Fall 12-17-2021

Spin-Dependent Electronic Transport in Noncollinear Antiferromagnetic Antiperovskites

Gautam Gurung
University of Nebraska-Lincoln, ggurung@huskers.unl.edu

SPIN-DEPENDENT ELECTRONIC TRANSPORT IN NONCOLLINEAR ANTIFERROMAGNETIC ANTIPEROVSKITES

by

Gautam Gurung

A DISSERTATION

Presented to the Faculty of

The Graduate College at the University of Nebraska

In Partial Fulfilment of Requirements

For the Degree of Doctor of Philosophy

Major: Physics and Astronomy

Under the Supervision of Professor Evgeny Tsymbal

Lincoln, Nebraska

December 2021

SPIN-DEPENDENT ELECTRONIC TRANSPORT IN NONCOLLINEAR ANTIFERROMAGNETIC ANTIPEROVSKITES

Gautam Gurung, Ph. D.

University of Nebraska, 2021

Advisor: Evgeny Tsymbal

Spin-dependent properties are the heart of spintronic devices. Spintronics exploits electron's spin, in addition to charge, to process and store the information. Recently, antiferromagnetic (AFM) spintronics has emerged as a subfield of spintronics, where an AFM order parameter (the Néel vector) is exploited to control spin-dependent transport properties. Due to being robust against magnetic perturbations, producing no stray fields, and exhibiting ultrafast dynamics, antiferromagnets can serve as promising functional materials for spintronic applications.

Among antiferromagnets, high Néel temperature noncollinear antiperovskites $ANMn_3$ (A = Ga, Ni, Sn, and Pt) are interesting due to their magnetic group symmetry supporting non-trivial spin-dependent transport phenomena. These materials have structural similarity to perovskites which allows their epitaxial deposition on perovskite substrates. Using symmetry analyses, first-principles methods based on density-functional theory, tight-binding Hamiltonian models, and magnetization dynamics techniques, this dissertation makes predictions and provides insights into different spin-dependent phenomena in non-collinear AFM antiperovskites. The results are as follow.

It is shown that the noncollinear AFM Γ_{4g} phase of the antiperovskites exhibits sizable anomalous Hall conductivity (AHC), while the Γ_{5g} phase has zero AHC by

symmetry. The Néel vector can be switched on the picosecond timescale using a spin torque generated by a spin polarized charge current. The critical switching current density can be tuned by $ANMn_3$ stoichiometry engineering.

It is demonstrated that the noncollinear AFM Γ_{5g} phase of $GaNMn_3$ exhibits unconventional spin Hall conductivity, in addition to the conventional existing in the paramagnetic phase. Due to its out-of-plane spin polarization, spin Hall current exerts a spin torque that can switch out-of-plane magnetization in an adjacent ferromagnet. This unconventional spin torque has been realized experimentally using spin torque ferromagnetic resonance measurements carried out by our collaborators at University of Wisconsin-Madison.

It is shown that noncollinear AFM antiperovskites allow generation of a spin-polarized longitudinal charge current like ferromagnets. The magnitude of the net spin polarization depends on crystallographic direction. These results demonstrate that AFM antiperovskites can be used as a spin source, spin-torque generator, and information carrier in spintronic devices.

ACKNOWLEDGEMENTS

I have received a lot of support throughout my Ph.D. work.

First, I would like to thank my supervisor, Professor Evgeny Tsymbal, whose expertise guided me to solve the challenging research problems and to learn the advanced theoretical methodologies. His critical analysis and the feedback to my research work have enhanced the quality of my work to a higher level.

I would like to thank postdoctoral fellows in our group, Tula Ram Paudel, Ding-Fu Shao, Hiroyuki Takenaka, and Ling-Ling Tao, for all the wonderful assistance they provided during my learning process. Especially, I would like to thank Ding-Fu Shao and Tula Ram Paudel for all the fruitful collaboration, without which much of the research work would not have been possible. Their guidance and intellectual input provided great insights into my research work. I would also like to thank graduate students in our group, especially Ming Li and Kai Huang, for their outstanding talks at our group meetings and other support as well. Advice given by Professor Sitaram Jaswal has been a great help for my research work. My special thanks are extended to Verona Skomski and graduate studies staffs at department of physics and astronomy.

I appreciate the endeavours from our collaborators. I acknowledge the excellent experimental work conducted by Tianxiang Nan, Neil Campbell, Professor Mark Rzchowski, Professor Chang-beom Eom at University of Wisconsin-Madison and Professor Paolo G. Radaelli at University of Oxford.

I want to say many thanks to my committee members, Professor Christian Binek, Professor Xia Hong, Professor Alexey Kovalev, and Professor Christos Argyropoulos for their guidance. Thanks for their reading and their comments on this dissertation.

Finally, I would like to thank my parents, brothers and sisters for their continuous support and love throughout my academic life. I would also like to thank my wife and her family for providing their warm support during my Ph. D. research. Last but not the least, I would like to thank all my Nepali friends at UNL and other graduate studies friends, especially Bret Gergley for the intellectual discussions at the coffee breaks.

Preface

The results presented in Chapter 3 are published in *Physical Review Materials* (G. Gurung, D. F. Shao, T. R. Paudel, E. Y. Tsymbal, Anomalous Hall conductivity of noncollinear magnetic antiperovskites, *Phys. Rev. Mat.* **3**, 044409 (2019)).

The results of Chapter 4 are published in *Physical Review B* (G. Gurung, D. F. Shao, E. Y. Tsymbal, Spin-torque switching of noncollinear antiferromagnetic antiperovskites, *Phys. Rev. B* **101**, 140405(R) (2020)).

The results of Chapter 5 are published in the *Nature Communications* (T. Nan, C. X. Quintela, J. Irwin, G. Gurung, D. F. Shao, J. Gibbons, N. Campbell, K. Song, S-Y Choi, L. Guo, R. D. Johnson, P. Manuel, R. V. Chopdekar, I. Hallisteinsen, T. Tybell, P. J. Ryan, J-W. Kim, Y. Choi, P. G. Radaelli, D. C. Ralph, E. Y. Tsymbal, M. S. Rzchowski, C. B. Eom, Controlling spin current polarization through non-collinear antiferromagnetism, *Nat. Commun.* **11**, 1 (2020)) and submitted to *Physical Review Materials* (G. Gurung, D. F. Shao, E. Y. Tsymbal, Spin polarization of noncollinear antiferromagnetic antiperovskites, *arxiv*:*2108.09540* (2021)).

Table of Contents

List of Figures

List of Tables

Chapter 1 Introduction

The quest for the energy efficient and ultrafast devices in the modern technological world has resulted in many scientific evolutions, especially in the field of spintronics. Spintronics is a branch of physics in which electronic devices use electron's spin instead of charge to carry the information and hence, these spintronic devices are robust against charge perturbations. For example, the presence of leakage currents results in loss of the information in electronic devices, but the intrinsic spin momentum is retained. The rise of spintronics was possible due to the realization of useful functional properties of magnetic materials. Figure 1.1 shows the schematics of some magnetic phases that exist in nature. A ferromagnetic (FM) phase [Fig. 1.1(a)] is characterized by a single sublattice with magnetization $\vec{m}_A$, which determines the FM order parameter known as magnetization $\vec{m} = \vec{m}_A$. A ferrimagnetic phase contains multiple sublattices such that the total magnetic moment is uncompensated and hence it can also be characterized by the magnetization. Figure 1.1(b) shows a two-sublattice ferrimagnet with magnetization $\vec{m}_A$ and $\vec{m}_B$. The magnetizations of the two sublattices are unequal and are pointing in opposite directions. The order parameter $\vec{m} = \vec{m}_A + \vec{m}_B$ is finite, as shown by the blue-white arrow in Figure 1.1(b). An antiferromagnetic (AFM) phase has magnetizations in multiple sublattices arranged in such a way that the total magnetization is compensated, *i.e.*, $\vec{m} = \vec{m}_A + \vec{m}_B + \vec{m}_C + \cdots = 0$. In this case, an AFM order parameter, known as the Néel vector, is used to explain properties of antiferromagnets. The antiferromagnets can be either collinear with two sublattices A and B [Fig. 1.1(c)] or noncollinear with three (or more) sublattices A, B, and C [Fig. 1(d)]. The Néel vector is defined as the staggered magnetization and hence, in general they can be expressed as $\vec{l} = \vec{m}_A - \alpha\, \vec{m}_B + \beta\, \vec{m}_C +$

⋯, where α, β are real value numbers. In the case of the collinear antiferromagnet, the Néel vector is defined by difference in the sublattice magnetizations, *i.e.*, $\vec{l}_1 = \vec{m}_A - \vec{m}_B$, as shown by the double head arrow with red and blue colour in Figure 1 (c). In the case of a noncollinear antiferromagnet, we can define two mutually orthogonal Néel vectors $\vec{l}_1 = \vec{m}_A - \vec{m}_B$ and $\vec{l}_2 = \vec{m}_A + \vec{m}_B - 2\,\vec{m}_C$ denoted by the two double head arrows in Figure 1.1(d). These examples indicate that the zero magnetization antiferromagnets must be very different from ferromagnets and ferrimagnets having finite magnetization.

Ferromagnets or their multilayer combinations are the main elements in the traditional spintronic devices because the FM finite magnetization can be easily manipulated and detected using conventional techniques. A well-known example is the giant magnetoresistance (GMR) effect in FM-based multilayers [1, 2]. The GMR effect occurs in a device, known as a spin valve, which consists of two FM layers separated by a thin nonmagnetic metallic spacer layer. The resistance of the spin valve depends on the relative magnetization orientation of the two FM layers. Similarly, in a magnetic tunnel junction (MTJ), where the two FM layers are separated by a thin nonmagnetic insulating barrier spacer layer, the tunnelling conductance depends on the relative magnetization orientation of the two FM layers. This phenomenon is known as the tunnelling magnetoresistance (TMR) effect [3, 4].

The discoveries of the GMR and TMR effects were helpful in developing low cost, high density disk drive storage devices. In such devices, an AFM layer is used as a secondary element. The antiferromagnet produces an exchange bias field to pin the magnetization orientation in the adjacent FM layer while the magnetization of the other FM layer remains free to rotate. This free-layer magnetization can be manipulated by an

external magnetic field. The change in the relative magnetization orientation can be detected by GMR or TMR. The two opposite orientations of the FM magnetization can be regarded as "0" and "1" information bits in a device. GMR and TMR effects find their use in the magnetic read heads in magnetic hard drives, magnetic field sensors, and magnetoresistive random access memories (MRAMs).

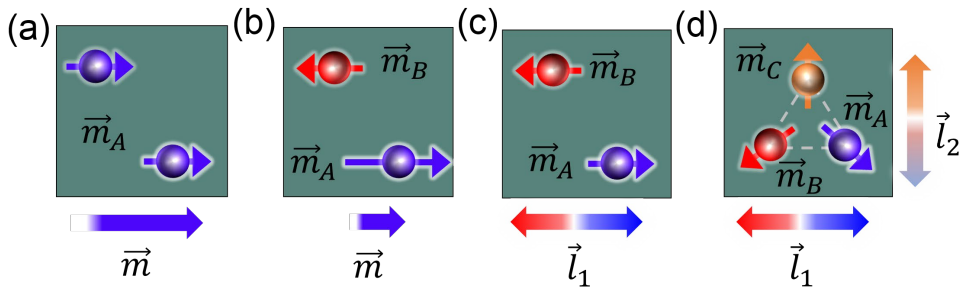

Figure 1.1. Schematics of different magnetic phases existing in nature. (a) Ferromagnetic phase with magnetization $\vec{m}_A$; (b) Ferrimagnetic phase with two sublattices having magnetizations $\vec{m}_A$ and $\vec{m}_B$; (c) Collinear antiferromagnetic phase with two sublattices having magnetization $\vec{m}_A$ and $\vec{m}_B$; and (d) Noncollinear antiferromagnetic phase with three sublattices having magnetization $\vec{m}_A$, $\vec{m}_B$, and $\vec{m}_C$. $\vec{m}$ is the net magnetization given by the sum of magnetizations of magnetic sublattices. $\vec{l}_1$ and $\vec{l}_2$ represent the Néel vector. Noncollinear antiferromagnets with three sublattices has two mutually orthogonal Néel vectors.

Slonczewski and Berger predicted that in addition to the external field, a spin-polarized charge current can control the magnetization orientation [5, 6]. Upon application of a sufficiently large charge current density in a spin valve, spin-polarized electrons flowing from the pinned FM layer exert a spin transfer torque (STT) on the free FM layer which can switch its magnetization. The two FM layers must have noncollinear

magnetization orientations to realize the STT. The theoretical prediction of STT has been promptly realized in the experiments [7– 9]. Utilizing the STT phenomenon in MTJs led to the development of the STT-MRAM which is nowadays used in various technological applications.

While STT has the advantage of high scalability of the non-volatile storage based on MTJs, it requires a high electrical current density. The large current dissipates a large energy. The energy dissipation can be somewhat reduced in spin-orbit torque (SOT)-MRAM. Here a FM layer is used in combination with a heavy non-magnetic (NM) metal layer. The in-plane charge current injected in the NM layer induces a transverse spin current due to the spin Hall effect (SHE) driven by the spin-orbit coupling (SOC) in the heavy metal [10, 11]. Still, the devices based on SOT have a large switching critical charge current density which is unwanted. Nevertheless, these are the main spintronic devices in the market nowadays and all of them constitute ferromagnets as primary functional materials with antiferromagnets being passive elements.

AFM materials are abundantly existent in nature, but they have a limited use in modern electronic devices. In MTJs and spin valves, the antiferromagnets provide only the supporting role delivering the hardness to a FM layer. Nobel prize laureate Louis Néel deemed antiferromagnets to be extremely interesting theoretically but useless practically [12]. This is mainly because of the difficulty to manipulate and detect their magnetic order parameter. However, recent demonstrations of the control of the Néel vector orientation using an electric current stimulated the idea of using antiferromagnets as a functional material in spintronics. The new research developments [13– 16] have

built up the emerging field of AFM spintronics which exploits antiferromagnets as the primary element in spintronics.

1.1. Antiferromagnetic Spintronics

An antiferromagnet with compensated total magnetization can be characterized by the Néel vector. The collinear and noncollinear antiferromagnets are determined by the overall orientation of the magnetization of each sublattice. These orientations define the unique symmetry as well as the Néel vector directions. A collinear antiferromagnet acts like two ferromagnets with their magnetic moment being antiparallel. In a noncollinear antiferromagnet, the total magnetization is fully compensated but the staggered (i.e., alternating in space) magnetic moment is finite like that in a collinear antiferromagnet. The staggered magnetic moment represents the Néel vector as shown in Figure 1.1(d). The zero magnetization in antiferromagnets makes them insensitive to the external magnetic field and hence, the Néel vector becomes difficult to manipulate. This has been the main reason of why antiferromagnets found their limited use in the spintronic devices. On the other hand, this insensitivity to the external magnetic field would make AFM spintronic devices robust against external perturbations. The information bits in the FM spintronic devices sometimes get changed accidentally due to the presence of an external magnetic field or even a static magnetic field generated within the device. This leads to the unwanted loss of information and in this regard, an AFM spintronic device is expected to have an advantage due to being robust with respect to magnetic perturbations.

The current research is focused on how the modern spintronic devices can be made robust and compact. When many FM elements in a device are kept in proximity of each other, stray magnetic fields can perturb the magnetic moments storing the

information. This makes it difficult to achieve ultrahigh density in spintronic devices with ferromagnets as the primary functional element. Synthetic antiferromagnets where two FM layers with antiparallel magnetization are coupled through Ruderman-Kittel-Kasuya-Yosida (RKKY) interactions were proposed as the alternative solution to reduce the magnetic stray fields [17]. But there is no complete compensation of the magnetization in synthetic antiferromagnets resulting in a small but finite stray field. On the contrary, antiferromagnets do not have any stray magnetic fields and hence, AFM spintronic devices can be compactly arranged side by side with ultrahigh density. Most importantly, the cost of making such kind of non-volatile and ultracompact devices is expected to be low. AFM materials are found abundantly in nature. These antiferromagnets can be metallic (FeMn, PtMn, IrMn, ANMn$_3$ (A = Ga, Ni, Sn, Pt, Zn, *etc.*), semiconducting (Sr_2IrO_4, MnTe, etc), semimetallic (CuMnAs, Mn_3Ge, Mn_3Sn, *etc*.) or insulating (NiO, CoO, Cr_2O_3, $BiFeO_3$, MnF_2, *etc*.) at room temperature.

In addition to all the above properties, modern devices should also be able to increase the time efficiency in doing the assigned work. The FM devices work at an optimal frequency within the GHz range, which limits the possibility of ultrafast performance. The presence of multiple sublattices which are coupled through the exchange field changes the dynamics of the antiferromagnets compared to the single sublattice ferromagnets. The FM resonance (FMR) frequency is enhanced by a factor proportional to the exchange field. Hence, the AFM resonance (AFMR) frequency is in the THz range [18].

A simple example of an antiferromagnet described by a two sublattice model within the mean field theory is demonstrated in Appendix A. It is seen that the AFM

dynamics [Eq. $(A12)$] is different from the FM dynamics [Eq. $(A1)$] and enhanced by the exchange field. Eq. $(A12)$ in Appendix A is equivalent to the Newton's equation for force acting on a solid body. An antiferromagnet follows the Newton's first law of motion which describes the motion of a solid object with mass reflecting the inertia effect. Therefore, upon removal of the force, the Néel vector in the antiferromagnet continues exhibiting the effect of the force until the external force opposes such inertial motion.

Although the results are very simplified, they agree well with the fact that the exchange field coupling of the multiple sublattices allows switching of the AFM order parameter much faster that the FM order parameter [15]. The exchange field enhancement also explains the requirement of a small charge current for the operation of the ultrafast AFM devices compared to FM counterparts. The power required to operate AFM devices is lower and hence, the energy loss by Joule heating is hugely minimized in antiferromagnets.

Unlike FM spintronics, AFM spintronics provides a chance of creating ultrafast, non-volatile, ultra-dense memory and logic devices. In addition to the binary bit cells, there has been suggestions of multilevel bit cells and neuromorphic computing in AFM based spintronic devices [13, 14, 16]. The AFM/FM system coupled with exchange bias behaves as a memristor (circuit element that can memorize the amount of past electric charge as its resistance) which can function as a synapse [19, 20]. Moreover, AFM multi-stable resistors [14, 21] can be realized and used in pulse-counter devices [22].

In additional to useful device functionalities, antiferromagnetism can give rise to interesting fundamental properties. Antiferromagnets break time-reversal $(\hat{T})$ symmetry

due to the presence of the staggered magnetic moment, but it can be combined with other

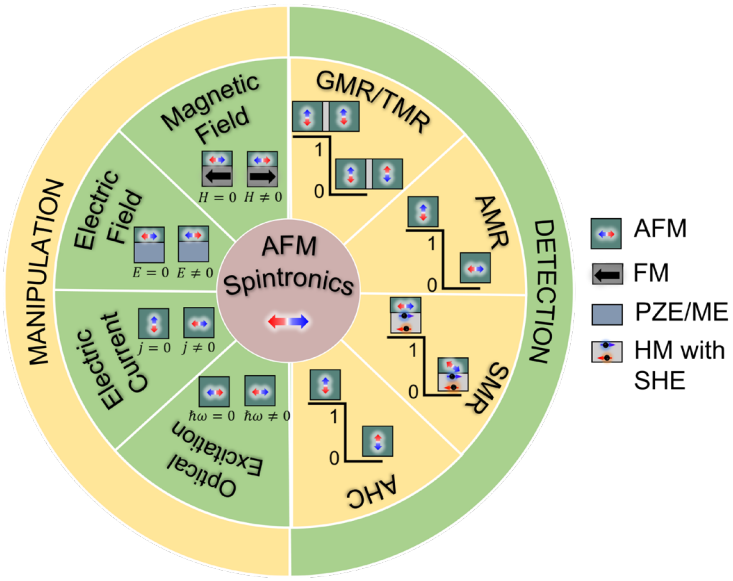

Figure 1.2. Manipulation and detection of the Néel vector in AFM spintronics. Manipulation of the Néel vector (represented by red-blue double arrow) is achieved by the application of magnetic field (H), electric field (E), electric current (j), and optical excitation ($\hbar\omega$). Schematics before and after application of the stimuli are shown in the respective sectors. Detection of the Néel vector is achieved by measuring giant magnetoresistance (GMR), tunnelling magnetoresistance (TMR), anisotropic magnetoresistance (AMR), spin Hall magnetoresistance (SMR), and anomalous Hall conductivity (AHC). The corresponding resistance states representing the information bits ("1" and "0") are shown in the respective sectors. AFM elements are shown with double-arrow Néel vectors, FM elements with a grey box with a black arrow, piezoelectric (PZE) or magnetoelectric (ME) elements with a blue box, and heavy metal (HM) inducing spin Hall effect (SHE) with a light grey box and arrows indicating the spin polarization.

symmetry operations ($\hat{O}$) like space-inversion symmetry ($\hat{P}$), mirror symmetry ($\hat{M}$), translation symmetry, *etc*. The conservation of the $\hat{O}\hat{T}$ symmetry results interesting topological properties (for example $\hat{P}\hat{T}$ symmetry enforces Kramers degeneracy and hence, the band crossing points forms Dirac points) and their dependence on the Néel vector orientation [23– 25]. These topological antiferromagnets exhibit different transport phenomena such as the anomalous Hall effect [26 – 37], the crystal Hall effect [38– 41], the anomalous Nernst effect [42], the spin Hall effect [43– 45], unconventional charge-to-spin conversion phenomena [46– 50], *etc*. Not only antiferromagnets have extra features compared to paramagnets and ferromagnets, but they also exhibit properties like those in paramagnets and ferromagnets which could make them useful and even dominant in the field of spintronics.

The realm of spintronics could be expanded to antiferromagnets if a possible solution was found to manipulate and detect the Néel vector. Figure 1.2 shows some possible ways to manipulate the Néel vector orientation and detect the change in its orientation. For example, the local staggered moment in antiferromagnets can be reoriented by applying a charge current (j) [14, 51]. In addition, Néel vector orientation can be controlled by a magnetic field (H) using an exchange bias or a heat-assisted magnetic recording technique [52– 57], an electric field (E), a piezoelectric (PZE) effect [58, 59] or a magnetoelectric (ME) effect [60– 62]), and optical excitation ($\hbar\omega$)[63]. The manipulation sector in Figure 1.2 shows two states before and after the application of the stimuli for the Néel vector reorientation. An AFM material is represented by the green box with the Néel vector indicated by a double arrow. The orientation of the Néel vector determines one of the two resistance states representing the

binary bits of information “1” and “0”. These resistance states can be read out by using GMR or TMR effects, anisotropic magnetoresistance (AMR), spin Hall magnetoresistance (SMR), and anomalous Hall conductivity (AHC). These methods of writing and reading the state of the Néel vector in antiferromagnets are further discussed in the next two sections.

1.2. Manipulation of the Néel Vector

The magnetization of a FM metal layer represents a state variable in modern spintronic devices. The ease to write the information bits by reorienting the magnetization in ferromagnets made them the primary element in spintronic devices. But with the massive advantages of antiferromagnets, it would be desirable to find ways to efficiently manipulate the Néel vector in antiferromagnets. Some of the methods such as the application of magnetic field, electric field, electric current, and optical excitation shown in Figure 1.2 will be discussed below [13, 15, 16, 64].

1.2.1. Magnetic

AFM materials are robust against magnetic perturbations due to the absence of a finite magnetization. Nevertheless, the magnetic moments on each sublattice can be rotated upon application of a large external magnetic field [47, 65, 66]. For example, the Néel vector of a noncollinear antiferromagnet Mn_3Sn with in-plane anisotropy was shown to reorient in a large magnetic field [47]. In general, antiferromagnets have zero magnetization but in some antiferromagnets like Mn_3Sn, symmetry allows a small uncompensated magnetic moment in specific directions. The application of external magnetic field may bring the magnetic material through metamagnetic transition. When the field is applied parallel to the easy axis, the antiferromagnet becomes unstable and

hence, the sublattice magnetizations rotate freely in the direction perpendicular to the easy axis above some critical field. This phenomenon is known as the spin-flop transition and the corresponding critical field is called the spin-flop field. This occurs due to the competition of the Zeeman energy in the applied magnetic field and the magneto-crystalline anisotropy energy. In the presence of the weak anisotropy field, the applied magnetic field leads to the rotation of the direction of staggered magnetization perpendicular to the easy axis. In contrast, in case of the strong magneto-crystalline anisotropy, there is a sudden rotation of the magnetization of one of the sublattices which is pointed antiparallel to the field direction at the critical field. This phenomenon is defined as the spin-flip transition. This explanation agrees with the AFM dynamics presented in Appendix A for the case of a uniform magnetic field.

As was discussed earlier, antiferromagnets are used as passive elements in FM spintronic devices to produce an exchange bias and pin the FM magnetization. The exchange bias can also be used in AFM spintronics but this time to write the information using the AFM Néel vector. The exchange coupled ferromagnet creates an AFM exchange spring effect which transfers the change of the magnetic moment orientation from the ferromagnet to the antiferromagnet [52, 53, 67, 68]. The exchange bias effect reduces the strength of the magnetic field required to manipulate the Néel vector. Upon application of external magnetic field, the ferromagnet reorients its magnetization towards the direction of the field as shown in Figure 1.2. This results in the slight rotation of the AFM moments due to the presence of the exchange bias. This has been demonstrated in many experiments where the rotated Néel vector was detected using tunnelling AMR [52, 53, 64, 69]. The exchange spring is affected by AFM film

thickness, temperature, layer termination, *etc*. [52, 70]. Due to the film thickness dependence, this phenomenon occurs within the AFM domain wall width and hence, the AFM film grown should be limited within this domain wall thickness. Changes in temperature and layer termination alter interface characteristics significantly influencing the effect. This puts limitations on the use of the exchange bias. Moreover, the exchange-coupled system uses a FM layer to control the AFM magnetic moment. The presence of the FM layer produces a stray magnetic field and hence, such a coupled system can be affected by weak magnetic perturbations.

Reorientation of the Néel vector can also be achieved by heat assisted field cooling. An antiferromagnet can be field cooled below the Néel temperature resulting in different AFM orientations thus different AMR [71, 72]. The field cooling of the antiferromagnet may result in the formation of different metastable AFM phases in various proportions. Magnetic materials undergo phase transitions at different temperature. Some materials can be in an AFM phase at low temperature and a FM phase at high temperature. In such cases, the material can be driven to high temperature so that the magnetization of the corresponding FM phase can be reoriented by application of the external field, then, the material can be field cooled below the Néel temperature producing an antiferromagnet with different Néel vector orientations corresponding to the high temperature FM magnetization orientation [71]. The heat assisted method reduces the magnitude of the external magnetic field required to reorient the Néel vector. This all shows that the AFM can be manipulated by the application of the external magnetic field assisted by field-cooling or exchange bias effect.

1.2.2. Optical

Magnetic materials interact with light and hence, the AFM magnetic moments can be optically manipulated. The spin-lattice interaction can be enhanced by the optical excitations in antiferromagnets. The temperature dependent magneto-crystalline anisotropy in some antiferromagnets (for example, rare-earth orthoferrites $RFeO_3$) can be tuned by passing an ultrashort laser pulse [73]. This laser pulse leads to spin-lattice interaction and hence, reorientation of the Néel vector, as shown in Figure 1.2. Similarly, in the multiferroic with antiferromagnetic phase (e.g., $TbMnO_3$), the Néel vector was found to be reversed using optical excitations [74]. The switching of the AFM order parameter was achieved based on two colour light pulses which were absorbed based on the electric polarization induced by the corresponding Néel vector. In addition to the optical excitations, the application of the laser pulses can produce an effective magnetic field in the presence of a circularly polarized pump pulse which can drive inertia motion between two metastable phases. AFM dynamics is defined in terms of the staggered magnetization ($\vec{l}_i$) and this dynamic follows the Newtonian motion as shown in Appendix A [Eq. ($A11$)]. The FM dynamics is of first order in time, but the AFM dynamics is of second order in time which defines the massive particle and thus the capability of inertia-driven motion [75]. In the inertia-driven motion, the Néel vector can reorient even after the light pulse is switched off. The main difference of the optical manipulation of the AFM order parameter compared to the FM order parameter is that the Néel vector reorientation acts like the rotation of the solid body due to the Newtonian effect [16, 64, 75].

1.2.3. Electric: Field Induced

The magnetic properties of a material can be changed by applying a strain. Changes in the atomic environment in the magnetic material alters the magnetic anisotropy due to a change in spin-orbit interactions. For example, in collinear antiferromagnet Mn_2Au, application of the sufficiently strong strain along the easy axis rotates the uniaxial anisotropy compared to the unstrained antiferromagnet [76]. The metamagnetic phase transition from a FM to AFM phase can also involve changes in the atomic structure. This implies that the epitaxial growth of such kind of AFM thin films on different substrates can control the orientation of the Néel vector due to different strain applied on the thin film. Such effect has been realized in FeRh thin films grown on different substrates [77, 78]. Moreover, if the substrate is piezoelectric the application of electric field changes the lattice parameters and hence can change the Néel vector orientation and even produce FM to AFM phase transition. This effect was realized using FeRh films epitaxially grown on the ferroelectric $BaTiO_3$ crystals under application of an electric field. It was shown that the FeRh films can be electrically driven through the phase transition from ferromagnet to antiferromagnet [79, 80]. The application of the voltage made the ferroelectric domain in $BaTiO_3$ uniform and hence, voltage-induced strain in FeRh changed the magnetization significantly. Like the metamagnetic transition, application of electric field can tune the exchange spring effect in AFM metals [81]. Therefore, combining the magnetic and electric fields can help to achieve the reorientation of the Néel vector.

A combination of an antiferromagnet with high Néel temperature (T_N) with a piezoelectric could make it possible to realize ultra-dense energy-efficient spintronic

devices. Collinear antiferromagnets MnPt ($T_N \sim 975$ K) and Mn_2Au ($T_N > 1000$ K) in combination with piezoelectric PMN-PT show that the AFM order parameter can be manipulated by the piezoelectric strain induced in the PMN-PT substrate due to application of an electric field in the order of 1 kV/cm at room temperature [58, 82]. These devices were found to show the rotation of the AFM order parameter due to the piezoelectric effect and the observed states were unperturbed even in the presence of a huge magnetic field. They exhibited low and high resistance states even at zero electric field. This is due to the remnant polarization of PMN-PT inducing residual strain on the antiferromagnet. The piezoelectric strain changes the magnetic easy axis of the adjacent antiferromagnet and hence, the Néel vector reorients.

In addition to the piezoelectric effect, AFM materials also show a magnetoelectric (ME) effect in which the electric field can control the orientation of the AFM order parameter. In single-phase ME materials, the unidirectional magnetic anisotropy can be switched without the piezoelectric effect. The FM surface in collinear AFM chromia Cr_2O_3 (0001) provides the reversible, isothermal, and global electric control of the exchange bias in the presence of small external magnetic field such that the product of the applied electric field and the magnetic field is above the critical value [60]. The change in the sign of the exchange bias indicates the change in the surface magnetization orientation associated with the global rotation of the Néel vector by π in ME Cr_2O_3.

The exchange bias effect discussed above needs to have FM and AFM layers adjacent to each other, but it would be desirable to avoid ferromagnets as a passive element in AFM spintronics. Experimentally, it was observed that the AFM order parameter can be controlled in a Cr_2O_3/Pt heterostructure, *i.e.*, without any FM element,

by applying electric field in presence of a low external magnetic field [61]. The advantage of using purely AFM components in spintronic devices is a possibility of ultrafast switching of the order parameter. But still the requirement of a non-zero applied magnetic field remains for the ME switching of Cr_2O_3. Recently, it was found that in the B-doped ME AFM Cr_2O_3, the Néel vector can be rotated upon application of the electric field only [62]. This was possible due to the formation of the polar nano regions changing the magnetic anisotropy of Cr_2O_3 and resulting in rotation of the Néel vector.

1.2.4. Electric: Current Induced

One of the well-known methods to manipulate FM magnetization is by applying an electric current [83– 86]. For example, in FM spin valves or MTJs, the transfer of spin angular momentum leads to the rotation of the FM magnetization in the free layer. The longitudinal current across the spin-valves gets spin polarized in the pinned FM layer and this spin polarization produces a spin transfer torque of the free FM layer which magnetization is noncollinear to that of the pinned layer. If the spin transfer torque is sufficiently large this leads to the switching of the free FM layer. Similar, AFM spin valve has been proposed using a one-dimensional (1D) model [51], which was later elaborated using more sophisticated models [87– 90]. So far, however, no experimental evidence of AFM switching has been demonstrated using this approach involving AFM spin valves or MTJs. Nevertheless, more recent theoretical and experimental developments showed that the AFM order parameter can be manipulated by electric currents in bulk antiferromagnets provided that certain symmetry conditions are satisfied [13–16, 53, 71]. For example, the presence of inversion asymmetry allows producing a finite spin-orbit torque on the Néel vector. The spin-orbit torque can also be exerted by

absorption of the spin polarization generated by the spin Hall effect in the adjacent heavy metal.

The electric current in a non-magnetic semiconductor with broken inversion symmetry results in a finite non-equilibrium spin polarization density. This phenomenon is known as the inverse spin galvanic effect (iSGE) or the Edelstein effect [91]. FM materials with the broken inversion symmetry exhibit the iSGE, where the induced non-equilibrium spin accumulation depends on the direction of the electric field [92 – 94]. The exchange interaction between the conduction electrons and the magnetization results in the finite spin-orbit torque which can be used to manipulate the FM order. Similarly, in antiferromagnets with broken inversion symmetry, there is a finite non-equilibrium spin polarization analogous to that in ferromagnets.

There are two types of the spin accumulation in sublattice A of a two-dimensional (2D) antiferromagnet with broken inversion symmetry:

$$\vec{p}_A = s_{intra}\,\vec{z}\times\vec{j} + s_{inter}\,\vec{m}_A\times\vec{z}\times\vec{j}\,, \tag{1.1}$$

where $\vec{z}$ is normal to the 2D plane, $\vec{j}$ is the applied current density, and $\vec{m}_A$ is the sublattice magnetization. The first contribution is the intraband effect associated with the extrinsic properties arising from the iSGE, and the second term is the interband effect which can be purely intrinsic. The iSGE produces the same kind of spin accumulation on the two sublattices because it is independent of the sublattice magnetization. This is the reason why the torque produced by the first term acts in opposite directions on the two magnetic sublattices which cancels the net effect at the macroscopic level. This torque is inefficient for switching the Néel vector. On the contrary, the second term produces

opposite spin accumulation of the two magnetic sublattices due to its dependence on the sublattice magnetization. Therefore, this kind of torque can switch the Néel vector.

The torque exerted on the sublattice magnetization due to the non-equilibrium spin accumulation can be expressed as

$$\tau_A = \tau_{FL}\ \vec{m}_A \times (\vec{z} \times \vec{j}_e) + \tau_{DL}\vec{m}_A \times (\vec{z} \times \vec{j}_e \times \vec{m}_A), \qquad (1.2)$$

where the first term defines the field like torque and the second term defines the damping like torque. The AFM order parameter with broken inversion symmetry can be reoriented by the damping like torque [95]. This relativistic effect is known as the Néel spin-orbit torque (NSOT). In antiferromagnets with bulk inversion symmetry, the NSOT having field like torque features can be realized [95]. This occurs in AFM metals exhibiting the combination of the inversion and time reversal symmetries (PT symmetry). In the local environment, due to the presence of two different magnetic sublattices, the inversion symmetry is broken, but due to the two magnetic sublattices occupying the inversion partner lattice sites, the PT symmetry is preserved. This leads to Kramers' degeneracy of the electronic bands. Each spin band is equally contributing due to the two magnetic sublattices. In the presence of the electrical current, each magnetic sublattice generates a nonequilibrium spin accumulation proportional to $(-1)^s \vec{z} \times \vec{j}$, where *s* is 0 or 1 for different magnetic sublattices. The staggered spin-orbit field exerts a staggered field like torque which can switch the orientation of the Néel vector. AFM crystals like Mn_2Au, CuMnAs, *etc*. are centrosymmetric in bulk but the Mn sublattices occupy inversion partner cites and hence, the staggered spin-orbit torque is generated upon application of the current. This can lead to the reorientation of the Néel vector by $\pi/2$ [14, 95, 96]. The

AFM dynamics in Appendix A for the case of uniform and staggered fields agrees with the above discussion that the staggered field is required for deterministic switching.

As mentioned earlier, the spin-orbit torque can be provided in a ferromagnet/ heavy metal combination due to the spin Hall effect. This is also possible using an antiferromagnet/heavy metal bilayer. The non-equilibrium spin accumulation at the interface of the bilayer due to the spin Hall effect in the heavy metal gets absorbed in the antiferromagnet and exerts a damping like NSOT which can rotate the Néel vector. Recent experimental results in noncollinear AFM IrMn and collinear AFM insulator NiO thin films which were kept in contact with heavy metals, like Ta or Pt, showed that the spin-orbit torque can be realized due to the spin Hall effect in heavy metal [97, 98].

1.3. Detection of the Néel Vector

In the previous section, we discussed different methods to manipulate the Néel vector in antiferromagnets, but they would not be worth if we could not read out the changes in the AFM order parameter. Changes in the macroscopic magnetization orientations in ferromagnets are detected using the magnetoresistive effects like GMR, TMR, and AMR. The counterparts of such magnetoresistive behaviours can be found in antiferromagnets as well. On passing through a spin valve or MTJ, the reading current depends on the relative orientation of the magnetization in FM layers which gives rise the GMR or TMR effects. The spin torque applied by the charge current on the magnetization of a FM free layer is explained based on the conservation of the total spin angular momentum. The approximation that the local spin angular momentum is conserved can also be used in antiferromagnets [99– 101]. So, from the microscopic point of view, the difference in the local torques due to the applied charge current acting on the magnetic sublattices with

opposite spins can change the Néel vector orientation. While the possibility of GMR was proposed for spin valves based on AFM metals, its realization required very strict interface conditions and a coherent transport through the interface [51, 101– 103]. The interfaces should have a perfect structural order which is mostly not under the experimental control and hence, the experimental realization of the GMR effect was not achieved with only AFM elements [104, 105]. Similarly, the TMR effect in the AFM tunnel junctions was found difficult to detect experimentally and even, if detected it was found to be very small [16]. In the AFM/FM case, a finite TMR was observed due to the exchange bias but there was no clear explanation of the origin of the spin torque effect [105, 106].

Initially, anisotropic magnetoresistance (AMR) was used as reading method in the FM-based recording devices. AMR depends on the spin-orbit coupling. AMR is an even function of magnetization ($\rho \propto \left(\hat{M}.\hat{j}\right)^2$) and hence, we expect it to occur in AFM metals as well. There are two types of AMR, namely ohmic non-crystalline AMR and ohmic crystalline AMR. Non-crystalline AMR depends on the angle between the direction of the current and the magnetization and hence, the electron travelling parallel and perpendicular to the magnetization axis is scattered differently by the relativistic spin-orbit coupling. But the crystalline AMR depends on the angle between the magnetization and the crystal axes and hence, different magnetization direction changes the relativistic electronic structure in such cases. The non-crystalline AMR effect was observed in collinear antiferromagnets like FeRh, CuMnAs, Mn_2Au, *etc.* under application of the reading current after manipulation of the Néel vector [14, 71, 96, 107]. In the single crystalline AFM Sr_2IrO_4, the current is applied perpendicular to the magnetization plane,

but the AMR effect was observed with respect to the crystal axes indicating crystalline AMR [108]. The main information in such cases is that the relative orientation of the Néel vector with respect to the staggered magnetization axis or crystal axes changes the resistance and, hence, we obtain the AMR effect.

Similar to a single FM layer, in a tunnel junction with a single FM electrode, the system goes from high to low resistance state on changing the direction of the applied magnetic field due to the presence of magneto-crystalline anisotropy originating from the relativistic spin-orbit coupling [109– 112]. This phenomenon is known as tunnelling anisotropic magnetoresistance (TAMR). The even dependence of the TAMR on the magnetic moment indicates that this effect should also be present in case of an AFM electrode. This fact has been confirmed experimentally in several works [14, 21, 52, 53, 71, 108, 113, 114]. The physical origin of TAMR is that in a tunnel junction with an AFM electrode, the spin-orbit coupling makes the tunnelling density of states dependent on the Néel vector direction [76]. Therefore, AFM can effectively determine the spin-dependent transport properties. The change in the orientation of the magnetic moment in a single layer is sufficient for the appearance of TAMR which removes the stringent conditions required for GMR in AFM spin valves. The TAMR effect can also be achieved by combining FM/AFM with the tunnel barriers [52, 76]. The exchange spring effect due to the FM/AFM coupling changes the Néel vector and hence the resistance state.

As was discussed before, AFM insulators in combination with heavy metals can be switched using the NSOT originated from the spin accumulation due to the spin Hall effect in an adjacent heavy metal layer [98, 115]. The detection of such switching cannot

be done with AMR because the AFM insulators are used in these experiments. In some cases, the AFM insulators themselves can also be used as a tunnel barrier and hence, the TMR effect can be expected. But one of the most promising method to detect the switching of the Néel vector in an AFM insulator is the spin Hall magnetoresistance (SMR). Unlike AMR, the SMR is the change of the resistance with the change of the angle between the spin polarization generated due to the spin Hall effect in a heavy metal with the AFM Néel vector [116]. In the case of the AFM insulators/heavy metal bilayer, on passing the charge current through the heavy metal, a finite non-equilibrium spin polarization is created at the interface due to the spin Hall effect. If this spin polarization is non-collinear to the Néel vector, a part of the spin current gets absorbed exerting a spin transfer torque and hence, the inverse spin Hall effect generates small current [116, 117]. This implies that the corresponding state has larger resistance compared to the state with collinear spin polarization. This difference helps to detect switching of the Néel vector in AFM insulators.

In antiferromagnets, the value of the AMR, TAMR, and SMR effects are found to be very small and hence, we get a very weak signal while trying to read the information bits written in AFM devices [14, 16, 117]. Moreover, the AMR signal detected experimentally may be an artifact of the multiterminal patterned structure which is used to detect the AFM switching [118]. The AMR signal indicating the switching of the Néel vector was also detected in the Pt/Si bilayer without any AFM layer. This indicates that the AMR signal may be not reliable. Alternative ways to detect the Néel vector switching in antiferromagnets need to be searched.

When an electrical current is applied across the ferromagnet with finite magnetization, perpendicular current is created. This phenomenon is known as the anomalous Hall effect (AHE). Conventional Hall resistivity is defined as $\rho_H = \rho_O B + \rho_M M$ where ρ_0 is the ordinary Hall resistivity due to the Lorentz force generated by the applied magnetic field B and ρ_M is the anomalous Hall resistivity associated with the finite magnetization M of the ferromagnet.

Recently, the AHE was found to exist in the AFM metal with zero net magnetization due to the presence of the finite total Berry curvature [26, 28, 38]. The Berry curvature acts like a magnetic monopole in the AFM momentum space, and this gives rise to the finite anomalous Hall conductivity (AHC) for the antiferromagnet with uncompensated magnetization. In such materials, there are no time reversal symmetry or any combination of time reversal symmetry and crystal symmetry which does not allow any finite net magnetization. Theoretical and experimental calculations show that both collinear and noncollinear AFM metals with uncompensated magnetization can have large AHC comparable to that obtained in FM metals [26, 28–30, 36–38, 119]. The finite AHC in collinear antiferromagnets originates due to the arrangement of the nonmagnetic atoms and the AHC originated through this mechanism is referred to as the crystal Hall effect (CHE) [38]. A change in the magnetization direction changes the electronic structure and hence, the anomalous Hall resistivity which can be used to read out the state of the Néel vector. Although the antiferromagnet has zero net magnetization, in some cases, we can consider a finite magnetization along certain directions which does not break the magnetic group symmetry of the material considered. For example, if the antiferromagnet has a combined time reversal and mirror symmetry, a finite

magnetization is allowed parallel to the mirror plane. These antiferromagnet where finite uncompensated magnetizations are allowed by symmetry were seen to have small uncompensated magnetization in the experimental setup as well [26, 28–30, 36–38]. This type of antiferromagnetic material will always have a finite AHC. Unfortunately, there are many AFM materials in which the magnetic group symmetry leads to zero net magnetization. Such materials generally have combined time reversal and translation symmetries which makes the total Berry curvature zero and hence, zero AHC. However, if the system has broken inversion symmetry, then it has a finite Berry curvature dipole which determines the nonlinear AHE [120– 123]. The Berry curvature dipole changes with the orientation of the Néel vector and hence, in any compensated antiferromagnet, switching of the Néel vector can be read out by measuring the nonlinear AHC.

1.4. Antiperovskites

Antiperovskites are materials with the perovskite structure but interchanged positions of the cations and anions. An antiperovskite can be described by the formula AXM_3, where M is the cation, A and X are anions. The cation M occupies the corner sharing octahedra sites with the X anion as shown in Figure 1.3 (a). The chemical formula shows that antiperovskites are rich chemically with M cation. This M cation determines magnetism of the antiperovskite. A magnetic antiperovskite AXM_3 has transition metals like Fe, Mn, Cr, *etc*. as M cations, X are usually the *p*-block elements like C, N, S, *etc*., and A is usually either the transition metal like Zn, Ni, Pt, Cu, *etc*. different from M or a *p*-block element like Ga, Sn, Pb, Br, Ge, *etc*. as shown in Figure 1.3(a). Mn based magnetic antiperovskites are very interesting because they exhibit different magnetic phases, such as ferromagnetic, antiferromagnetic, and ferrimagnetic, at room temperatures as shown in

Figure 1.3(b)-(e) [124, 125]. Moreover, chemical substitution in antiperovskites provides a new material platform for stoichiometrically engineered new devices favourable for some applications [125 – 127]. Figure 1.3(b) shows the collinear FM antiperovskites, e.g., $GaCMn_3$ with magnetization pointing along the (111) direction. Doped antiperovskites like $Ga_{1-x}Sn_xCMn_3$ are found to exist in the ferrimagnetic phase with two magnetic sublattices in the [111] plane with opposite and unequal magnetizations as shown in Figure 1.3(c). Noncollinear AFM phase Γ_{4g} and Γ_{5g} with three sublattice magnetizations on a single [111] plane is found to be stable at room temperature for antiperovskites like $NiNMn_3$ and $GaNMn_3$, respectively. These structures are shown in Figures 1.3(d) and 1.3(e), respectively, where the magnetization on each sublattice makes an angle of $2\pi/3$ with each other. It is evident that they can be converted to each other by rotation of $\pi/2$ about the (111) axis.

Antiperovskites are found to possess many functional properties like superconductivity [128], magnetoresistance [129], and magnetovolume [124, 130, 131], magnetocaloric [132, 133], piezomagnetic [134– 136], and barocaloric effects [137]. As mentioned, the AXM_3 antiperovskites exhibit an AFM ordering, both collinear and noncollinear. Most of these AFM phases occurs at room temperature. For example, the Neel temperatures of some of these antiperovskites are $GaNMn_3$ – 288K, $NiNMn_3$ – 262K, $SnNMn_3$ – 237K, $PtNMn_3$ – 510K [124, 131, 138]. Also, the antiperovskite materials have flexibility for the magnetic phase transitions. The magnetic phases can be changed by doping, strain, pressure, or temperature [126, 139, 140]. The metallic antiperovskites can also host interesting topological properties [141– 143]. These

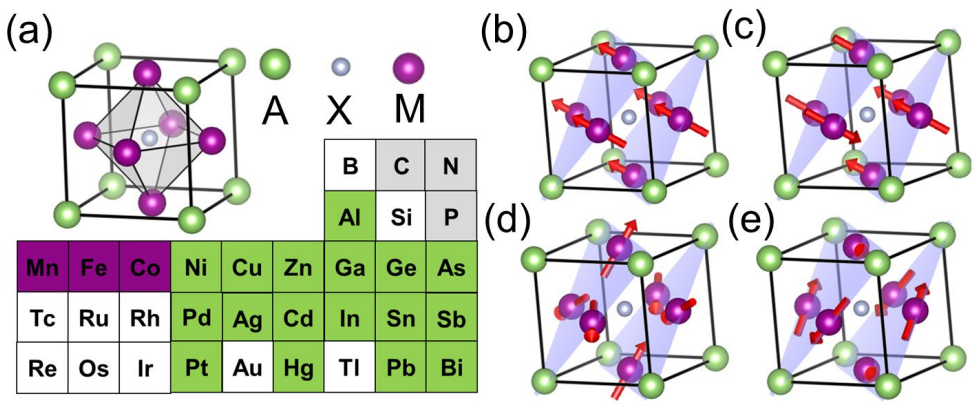

Figure 1.3. Antiperovskite AXM_3 structure and different Magnetic phases. (a) General structure of antiperovskite with octahedral cavity formed by anion X. Part of periodic table with the purple colour represents the possible M cation, anion A and X represented by grey and green colour. (b) Ferromagnetic phase with magnetization in (111) direction (c) Collinear antiferromagnetic phase with Néel vector in (111) direction. Noncollinear magnetic phase (d) Γ_{4g} and (e) Γ_{5g} with magnetic vectors lying on the [111] plane making an angle $2\pi/3$ with each other.

properties of the antiperovskites make these materials interesting for further exploration and using them in AFM spintronic devices.

1.5. Motivations

The great advantages of the antiferromagnets over ferromagnets for the development of ultrafast, ultradense, and ultrarobust spintronic devices have stimulated the search for new functional spin-dependent transport properties of different AFM materials. Mn based magnetic antiperovskites with plethora of AFM phases (collinear or noncollinear AFM phases like Γ_{4g} and Γ_{5g}) provide the new material platform to explore for the potential use in AFM spintronics. Due to the different AFM phases having different magnetic

group symmetries, these materials are expected to exhibit very diverse spin-dependent transport properties. These involve the anomalous Hall effect and the spin Hall effect, which appearance are controlled by the Berry curvature – the topological property intrinsic to the spin-dependent electronic band structure of the material. The AHE may be useful for the detection of the Néel vector in the AFM materials and has advantages over the AMR and TMR effects by the magnitude of this effect as well as a more simplified experimental setup. The SHE is interesting because, as is shown in this dissertation, its magnitude appears to be sizable despite a relative low spin-orbit coupling in AFM antiperovskites. Moreover, it appears that spin Hall conductance is strongly dependent on the current direction with respect to the crystallographic axes as well as the orientation of the Néel vector. Since the spin current generated by the SHE can be used to produce spin-orbit torques, this result could provide an opportunity to control the spin-orbit torques by the Neel vector. Furthermore, there is a possibility to control the non-collinear AFM state as well as the orientation of the Néel vector by an applied spin-polarized current. In AFM metals, the spin dynamics occurs on the *ps* scale, *i.e.*, much faster than in ferromagnets where it occurs on the *ns* scale. The dynamics of the switching process driven by spin-polarized current is another important direction to explore.

The theoretical studies of these phenomena carried out in this dissertation are expected to provide the new fundamental knowledge about functional properties of the AFM antiperovskite materials which could be useful for their experimental exploration as well their use in AFM spintronics. Recent advances in thin-film growth techniques have demonstrated a possibility to realize singe-crystal antiperovskite structures grown epitaxially on different substrates. Therefore, the results of this dissertation may provide

guidance to the experimentalists working in this field on anticipated functional properties of the AFM antiperovskite materials.

The structure of this dissertation is as follows. Chapter 2 elaborates the theoretical methods implemented in this work. Chapter 3 involves the study of the different AFM phases of the antiperovskite materials to explain the symmetry requirements for the existence of the finite anomalous Hall conductivity. Chapter 4 is devoted to AFM terahertz dynamics driven by the application of the spin-polarized charge current and the importance of the antiperovskite stoichiometrically on the possibility to realize these dynamics in practice. Chapter 5 explores spin polarization of the Mn based antiperovskites dependent on the Néel vector which can be used to generate the unconventional spin-orbit torque properties and involves collaboration with experimentalists. Finally, Chapter 6 summarizes the results and concludes this dissertation.

References

[1] F. Saurenbach, U. Walz, L. Hinchey, P. Grunberg, and W. Zinn, Static and dynamic magnetic properties of Fe-Cr-layered structures with antiferromagnetic interlayer exchange. *J. Appl. Phys.* **63**, 3473 (1988).

[2] M. N. Biabich, J. M. Broto, A. Fert, F. N. V. Dau, F. Petroff, P. Etienne, G. Creuzet, A. Friederich, and J. Chazelas, Giant Magnetoresistance of (001)Fe/(001)Cr Magnetic Superlattices. *Phys. Rev. Lett.* **61**, 2472 (1988).

[3] M. Julliere, Tunneling between ferromagnetic films. *Phys. Lett. A* **54**, 225 (1975).

[4] J. S. Moodera, L. R. Kinder, T. M. Wong, and R. Meservey, Large magnetoresistance at room temperature in ferromagnetic thin film tunnel junctions. *Phys. Rev. Lett.* **74**, 3273 (1995).

[5] J. C. Slonczewski, Conductance and exchange coupling of two ferromagnets separated by a tunnelling barrier. *Phys. Rev. B* **39**, 6995 (1989).

[6] L. Berger, Emission of spin waves by a magnetic multilayer traversed by a current. *Phys. Rev. B* **54**, 9353 (1996).

[7] M. Tsoi, A. G. M. Jansen, J. Bass, W. C. Chiang, M. Seck, V. Tsoi, and P. Wyder, Excitation of a magnetic multilayer by an electric current. *Phys. Rev. Lett.* **80**, 4281 (1998).

[8] M. Tsoi, A. G. M. Jansen, J. Bass, W. C. Chiang, V. Tsoi, and P. Wyder, Generation and detection of phase-coherent current-driven magnons in magnetic multilayers. *Nature* **406**, 46 (2000).

[9] J. A. Katine, F. J. Albert, R. A. Buhrman, E. B. Myers, and D. C. Ralph, Current-driven magnetization reversal and spin-wave excitations in Co/Cu/Co pillars. *Phys. Rev. Lett.* **84**, 3149 (2000).

[10] A. Chenyshov, M. Overby, X. Liu, J. K. Furdyna, Y. L-Geller, and L. P. Rokhinson, Evidence for reversible control of magnetization in a ferromagnetic material by means of spin-orbit magnetic field. *Nat. Phys.* **5**, 656 (2009).

[11] I. M. Miron, G. Gaudin, S. Auffret, B. Rodmacq, A. Schuhl, S. Pizzini, J. Vogel, and P. Gambardella, Current-driven spin torque induced by the Rashba effect in a ferromagnetic metal layer. *Nat. Mater.* **9,** 230 (2010).

[12] L. Néel, Magnetism and the local molecular field. *Nobel Lectures, Physics* 1963 (1970).

[13] T. Jungwirth, X. Marti, P. Wadley, and J. Wunderlich, Antiferromagnetic spintronics. *Nat. Nanotechnol.* **11**, 231 (2016).

[14] P. Wadley, B. Howells, J. Zelezny, C. Andrews, V. Hills, R. P. Campion, V. Novák, K. Olejník, F. Maccherozzi, S. S. Dhesi, S. Y. Martin, T. Wagner, J. Wunderlich, F. Freimuth, Y. Mokrousov, J. Kunes, J. S. Chauhan, M. J. Grzybowski, A. W. Rushforth, K. W. Edmonds, B. L. Gallagher, and T. Jungwirth, Electrical switching of an antiferromagnet. *Science* **351**, 587 (2016).

[15] E.V. Gomonay and V. M. Loktev, Spintronics of antiferromagnetic systems. *Low Temp. Phys.* **40,** 17 (2011).

[16] V. Baltz, A. Manchon, M. Tsoi, T. Moriyama, T. Ono, and Y. Tserkovnyak, Antiferromagnetic spintronics. *Rev. Mod. Phys.* **90,** 015005 (2018).

[17] S. S. P. Parkin Systematic variation of the strength and oscillation period of indirect magnetic exchange coupling through the 3d, 4d, and 5d transition metals. *Phys. Rev. Lett.* **67**, 3598 (1991).

[18] T. Kamparth, A. Sell, G. Klatt, A. Pashkin, S. Mahrlein, T. Dekorsy, M. Wolf, M. Fiebig, A. Leitenstorfer, and R. Huber, Coherent terahertz control of antiferromagnetic spin waves. *Nat. Photonics* **5**, 31 (2011).

[19] W. A. Borders, H. Akima, S. Fukami, S. Moriya, S. Kurihara, Y. Horio, S. Sato, and H. Ohno, Analogue spin-orbit torque device for artificial-neural-network-based associative memory operation. *Appl. Phys. Express* **10**, 013007 (2017).

[20] A. Kurenkov, S. Fukami, and H. Ohno, Neuromorphic computing with antiferromagnetic spintronics. *J. Appl. Phys.* **128**, 010902 (2020).

[21] D. Kriegner, K. Výborný, K. Olejník, H. Reichlová, V. Novák, X. Marti, J. Gazquez, V. Saidl, P. Nemec, V. V. Volobuev, G. Springholz, V. Holý, and T. Jungwirth, Multiple-stable anisotropic magnetoresistance memory in antiferromagnetic MnTe. *Nat. Commun.* **7**, 11624 (2016).

[22] K. Olejník, V. Schuler, X. Marti, V. Novák, Z. kaspar, P. Wadley, R. P. Campion, K. W. Edmonds, B. L. Gallagher, J. Garces, M. Baumgartner, P. Gambardella, and T. Jungwirth, Antiferromagnetic CuMnAs multi-level memory cell with microelectronic compatibility. *Nat. Commun.* **8**, 15434 (2017).

[23] L. Šmejkal, T. Jungwirth, and J. Sinova, Route towards Dirac and Weyl antiferromagnetic spintronics. *Phys. Stat. Sol.* **11**, 1700044 (2017).

[24] L. Šmejkal, Y. Mokrousov, B. Yan, and A. H. MacDonald, Topological antiferromagnetic spintronics. *Nat. Phys.* **14**, 242 (2018).

[25] R. S. K. Mong, A. M. Essin, and J. E. Moore, Antiferromagnetic topological insulators. *Phys. Rev. B* **81**, 245209 (2010).

[26] H. Chen, Q. Niu, and A. H. MacDonald, Anomalous Hall effect arising from noncollinear antiferromagnetism. *Phys. Rev. Lett*. **112**, 017205 (2014).

[27] J. Kübler and C. Felser, Non-collinear antiferromagnets and the anomalous Hall effect. *EPL* **108**, 67001 (2014).

[28] S. Nakatsuji, N. Kiyohara, and T. Higo, Large anomalous Hall effect in a non-collinear antiferromagnet at room temperature. *Nature* **527**, 212 (2015).

[29] A. K. Nayak, J. E. Fischer, Y. Sun, B. Yan, J. Karel, A. C. Komarek, C. Shekhar, N. Kumar, W. Schnelle, J. Kübler, C. Felser, and S. P. P. Parkin, Large anomalous Hall effect driven by a nonvanishing Berry curvature in the noncollinear antiferromagnet Mn_3Ge. *Sci. Adv.* **2**, e1501870 (2016).

[30] Y. Zhang, Y. Sun, H. Yang, J. Železný, S. P. P. Parkin, C. Felser, and B. Yan, Strong anisotropic anomalous Hall effect and spin Hall effect in the chiral antiferromagnetic compounds Mn_3X (X = Ge, Sn, Ga, Ir, Rh, and Pt). *Phys. Rev. B* **95**, 075128 (2017).

[31] G. Gurung, D.-F. Shao, T. R. Paudel, and E. Y. Tsymbal, Anomalous Hall conductivity of non-collinear magnetic antiperovskites. *Phys. Rev. Mater.* **3**, 044409 (2019).

[32] D. Boldrin, I. Samathrakis, J. Zemen, A. Mihai, B. Zou, B. Esser, D. McComb, P. Petrov, H. Zhang, and L. F. Cohen, The anomalous Hall effect in non-collinear antiferromagnetic Mn_3NiN thin films. *Phys. Rev. Mater.* **3**, 094409 (2019).

[33] X. Zhou, J.-P. Hanke, W. Feng, F. Li, G.-Y. Guo, Y. Yao, S. Blügel, and Y. Mokrousov, Spin-order dependent anomalous Hall effect and magneto-optical effect in the noncollinear antiferromagnets Mn_3XN with X = Ga, Zn, Ag, or Ni. *Phys. Rev. B* **99**, 104428 (2019).

[34] K. Zhao, T. Hajiri, H. Chen, R. Miki, H. Asano, and P. Gegenwart, Anomalous Hall effect in the noncollinear antiferromagnetic antiperovskite $Mn_3Ni_{1-x}Cu_xN$. *Phys. Rev. B* **100**, 045109 (2019).

[35]Y. You, H. Bai, X. Chen, Y. Zhou, X. Zhou, F. Pan, and C. Song, Room temperature anomalous Hall effect in antiferromagnetic Mn_3SnN films. *Appl. Phys. Lett*. **117**, 222404 (2020).

[36] X. Li, A. H. MacDonald, and H. Chen, Quantum anomalous Hall effect through canted antiferromagnetism. *arXiv*:1902.10650 (2019).

[37] N. J. Ghimire, A. S. Botana, J. S. Jiang, J. Zhang, Y.-S. Chen, and J. F. Mitchell, Large anomalous Hall effect in the chiral-lattice antiferromagnet $CoNb_3S_6$. *Nat. Commun.* **9**, 3280 (2018).

[38] L. Šmejkal, R. González-Hernández, T. Jungwirth, and J. Sinova, Crystal time-reversal symmetry breaking and spontaneous Hall effect in collinear antiferromagnets. *Sci. Adv.* **6**, eaaz8809 (2020).

[39] D. F. Shao, J. Ding, G. Gurung, S. H. Zhang, and E. Y. Tsymbal, interfacial crystal hall effect reversible by ferroelectric polarization. *Phys. Rev. Applied* **15**, 024057 (2021).

[40] K. Samanta, M. Ležaić, M. Merte, F. Freimuth, S. Blügel, and Y. Mokrousov, Crystal Hall and crystal magneto-optical effect in thin films of $SrRuO_3$. *J. Appl. Phys.* **127**, 213904 (2020).

[41] J. Kipp, K. Samanta, F. R. Lux, M. Merte, D. Go, J.-P. Hanke, M. Redies, F. Freimuth, S. Blugel, M. Lezaic, and Y. Mokrousov, The chiral Hall effect in canted ferromagnets and antiferromagnets. *Commun. Physics* **4**, 99 (2021).

[42] M. Ikhlas, T. Tomita, T. Koretsune, M.-T. Suzuki, D. Nishio-Hamane, R. Arita, Y. Otani, and S. Nakatsuji, Large anomalous Nernst effect at room temperature in a chiral antiferromagnet. *Nat. Phys.* **13**, 1085 (2017).

[43] W. Zhang, M. B. Jungfleisch, W. Jiang, J. E. Pearson, A. Hoffman, F. Freimuth, and Y. Mokrousov, Spin Hall effects in metallic antiferromagnets. *Phys. Rev. Lett.* **113,** 196602 (2014).

[44] W. Zhang, M. B. Jungfleisch, F. Freimuth, W. Jiang, J. Sklenar, J. E. Pearson, J. B. Ketterson, Y. Mokrousov, and A. Hoffman, All-electrical manipulation of magnetization dynamics in a ferromagnet by antiferromagnets with anisotropic spin Hall effects. *Phys. Rev. B* **92**, 144405 (2015).

[45] J. B. S. Mendes, R. O. Cunha, O. A. Santos, P. R. T. Ribeiro, F. L. A. Machado, R. L. Rodriquez-Suàrez, A. Azevedo, and S. M. Rezende, Large inverse spin Hall effect in the antiferromagnetic metal $Ir_{20}Mn_{80}$. *Phys. Rev. B* **89**, 140406 (2014).

[46] J. Železný, Y. Zhang, C. Felser, and B. Yan, Spin-polarized current in noncollinear antiferromagnets. *Phys. Rev. Lett.* **119**, 187204 (2017).

[47] M. Kimata, H. Chem, K. Kondou, S. Sugimoto, P. K. Muduli, M. Ikhlas, Y. Omori, T. Tomita, A. H. MacDonald, S. Nakatsuji, and Y. Otani, Magnetic and magnetic inverse spin Hall effects in a non-collinear antiferromagnet. *Nature* **565**, 627 (2019).

[48] A. Mook, R. R. Neumann, A. Johansson, J. Henk, and I. Mertig, Origin of the magnetic spin Hall effect: Spin current vorticity in the Fermi sea. *Phys. Rev. Research* **2**, 023065 (2020).

[49] R. González-Hernández, L. Šmejkal, K. Výborný, Y. Yahagi, J. Sinova, T. Jungwirth, and J. Železný, Efficient electrical spin-splitter based on non-relativistic collinear antiferromagnetism. *Phys. Rev. Lett.* **126**, 127701 (2021).

[50] M. Naka, S. Hayami, H. Kusunose, Y. Yanagi, Y. Motome, and H. Seo, Spin current generation in organic antiferromagnets. *Nat. Commun.* **10**, 4305 (2019).

[51] A. S. Núñez, R. A. Duine, P. Haney, and A. H. MacDonald, Theory of spin torques and giant magnetoresistance in antiferromagnetic metals. *Phys. Rev. B* **73**, 214426 (2006).

[52] B. G. Park, J. Wunderlich, X. Marti, V. Holy, Y. Kurosaki, M. Yamada, H. Yamamoto, A. Nishide, J. Hayakawa, H. Takahashi, A. B. Shick, and T. Jungwirth, A spin-valve-like magnetoresistance of an antiferromagnet-based tunnel junction. *Nat. Mater.* **10**, 347 (2011).

[53] X. Martí, B. G. Park, J. Wunderlich, H. Reichlova, Y. Kurosaki, M. Yamada, H. Yamamoto, A. Nishide, J. Hayakawa, H. Takahashi, and T. Jungwirth, Electrical measurement of antiferromagnetic moments in exchange-coupled IrMn/NiFe stacks. *Phys. Rev. Lett.* **108**, 017201 (2012).

[54] X. Martí, I. Fina, and T. Jungwirth, Prospect for antiferromagnetic spintronics. *IEEE trans. Magn.* **51** 2900104 (2015).

[55] V. Tshitoyan, C. Ciccarelli, A. P. Mihal, M. Ali, A. C. Irvine, T. A. Moore, T. Jungwirth, and A. J. Ferguson, Electrical manipulation of ferromagnetic NiFe by antiferromagnetic IrMn. *Phys. Rev.* B **92**, 214406 (2021).

[56] W. H. Meiklejohn and C. P. Bean, New magnetic anisotropy. *Phys. Rev.***102**, 1413 (1956).

[57] M. D. Stiles, R. D. McMichael, Model for exchange bias in polycrystalline ferromagnet-antiferromagnet bilayers. *Phys. Rev. B* **59**, 3722 (1999).

[58] X. Chen, X. Zhou, R. Cheng, C. Song, J. Zhang, Y. Wu, Y. Ba, H. Li, Y. Sun, Y. You, Y. Zhao, and F. Pan, Electric field control of Néel spin-orbit torque in an antiferromagnet. *Nat. Mater.* **18**, 931 (2019).

[59] H. Yan, Z. Feng, S. Shang, X. Wang, Z. Hu, J. Wang, Z. Zhu, H. Wang, Z. Chen, H. Hua, W. Lu, J. Wang, P. Qin, H. Guo, X. Zhou, Z. Leng, Z. Liu, C. Jiang, M. Coey, and Z. Liu, A piezoelectric, strain-controlled antiferromagnetic memory insensitive to magnetic fields. *Nat. Nanotech.* **14**, 131 (2019).

[60] X. He, Y. Wang, N. Wu, A. N. Caruso, E. Vescovo, K. D. Belaschenko, P. A. Dowben, and C. Binek, Robust isothermal electric control of exchange bias at room temperature. *Nat. Mater.* **9**, 579(2010).

[61] T. Kosub, M. Kopte, R. Huhne, P. Appel, B. Shields, P. Maletinsky, R. Hubner, M. O. Liedke, J. Fassbender, O. G. Schmidt, and D. Makarov, Purely antiferromagnetic magnetoelectric random access memory. *Nat. Commun.* **8**, 13985 (2017).

[62] A. Mahmood, W. Echtenkamp, M. Street, J.-L. Wang, S. cao, T. Komesu, P. A. Dowben, P. Buragohain, H. Lu, A. Gruverman, A. Parthasarathy, S. Rakheja, and C. Binek, Voltage controlled Néel vector rotation in zero magnetic field. *Nat. Commun.* **12**, 1674 (2021).

[63] A. V. Kimel, A. Kirilyuk, A. Tsvetkov, R. V. Pisarev, and Th. Rasing, Laser-induced ultrafast spin reorientation in the antiferromagnet $TmFeO_3$. *Nature* **429**, 850 (2004).

[64] C. Song, Y. You, X. Chen, X. Zhou, Y. Wang, and F. Pan, How to manipulate magnetic states of antiferromagnets. *Nanotech.* **29**, 112001 (2018).

[65] G. R. Hoogeboom, A. Aqeel, T. Kuschel, T. T. M. Palstra, and B. J. van Wees, Negative spin Hall magnetoresistance of Pt on the bulk easy-plane antiferromagnet NiO. *Appl. Phys. Lett.* **111**, 052409 (2017).

[66] A. A. Sapozhnik, R. Abrudan, Y. Skourski, M. Jourdan, H. Zabel, M. Kläui, and H. -J. Elmers, Manipulation of antiferromagnetic domain distribution in Mn_2Au by ultrathin magnetic fields and by strain. *Phys. Stat. Solidi* **11**, 1600438 (2017).

[67] Y. Y. Wang, C. Song, B. Cui, G. Y. Wang, F. Zeng, and F. Pan, Room-temperature perpendicular exchange coupling and tunnelling anisotropic magnetoresistance in an antiferromagnet-based tunnel junction. *Phys. Rev. Lett.* **109**, 137201 (2012).

[68] A. Scholl, M. Liberati, E. Arenholz, H. Ohldag, and J. Stöhr, Creation of an antiferromagnetic exchange spring. *Phys. Rev. Lett.* **92**, 247201 (2004).

[69] J. Li, A. Tan, S. Ma, R. F. Yang, E. Arenholz, C. Hwang, and Z Q. Qiu, Chirality switching and winding or unwinding of the antiferromagnetic NiO domain walls in Fe.NiOFe/CoO/Ag(001). *Phys. Rev. Lett.* **113**, 147207 (2014).

[70] H. Reichlová, V. Novak, Y. Kurosaki, M. Yamada, H. Yamamoto, A. Nishide, J. Hayakawa, H. Takahashi, M. Marysko, and J. Wunderlich, Temperature and thickness dependence of tunnelling anisotropic magnetoresistance in exchange-biased Py/IrMn/MgO/Ta stacks. *Mat. Res. Express* **3**, 076406 (2016).

[71] X. Marti, I. Fina, C. Frontera, J. Liu, P. Wadley, Q. He, R. J. Paull, J. D. Clarkshon, J. Kudrnovský, I. Turek, J. Kunes, D. Yi, J-H. Chu, C. T. Nelson, L. You, E. Arenholz, S. Salahuddin, J. Fontcuberta, T. Jungwirth, and R. Ramesh, Room-temperature antiferromagnetic memory resistor. *Nat. Mater.* **13**, 367 (2014).

[72] D. Petti, E. Albisetti, H. Reichlova, J. Gazquez, M. Varela, M. Molina-Ruiz, A. F. Lopeandia, K. Olejnik, V. Novak, I. Fina, B. Dkhil, J. Hayakawa, X. Marti, J. Wunderlich, T. Jungwirth, and R. Bertacco, Storing magnetic information in

IrMn/MgO/Ta tunnel junctions via field-cooling. *Appl. Phys. Lett.* **102**, 192404 (2013).

[73] A. V. Kimel, A. Kirilyuk, A. Tsvetkov, R. V. Pisarev, and th. Rasing, Laser-induced ultrafast spin reorientation in the antiferromagnet $TmFeO_3$. *Nat.* **429**, 850 (2004).

[74] S. Manz, M. Matsubara, T. Lottermoser, J. Bü chi, A. Iyama, T. Kimura, D. Meier, and M. Fiebig, Reversible optical switching of antiferromagnetism in $TbMnO_3$. *Nat. Phot.* **10**, 653 (2016).

[75] A. V. Kimel, B. A. Ivanov, R. V. Pisarev, P. A. Usacehv, A. Kirilyuk, and Th. Rasing, Inertia-driven spin switching in antiferromagnets. *Nat. Phys.* **5**, 727 (2009).

[76] A. B. Shick, S. Khmelevskyi, O. N. Mryasov, J. Wunderlich, and T. Jungwirth, Spin-orbit coupling induced anisotropy effects in bimetallic antiferromagnets: A route towards antiferromagnetic spintronics. *Phys. Rev. B* **81**, 212409 (2010).

[77] A. X. Gray, D. W. Cooke, P. Kruger, C. Bordel, A. M. Kaiser, S. Moyerman, E. E. Fullerton, S. Ueda, Y. Yamashita, A. Gloskovskii, C. M. Schneider, W. Drube, K. Kobayashi, F. Hellman, and C. S. Fadley, Electronic structure changes across the metamagnetic transition in FeRh via hard x-ray photoemission. *Phys. Rev. Lett.* **108**, 257208 (2012).

[78] C. Bordel, J. Juraszek, D. W. Cooke, C. Baldasseroni, S. Mankovsky, J. Minar, H. Ebert, S. Moyerman, E. E. Fullerton, and F. Hellman, Fe spin reorientation across the metamagnetic transition in strained FeRh thin films. *Phys. Rev. Lett.* **109**, 1172021 (2012).

[79] R. O. Cherifi, V. Ivanovskaya, L. C. Phillips, A. Zobelli, I. C. Infante, E. Jacquet, V. Garcia, S. Fusil, P. R. Briddon, N. Guiblin, A. Mougin, A. A. Unal, F. Kronast, S.

Valencia, B. Dkhil, A. Barthelemy, and M. Bibes, Electric-field control of magnetic order above room temperature. *Nat. Mater.* **13**, 345 (2014).

[80] I. Suzuki, M. Itoh, and T. Taniyama, Elastically controlled magnetic phase transitionin ga-FeRh/$BaTiO_3$(001) heterostructure. *Appl. Phys. Lett.* **104**, 022401 (2014).

[81] Y. Wang, X. Zhou, C. Song, Y. Yan, S. Zhou, G. Wang, C. Chen, F. Zeng, and F. Pan, Electrical control of the exchange spring in antiferromagnetic metals. *Adv. Mat.* **27**, 3196 (2015).

[82] H. Yan, Z. Feng, S. Shang, X. Wang, Z. Hu, J. Wang, Z. Zhu, H. Wang, Z. Chen, H. Hua, W. Lu, J. Wang, P. Qin, H. Guo, X. Zhou, Z. Leng, Z. Liu, C. Jiang, M. Coey, and Z. Liu, A piezoelectric, strain-controlled antiferromagnetic memory insensitive to magnetic fields. *Nat. Nanotech.* **14**, 131 (2019).

[83] J. C. Slonczewski, Current-driven excitation of magnetic multilayers. *J. Magn. Magn. Mater.* **159,** L1 (1996).

[84] L. Berger, Emission of spin waves by a magnetic multilayer traversed by a current. *Phys. Rev. B* **54**, 9353 (1996).

[85] S. Zhang and Z. Li, Roles of nonequilibrium conduction electrons on the magnetization dynamics of ferromagnets. *Phys. Rev. Lett.* **93**, 127204 (2004).

[86] D. C. Ralph and M. D. Stiles, Spin transfer torques. *J. Magn. Magn. Mater.* **320**, 1190 (2008).

[87] H. V. Gomonay and V. M. Loktev, Spin transfer and current-induced switching in antiferromagnets. *Phys. Rev. B* **81**, 144427 (2010).

[88] H. B. M. Saidaoui, A. Manchon, and X. Waintal, Spin transfer torque in antiferromagnetic spin valves: From clean to disordered regimes. *Phys. Rev. B* **89**, 174430 (2014).

[89] P. Merodio, A. Kalitsov, H. Ba, V. Baltz, and M. Chshiev, Spin-dependent transport in antiferromagnetic tunnel junctions. *Appl. Phys. Lett*. **105**, 122403 (2014).

[90] M. Stamenova, R. Mohebbi, J. Seyed-Yazdi, I. Rungger, and S. Sanvito, First-principles spin-transfer torque in CuMnA|GaP|CuMnAs junctions. *Phys. Rev. B* **95**, 060403 (2017).

[91] V. M. Edelstein, Spin polarization of conduction electrons induced by electric current in two-dimensional asymmetric electron systems. *Sol. State Commun.* **73**, 233 (1990).

[92] A. Manchon and S. Zhang, Theory of nonequilibrium intrinsic spin torque in a single nanomagnet. *Phys. Rev. B* **78**, 212405 (2008).

[93] A. Manchon and S. Zhang, Theory of spin torque due to spin-orbit coupling. *Phys. Rev. B* **79**, 094422 (2009).

[94] A. Chernyshov, M. Overby, X. Liu, J. K. Furdyna, Y. L.-Geller, and L. P. Rokhinson, Evidence for reversible control of magnetization in a ferromagnetic material by means of spin-orbit magnetic field. *Nat. Phys.* **5**, 656 (2009).

[95] J. Zelezny, H. Gao, K. Vyborny, J. Zemen, J. Masek, A. Manchon, J. Wunderlich, J. Sinova, and T. Jungwirth, Relativistic Néel-order fields induced by electrical current in antiferromagnets. *Phys. Rev. Lett.* **113**, 157201 (2014).

[96] S. Y. Bodnar, L. Smejkal, I. Turek, T. Jungwirth, O. Gomonay, J. Sinova, A. A. Sapozhnik, H. -J. Elmers, M. Klaui, and M. Jourdan, Writing and reading

antiferromagnetic Mn_2Au by Néel spin-orbit torques and large anisotropic magnetoresistance. *Nat. Commun.* **9**, 348 (2018).

[97] H. Reichlová, D. Kriegner, V. Holy, K. Olejnik, V. Novak, M. Yamada, K. Miura, S. Ogawa, H. Takahashi, T. Jungwirth, and J. Wunderlich, Current induced torques in structures with ultra-thin IrMn antiferromagnet. *Phys. Rev. B* **92**, 165424 (2015).

[98] T. Moriyama, K. Oda, T. Ohkochi, M. Kimata, and T. Ono, Spin torque control of antiferromagnetic moments in NiO. *Sci. Rep.* **8**, 14167 (2018).

[99] E. V. Gomonaĭ and V. M. Loktev, Distinctive effects of a spin-polarized current on the static and dynamic properties of an antiferromagnetic conductor. *Low. Temp. Phys.* **34**, 198 (2008).

[100] H. V. Gomonay and V. M. Loktev, Spin transfer and current-induced switching in antiferromagnets. *Phys. Rev. B* **81**, 144427 (2010).

[101] A. H. MacDonald, and M. Tsoi, Antiferromagnetic metal spintronics. *Phil. Trans. R. Soc. A* **369**, 3098 (2011).

[102] P. M. Haney, D. Waldron, R. A. Duine, A. S. Núñez, H. Guo, and A. H. MacDonald, *Ab initio* giant magnetoresistance and current-induced torques in Cr/Au/Cr multilayers. *Phys. Rev. B* **75**, 74428 (2007).

[103] R. A. Duine, P. M. Haney, A. S. Núñez, and A. H. MacDonald, Inelastic scattering in ferromagnetic and antiferromagnetic spin valves. *Phys. Rev. B* **75**, 014433 (2007).

[104] Z. Wei, A. Sharma, J. Bass, and M. Tsoi, Point-contact search for antiferromagnetic giant magnetoresistance. *J. Appl. Phys.* **105**, 07D113 (2009).

[105] L. Wang, S. G. Wang, S. Rizwan, H. Q. Qin, and X. F. Han, Magnetoressitance effect in antiferromagnet/nonmagnet/antiferromagnet multilayers. *Appl. Phys. Lett.* **95**, 152512 (2009).

[106] S. Urazhdin and N. Anthony, Effect of polarized current on the magnetic state of an antiferromagnet. *Phys. Rev. Lett.* **99**, 046602 (2007).

[107] H.-C. Wu, M. Abid, A. Kalitsov, P. Zarzhitsky, M. Abid, Z.-M. Liao, C. O. Coilean, H. Xu J.-J. Wang, H. Lu, O. N. Mryasov, C.-R. Chang, and I. V. Shvets, Anomalous anisotropic magnetoresistance of antiferromagnetic epitaxial bimetallic films: Mn_2Au and Mn_2Au/Fe bilayers. *Adv. Func. Mater.* **26**, 5884 (2016).

[108] I. Fina, X. Marti, D. Yi, J. Liu, J. H. Chu, C. R.-Searro, S. Suresha, A. B. Shick, J. Zelezny, T. Jungwirth, J. Fontcuberta, and R. Ramesh, Anisotropic magnetoresistance in an antiferromagnetic semiconductor. *Nat. Commun.* **5**, 4671 (2014).

[109] C. Gould, C. Ruster, T. Jungwirth, E. Girgis, G. M. Schott, R. Giraud, K. Brunner, G. Schmidt, and L. W. Molenkamp, Tunnelling anisotropic magnetoresistance: A spin-valve-like tunnel magnetoresistance using a single magnetic layer. *Phys. Rev. Lett.* **93**, 117203 (2004).

[110] L. Brey, C. Tejedor, and J. Fernández-Rossier, Tunnel magnetoresistance in GaMnAs: Going beyond Jullière formula. *Appl. Phys. Lett.* **85**, 1996 (2004).

[111] A. B. Shick, F. Máca, J. MaŠek, and T. Jungwirth, Prospect for room temperature tunnelling anisotropic magnetoresistance effect: Density of states anisotropies in CoPt systems. *Phys. Rev. B* **73**, 024418 (2006).

[112] L. Gao, X. Jaing, S.-H. Yang, J. D. Burton, E. Y. Tsymbal, and S. S. P. Parkin, Bias voltage dependence of tunnelling anisotropic magnetoresistance in magnetic

tunnel junctions with MgO and Al_2O_3 tunnel barriers. *Phys. Rev. Lett.* **99**, 226602 (2007).

[113] Y. Y. Wang, C. Song, B. Cui, G. Y. Wang, F. Zeng, and F. Pan, Room-temperature perpendicular exchange coupling and tunnelling anisotropic magnetoresistance in an antiferromagnet-based tunnel junction. *Phys. Rev. Lett.* **109**, 137201 (2012).

[114] Y. Y. Wang, C. Song, G. Y. Wang, F. Zeng, and F. Pan, Evidence for asymmetric rotation of spins in antiferromagnetic exchange-spring. *New J. Phys.* **16**, 123032 (2014).

[115] X. Z. Chen R. Zarzuela, J. Zhang, C. Song, X. F. Zhou, G. Y. Shi, F. Li, H. A. Zhou, W. J. Jiang, F. Pan, and Y. Tserkovnyak, Antidamping-Torque-Induced switching in biaxial antiferromagnetic insulators. *Phys. Rev. Lett.* **120**, 207204 (2018).

[116] Y.-T. Chen, S. Takahashi, H. Nakayama, M. Althammer, S. T. B. Goennenwein, E. Saitoh, and G. E. W. Bauer, Theory of spin Hall magnetoresistance. *Phys. Rev. B* **87**, 144411 (2013).

[117] J. Fischer, O. Gomonay, R. Schlitz, K. Ganzhorn, N. Vlietstra, M. Althammer, H. Huebi, M. Opel, R. Gross, S. T. B. Goennwein, and S. Geprags, Spin Hall magnetoresistance in antiferromagnet/heavy-metal heterostructures. *Phys. Rev. B* **97**, 014417 (2018).

[118] C. C. Chiang, S. Y. Huang, D. Qu, P. H. Wu, and C. L. Chien, Absence of evidence of electrical switching of the antiferromagnetic Néel vector. *Phys. Rev. Lett.* **123**, 227203 (2019).

[119] Z. Feng, X. Zhou, L. Smejkal, L. Wu, Z. Zhu, H. Guo, R. G.-Hernandez, X.Wang, H. Yan, P. Qin, X. Zhang, H. Wu, H. Chen, Z. Xia, C. Jiang, M. Coey, J. Sinova, T. Jungwirth, and Z. Liu, Observation of the anomalous Hall effect in a collinear antiferromagnet. *arxiv:*2002.08712 (2020).

[120] I. Sodemann and L. Fu, Quantum nonlinear Hall effect induced by Berry curvature dipole in time-reversal invariant materials. *Phys. Rev. Lett.* **115**, 216806 (2015).

[121] Q. Ma, S.-Y. Xu, H. Shen, D. MacNeill, V. Fatemi, T.-R. Chang, A. M. Mier Valdivia, S. Wu, Z. Du, C.-H. Hsu, S. Fang, Q. D. Gibson, K. Watanabe, T. Taniguchi, R. J. Cava, E. Kaxiras, H.-Z. Lu, H. Lin, L. Fu, N. Gedik, and P. J.-Herrero, Observation of the nonlinear Hall effect under time-reversal-symmetric conditions. *Nature* **565**, 337 (2019).

[122] K. Kang, T. Li, E. Sohn, J. Shan, and K. F. Mak, Nonlinear anomalous Hall effect in few-layer WTe_2. *Nat. Mater.* **18**, 324 (2019).

[123] D.F. Shao, S. -H. Zhang, G. Gurung, W. Yang, and E. Y. Tsymbal, Nonlinear anomalous Hall effect for Néel vector detection. *Phys. Rev. Lett.* **124**, 067203 (2020).

[124] D. Fruchart and E. F. Bertaut, Magnetic studies of the metallic perovskite-type compounds of manganese. *J. Phys. Soc. Jap.* **44**, 781 (1978).

[125] E. F. Bertaut, D. Fruchart, J. P. Bouchaud, and R. Fruchart, Diffraction neutronique de Mn_3GaN. *Sol. St. Commun.* **6**, 251 (1968).

[126] K. Takenaka, T. Inagaki, and H. Takagi, Conversion of magnetic structure by slight dopants in geometrically frustrated antiperovskite Mn_3GaN. *Appl. Phys. Lett.* **95**, 132508 (2009).

[127] Y. Wang, H. Zhang, J. Zhu, X. Liu, S. Li, R. Zou, and Y. Zhao, Antiperovskites with exceptional functionalities. *Adv. Mater.* **32**, 1905007 (2020).

[128] T. He, Q. Huang, A. P. Ramirez, Y. Wang, K. A. Regan, N. Rogado, M. A. Hayward, M. K. Haas, J. S. Slusky, K. Inumara, H. W. Zandbergen, N. P. Ong, and R. J. Cava, Superconductivity in the non-oxide perovskite $MgCNi_3$. *Nature* **411**, 54 (2001).

[129] K. Kamishima, T. Goto, H. Nakagawa, N. Miura, M. Ohashi, N. Mori, T. Sasaki, and T. Kanomata, Giant magnetoresistance in the intermetallic compound Mn_3GaC. *Phys. Rev. B* **63**, 024426 (2000).

[130] T. Kaneko, T. Kanomata, and K. Shirakawa, Pressure effect on the magnetic transition temperatures in the intermetallic compounds Mn_3MC (M = Ga, Zn and Sn). *J. Phys. Soc. Jap.* **56**, 4047 (1987).

[131] K. Takenaka, M. Ichigo, T. Hamada, A. Ozawa, T. Shibayama, T. Inagaki, and K. Asano, Magnetovolume effects in manganese nitrides with antiperovskite structure. *Sci. Tech. Adv. Mat.* **15**, 015009 (2014).

[132] T. Tohei, H. Wada, and T. Kanomata, Negative magnetocaloric effect at the antiferromagnetic to ferromagnetic transition of Mn_3GaC. *J. Appl. Phys.* **94**, 1800 (2003).

[133] B. S. Wang, P. Tong, Y. P. Sun, X. Luo, X. B. Zhu, G. Li, X. D. Zhu, S. B. Zhang, Z. R. Yang, and W. H. Song, Large magnetic entropy change near room temperature in antiperovskite $SnCMn_3$. *EPL* **85**. 47004 (2009).

[134] P. Lukashev, R. F. Sabirianov, and K. Belashchenko, Theory of piezomagnetic effect in Mn-based antiperovskites. *Phys. Rev. B* **78**, 184414 (2008).

[135] J. Zemen, Z. Gercsi, and K. G. Sandeman, Piezomagnetism as a counterpart of the magnetovolume effect in magnetically frustrated Mn-based antiperovskite nitrides. *Phys. Rev. B* **96**, 024451 (2017).

[136] D. Boldrin, A. P. Mihai, B. Zou, J. Zemen, R. Thompson, E. Ware, B. V. Neamtu, L. Ghivelder, B. Esser, D. W. McComb, P. Petrov, and L. F. Cohen., Giant piezomagnetism in Mn_3NiN. *ACS Appl. Mater. & Int.* **10**, 18863 (2018).

[137] D. Matsunami, A. Fujita, K. Takenaka, and M. Kano, Giant barocaloric effect enhanced by the frustration of the antiferromagnetic phase in Mn_3GaN. *Nat. Mater.* **14**, 73 (2015).

[138] H. K. Singh, I. Samathrakis, N. M. Fortunato, J. Zemen, C. Shen, O. Gutfleisch, and H. Zhang, Multifunctional antiperovskites driven by strong magnetostructural coupling. *npj Comput Mater* **7**, 98 (2021).

[139] K. Shi, Y. Sun, J. Yan, S. Deng, L. Wang, H. Wu, P. Hu, H. Lu, M. I. Malik, Q. Huang, and C. Wang, Baromagnetic effect in antiperovsktie $Mn_3Ga_{0.95}N_{0.94}$ by neutron powder diffraction analysis. *Adv. Mater.* **28**, 3761 (2016).

[140] S. Likubo, K. Kodama, K. Takenaka, H. Takagi, and S. Shamoto, Magnetovolume effect in $Mn_3Cu_{1-x}Ge_xN$ related to the magnetic structure: Neutron powder diffraction measurements. *Phys. Rev. B* **77**, 020409 (2008).

[141] V. T. N. Huyen, M. -T. Suzuki, K. Yamauchi, and T. Oguchi, Topology analysis for anomalous Hall effect in the noncollinear antiferromagnetic states of Mn_3AN (A = Ni, Cu, Zn, Ga, Ge, Pd, In, Sn, Ir, Pt). *Phys. Rev. B* **100**, 094426 (2019).

[142] S. M. L. Teicher, I. K. Svenningsson, L. M. Schoop, and R. Seshadri, Weyl nodes and magnetostructural instability in antiperovskite Mn_3ZnC. *APL Mater.* **7**, 121104 (2019).

[143] X. Zhou, J.-P. Hanke, W. Feng, F. Li, G.-Y. Guo, Y. Yao, S. Blügel, and Y. Mokrousov, Spin-order dependent anomalous Hall effect and magneto-optical effect in the noncollinear antiferromagnets Mn_3XN with X = Ga, Zn, Ag, or Ni. *Phys. Rev.* B **99***,* 104428 (2019).

Chapter 2 Theoretical Methods

Properties of the condensed matter systems consisting of many electrons and ions can be found by solving the Schrödinger equation exactly. But the complexity of the exact solution of this many-body problem increases with increase in the number of electrons and ions. Protons are about 1800 times heavier than the electron and hence, the motion of the ions (protons + neutrons) in the real system can be frozen compared to the fast-moving electron. This approximation is well known as the Born-Oppenheimer (BO) approximation [1]. This approximation reduces the problem to that of the system where electrons move under the external potential produced by the frozen ions. The electronic Hamiltonian then is given by

$$\hat{H} = -\sum_i \frac{\hbar^2}{2m}\nabla_i^2 + \sum_i \sum_{j\neq i} \frac{1}{4\pi\epsilon_0 |\vec{r}_i - \vec{r}_j|} - \sum_A \sum_i \frac{Z_A}{|R_A - r_i|} = \hat{T}_e + \hat{V}_{ee} + \hat{V}_{Ne}\,, \quad (2.1)$$

where $\hat{T}_e$ is the kinetic energy operator of the electrons, $\hat{V}_{ee}$ is the electron-electron correlation, $\hat{V}_{Ne} = \sum_i \hat{v}_{ext}$ is the coulomb potential of the nuclei and any external potential acting on the electrons.

The BO approximation decouples the electron and nuclei motions but still the number of electrons is very large. In addition, the quantum nature of electrons and electron-electron correlations makes the solution of the many-body Schrödinger equation very complicated. Several methods have been developed to simplify the Hamiltonian. In particular, the Hartree-Fock (HF) approximation takes into account the fermionic nature of the electron and uses the Slater determinant wavefunction which respects the Pauli exclusion principle [1– 3]. The HF approximation reduces the many-body Schrödinger

equation into a single-particle Schrödinger equation. This equation can be solved by variational self-consistent iterations. But the main problem is that HF fails to account for electron-electron correlations [2, 3].

Within the HF approximation utilizes an approach based on the wave function. The wavefunction of the electronic Hamiltonian consisting of N electrons is dependent upon the 4N variables (3 spatial and one spin for each of the electrons). The number of the variables can be reduced if we solve the Schrödinger equation using the electron density. The electron density depends only upon 3 spatial variables and is defined as

$$n(\vec{r}) =< \psi(\vec{r}_1, \dots \vec{r}_N, s_1 \dots s_N)|\, \hat{n}(r) |\psi(\vec{r}_1, \dots \vec{r}_N, s_1 \dots s_N) >, \qquad (2.2)$$

where $\hat{n}(r)$ is the electron density operator, ψ is the wavefunction with spatial variable $\vec{r}_i$ and spin variable s_i. Moreover, the electron density, unlike the wavefunction, can be determined experimentally. The theoretical methods utilizing the electron density are known as density functional theory (DFT). DFT methods are known to be accurate and providing high accuracy in computations. Therefore, in this work, we apply the DFT methods to solve the nonrelativistic Schrödinger equation. The relativistic part is added as a perturbation to solve the relativistic Schrödinger equation. Below, we give an overview of the DFT methods which are used in this work.

2.1. Density Functional Theory

DFT uses the density of electrons as the basic variable to find the ground state of the condensed matter system described by the single-particle electronic Hamiltonian. Electron density describes the distribution of electrons in the system and indirectly includes the information of the atomic number of the ions. The Hohenberg-Kohn theorem

[4] and the Kohn-Sham approach [5] are central in the DFT showing that the ground state energy of the interacting system can be found in terms of the electron density.

2.1.1. Hohenberg-Kohn Theorem

The electronic Hamiltonian in Eq. (2.1) consists of the kinetic energy operator, electron-electron correlation term, and external potential v_{ext} due to the nuclei and the external field. The application of the DFT is possible if we can define an energy functional in terms of the electron density. The Hohenberg-Kohn (HK) theorem shows that the ground state electron density can determine this external potential. The HK theorem consists of two parts which explain how to express the v_{ext} in terms of the ground state electron density.

HK Theorem I: The ground state energy is a unique functional of the ground state electron density $n_0(\vec{r})$.

Proof: Consider two different external potentials v_{ext}^{A} and v_{ext}^{B} with ground state wavefunctions ψ^A and ψ^B and energy E^A and E^B respectively. The ground state energy is defined by

$$E^i = \langle \psi^i | \hat{T}_e + \hat{V}_{ee} + \hat{V}_{ext}^i | \psi^i \rangle = \langle \psi^i | \hat{F} + \hat{V}_{ext}^i | \psi^i \rangle, i = A, B , \qquad (2.3)$$

where $\hat{F}$ is the universal functional because it has the same form for all N electron systems and $\hat{V}_{ext}^i = \sum_j v_{ext}^i(\vec{r}_j)$. Consider that these states are not degenerate, *i.e.*, $\psi^A \neq \psi^B$, but the ground state electron density is same $n^A = n^B = n_0$. Ground state energy for the electronic Hamiltonian with potential v_{ext}^i is lower than the energy determined with the trial function ψ^j, *i.e.*

$$E^i = \langle \psi^i | \hat{F} + \hat{V}^i_{ext} | \psi^i \rangle < \langle \psi^j | \hat{F} + \hat{V}^j_{ext} | \psi^i \rangle, i \neq j = A, B$$

$$E^i < \langle \psi^j | \hat{F} + \hat{V}^j_{ext} | \psi^j \rangle + \langle \psi^j | \hat{V}^i_{ext} - \hat{V}^j_{ext} | \psi^j \rangle,$$

$$E^i < E^j + \int d\vec{r} n_0(\vec{r}) \left(\hat{V}^i_{ext} - \hat{V}^j_{ext} \right). \quad (2.4)$$

Adding Eq. (2.4) with $(i = A, j = B)$ and $(i = B, j = A)$, we obtain a contradictory equation $E^A + E^B < E^B + E^A$, which means that our assumption of the non-degenerate ground state for the same ground state electron density is wrong. Therefore, $\psi, v_{ext},$ and n_0 determine each other uniquely and the potential just differs by some constant at most. The HK theorem suggests that the ground state energy can be expressed as

$$E_0[n_0] = \int d\vec{r}\, n_0(\vec{r}) v_{ext} + F_{HK}[n_0] = \langle \psi[n_0] | \hat{H}_e | \psi[n_0] \rangle, \quad (2.5)$$

where $F_{HK}[n_0]$ is the universal functional of the ground state density which consists of the kinetic energy of the electron and the electron-electron interaction. The HK theorem makes the energy a functional of the ground state density.

HK Theorem II: The energy functional $E[n]$ in the presence of an external potential v_{ext} is minimized by the ground state electron density.

Proof: The HK second theorem explains the variational approach to define the ground state system. Consider a trial density $n(\vec{r})$ for an external potential v_{ext} such that $n(\vec{r}) \geq 0$ and $\int d\vec{r}\, n(\vec{r}) = N$ is satisfied. The energy evaluated using this trial density satisfy the condition

$$E[n(\vec{r})] = \int d\vec{r}\, n(\vec{r}) v_{ext} + F_{HK}[n] \geq E_0[n_0(\vec{r})], \quad (2.5)$$

where the equality sign holds if the trial density is the ground state density. Using the variational approach, we can minimize the energy functional in Eq. (2.5) as follows

$$\frac{\delta}{\delta n(\vec{r})}\{E[n] - \mu\big(\int d\vec{r}\, n(\vec{r}) - N\}\big|_{n(\vec{r})=n_0} = 0\,, \tag{2.6}$$

where, μ is the Lagrange multiplier. This proves the HK second theorem suggesting that the ground state density is the condition for the minimum energy functional.

The HK theorem shows that the ground state density of a condensed matter system in the presence of an external potential has one to one mapping to the ground state energy. But the energy functional is expressed in terms of the unknown functional F_{HK}. Kohn and Sham explained the methods to deal with this unknown functional which helped to make the HK theorem useful in practical computations.

2.1.2. Kohn-Sham Approach

The Kohn-Sham (KS) approach uses a single-particle orbital to map the non-interacting system to the real system with interacting electrons [6]. This method is analogous to the HF approximation. Similar to the HF approximation mentioned above, the KS approach is also a self-consistent procedure to derive a set of the KS orbitals from an effective one-electron potential [7]. Kohn and Sham considered a *fictitious* non-interacting system having the ground state density equal to the real interacting system. The Hamiltonian of such non-interacting system can be written simply as the sum of the individual energy operators *i.e.*

$$\hat{H}_s = \hat{T}_s + \hat{V}_s(\vec{r}) = -\frac{\hbar^2}{2m}\sum_i \nabla_i^2 + \int d\vec{r} V_s(\vec{r})\, \hat{n}(\vec{r}), \tag{2.7}$$

where, $\hat{V}_s(\vec{r})$ is the effective potential experienced by the non-interacting system. We can derive the general form of this effective potential using the KS approach. The

wavefunction ϕ_s satisfies $\hat{H}_s\Phi_s = E_s\Phi_s$ and it can be expressed as the Slater determinant of the individual atomic orbitals ϕ_i in the system, *i.e.*

$$\Phi_s = \frac{1}{\sqrt{N!}}\begin{vmatrix} \phi_1(\vec{r}_1) & \phi_2(\vec{r}_1) & \cdots & \phi_N(\vec{r}_1) \\ \phi_1(\vec{r}_2) & \phi_2(\vec{r}_2) & \cdots & \phi_N(\vec{r}_2) \\ \vdots & \vdots & \vdots & \vdots \\ \phi_1(\vec{r}_N) & \phi_2(\vec{r}_N) & \cdots & \phi_N(\vec{r}_N) \end{vmatrix}. \tag{2.8}$$

Hence, the many-body problem is reduced to a single particle equation analogous to the HF equation

$$\hat{h}_{KS}\phi_i = \varepsilon_i\phi_i\,. \tag{2.9}$$

where, $E_s = \sum_i \varepsilon_i$ is the energy of the KS system and $\hat{h}_{KS} = -\frac{\hbar^2}{2m}\nabla^2 + v_s(\vec{r})$ is the single electron KS operator. The potential v_s is chosen such that the non-interacting system density $n(\vec{r}) = \sum_i \phi_i(\vec{r})^*\phi_i(\vec{r}) = n_0(\vec{r})$ gives the ground state density of the real condensed matter system. The energy functional for the non-interacting system with electron density $n(\vec{r})$ with the potential v_s is

$$\begin{aligned} E_s[n] = \sum_i \varepsilon_i[n] &= -\frac{\hbar^2}{2m}\sum_i \langle\phi_i|\nabla^2|\phi_i\rangle + \int d\vec{r}\, n(\vec{r})v_s(\vec{r}) \\ &= T_s[n] + \int d\vec{r}\, n(\vec{r})v_s(\vec{r}). \end{aligned} \tag{2.10}$$

This is not exactly equal to the real energy and hence, Kohn and Sham defined the real energy of the interacting system as

$$\begin{aligned} E_0[n] &= \int d\vec{r}\, n(\vec{r})v_{ext}(\vec{r}) + F_{HK}[n] \\ &= \int d\vec{r}\, n(\vec{r})v_{ext}(\vec{r}) + T_s[n] + J[n] + E_{XC}[n], \end{aligned} \tag{2.11}$$

where, $J[n]$ is the classical Coulomb interaction and $E_{XC}[n]$ is the exchange-correlation energy functional. We see that the unknown functional is expressed in terms of the non-

interacting kinetic energy $T_s[n]$ which can be evaluated using the relation in Eq. (2.10). The Coulomb interaction can be easily expressed in terms of the electron density as

$$J[n] = \frac{1}{2}\int\int d\vec{r}_i d\vec{r}_j \frac{n(\vec{r}_i)n(\vec{r}_j)}{4\pi\epsilon_0 r_{ij}} . \tag{2.12}$$

The exchange-correlation energy remains still unknown as it contains the unknown functional which is the sum of the interacting electron kinetic energy ($T[n]$) and electron-electron correlation energy ($E_{ee}[n]$):

$$E_{XC}[n] = F_{HK}[n] - T_s[n] - J[n] = T[n] - T_s[n] + E_{ee}[n] - J[n]. \tag{2.13}$$

The exchange-correlation functional reflects all the quantum mechanical effects in the system. Equation (2.11) can be expanded in terms of the KS orbitals ϕ_i which is just a trial function and hence, a variational method is used in KS approach to find the best value for the KS orbitals which are closer to the exact KS orbitals. The exact KS orbitals determine the ground state energy of the real interacting system. Using the constraint of $\int d\vec{r} n(\vec{r}) = N$ to minimize the energy with the Lagrange's multiplier μ, using variational method, we obtain

$$\delta\{E[n] - \mu\big(\int d\vec{r} n(\vec{r}) - N\big)\} = 0 . \tag{2.14}$$

The HK theorem I states that the electron density is uniquely defined for a given external potential and so for the state $\phi + \delta\phi$, there should be a unique electron density $n + \delta n$. By definitions of the electron density $n = \sum_i \phi_i^* \phi_i$ and the orthonormality condition $\int d\vec{r} \phi_i^* \phi_i = 1$, by using the variations, we obtain

$$\delta n = \sum_i \delta\phi_i^* \phi_i + \phi_i^* \delta\phi_i,$$

$$0 = \int d\vec{r}\,\delta\phi_i^*\phi_i + \phi_i^*\delta\phi_i, \tag{2.15}$$

$\delta E[n]$ in Eq. (2.14) consists of $\delta T_s[n]$, $\delta J[n]$, $\delta E_{XC}[n]$, and $\delta\int d\vec{r}\; n(\vec{r})v_{ext}(\vec{r})$ term as followed from Eq. (2.11). The non-interacting kinetic energy can be easily expressed in terms of the ground state density as follows

$$\delta T_s[n] = -\frac{\hbar^2}{2m}\sum_i \int d\vec{r}\,\delta(\phi_i^*\nabla^2\phi_i) = -\frac{\hbar^2}{2m}\sum_i \int d\vec{r}(\delta\phi_i^*\nabla^2\phi_i + \phi_i^*\nabla^2\delta\phi_i\,. \tag{2.16}$$

We arrived at Eq. (2.16) using Eqs. (2.9) and (2.15). Similarly, we can write the external potential term of the non-interacting system and the Coulomb interaction also in terms of the electron density:

$$\delta J[n] = \int\int d\vec{r}_i d\vec{r}_j \frac{n(\vec{r}_j)}{4\pi\epsilon_0 r_{ij}}\delta n(\vec{r}_i),$$

$$\delta\int d\vec{r}\; n(\vec{r})v_{ext}(\vec{r}) = \int d\vec{r}\; v_{ext}(\vec{r})\delta n(\vec{r})\,. \tag{2.17}$$

The exchange correlation functional is unknown but we can use the functional derivative measures to write it as

$$E_{XC}[n+\delta n] = E_{XC}[n] + \int d\vec{r}\,\frac{\delta E_{XC}[n]}{\delta n}\delta n,$$

$$\delta E_{XC}[n] = \int d\vec{r}\,\frac{\delta E_{XC}[n]}{\delta n}\delta n\,, \tag{2.18}$$

Using Eqs. (2.15) to (2.18) in Eq. (2.14) and the chemical potential μ which is the sum of the occupied energy $\sum_i \varepsilon_i$, we obtain for the variation $\delta\phi_i^*$,

$$\sum_i \int d\vec{r}\;\delta\phi_i^*\left[-\frac{\hbar^2}{2m}\nabla^2 + v_{ext} + \int d\,\vec{r}_j\,\frac{n(\vec{r}_j)}{4\pi\epsilon_0 r_{ij}} + \frac{\delta E_{XC}[n]}{\delta n} - \varepsilon_i\right]\phi_i = 0.$$

Since $\delta\phi_i^*$ is arbitrary, we have

$$\sum_i \left[-\frac{\hbar^2}{2m}\nabla^2 + v_{ext} + \int d\,\vec{r}_j \frac{n(\vec{r}_j)}{4\pi\epsilon_0 r_{ij}} + \frac{\delta E_{XC}[n]}{\delta n}\right]\phi_i = \sum_i \varepsilon_i \phi_i,$$

$$\sum_i \left[-\frac{\hbar^2}{2m}\nabla^2 + v_{ext} + V_H + V_{XC}\right]\phi_i = \sum_i \varepsilon_i \phi_i,$$

$$\sum_i \left[-\frac{\hbar^2}{2m}\nabla^2 + V_{eff}\right]\phi_i = \sum_i \varepsilon_i \phi_i \ , \qquad (2.19)$$

The KS approach reduces the problem to N single-particle Schrödinger equations. So, the KS potential (v_s) defined for the non-interacting system compared to Eq. (2.9) shows that $v_s = V_{eff}$ is the sum of the external potential, the Hartree potential (V_H) and the exchange-correlation potential (V_{XC}). This potential is required to convert the interacting system into the non-interacting system which has the ground state electron density of the real system. Both the external potential and the Hartree potential are known and can be calculated easily. But the exchange-correlation potential is still unknown and hence, we need to use some approximations to this term.

Magnetic materials have spin-polarized electronic structure. So, we need to use a spin-dependent KS approach to solve the Schrödinger equation in magnetic systems. Up to now, we have ignored the spin-dependent terms. For FM and collinear AFM materials with the (sublattice) magnetization along a certain direction (for example, the *z* axis), we can define separately the spin-up ($n_\uparrow$) and spin-down ($n_\downarrow$) components of the electron density with spin up (down) pointing parallel (antiparallel) to the z axis. The magnetic moment associated with such system is given by $m_x = m_y = 0, m_z = \mu_B(n_\uparrow - n_\downarrow)$. The KS equations for each spin component can be decoupled, and we can solve them similar to Eq. (2.19) for the two spin components, *i.e.,* $H_\alpha \phi_{i,\alpha} = \varepsilon_{i,\alpha}\phi_{i,\alpha}$, where the Hamiltonian H_α is defined as

$$H_\alpha = -\frac{\hbar^2}{2m}\nabla^2 + v_{ext} + V_H + V_{XC,\alpha} + (-1)^s B_z, \tag{2.20}$$

where B_z is the magnetic field, $s = 0$ (1) for $\alpha = \uparrow (\downarrow)$.

In a noncollinear magnetic system, such as a noncollinear antiferromagnet, where the spin quantization axis changes from site-to-site spin is not a good quantum number. Therefore, in the noncollinear case, the Kohn-Sham eigenstate is a mixed state of spin up and spin down which is given by the spinor [8, 9]:

$$\phi_i = \begin{bmatrix} \phi_{i,\uparrow} \\ \phi_{i,\downarrow} \end{bmatrix}. \tag{2.21}$$

In this case, we can define a 2×2 Hermitian spin-density matrix

$$\underline{n}(\vec{r}) = \sum_i \phi_i \phi_i^+ = \sum_i \begin{bmatrix} |\phi_{i,\uparrow}|^2 & \phi_{i,\uparrow}\phi_{i,\downarrow}^* \\ \phi_{i,\downarrow}\phi_{i,\uparrow}^* & |\phi_{i,\downarrow}|^2 \end{bmatrix}. \tag{2.22}$$

The electron density has form $n(\vec{r}) = \sum_\alpha \sum_i \phi_{i,\alpha}^* \phi_{i,\alpha}$ and the magnetization density is $\vec{m}(\vec{r}) = \langle \phi_i | \sigma_x \hat{x} + \sigma_y \hat{y} + \sigma_z \hat{z} | \phi_i \rangle$, where σ_j are the Pauli matrices. Using these definitions, we can rewrite the spin density matrix as

$$\underline{n}(\vec{r}) = \frac{1}{2}\left(n(\vec{r})I + \vec{\sigma}.\vec{m}(\vec{r})\right) = \frac{1}{2}\begin{bmatrix} n(\vec{r}) + m_z(\vec{r}) & m_x(\vec{r}) - im_y(\vec{r}) \\ m_x(\vec{r}) + im_y(\vec{r}) & n(\vec{r}) - m_z(\vec{r}) \end{bmatrix}. \tag{2.23}$$

Unlike Eq. (2.20), the KS equations for spinors are

$$\sum_\beta H_{\alpha\beta}\phi_{i,\beta} = \varepsilon_i \phi_{i,\alpha}\ , \tag{2.24}$$

where the Hamiltonian $H_{\alpha\beta}$ is not diagonal but with an off-diagonal element

$$H_{\alpha\beta} = (T + v_{ext} + V_H)\delta_{\alpha\beta} + V_{XC,\alpha\beta}\ . \tag{2.25}$$

In the case of the collinear spins, the off-diagonal components resulting from the exchange-correlation potential $\left(\frac{\delta E_{XC}[\underline{n}(\vec{r})]}{\delta n_{\alpha\beta}}\right)$ vanishes because the density matrix is diagonal. For collinear spins, we have a decoupled spin up and spin down equation. But in the non-collinear case, the off-diagonal components in the Hamiltonian are not zero as in the density matrix. Using a unitary matrix $U(\vec{r})$, which is the spin 1/2 rotation matrix, the density matrix can be diagonalized. In the absence of spin-orbit coupling, the energy is invariant with respect to spin rotation. On the contrary, in the presence of the spin-orbit coupling, the energy depends on the spin orientation, and thus the spin rotation cannot be separated from the crystal symmetry. As a result, the noncollinear spin DFT is computationally more expensive.

2.1.3. Exchange-Correlation Functional

The HK theorem and the KS approach explain the method to implement DFT but do not provide a method to determine the exchange-correlation energy E_{XC}. The exact form of this functional would allow the exact solution of the many-body problem, which is extremely complicated. Therefore, approximations are used to represent the exchange-correlation energy. As a result, DFT calculations are not exact and depend upon the type of the approximation used.

The simplest form of DFT is the Thomas-Fermi (TF) approximation. The TF approximation assumes that an inhomogeneous system can be divided into a small volume of the homogeneous subsystem, where the kinetic energy density can be easily found. Within the TF approximation, the kinetic energy of the system can be expressed as follows [10]:

$$T[n] = \int d\vec{r} C_k n(\vec{r})^{\frac{4}{3}}, \tag{2.27}$$

Where, C_k is an adjustable constant.

The TF approximation does not include neither the exchange energy nor electron-electron correlation energy. One can approximate the exchange-correlation energy either by an empirical or non-empirical method. In the empirical method, the exchange-correlation functional is expressed in terms of some parameters which can be found by fitting the experimentally known results. Therefore, the empirical methods depend upon what quantity is used to fit these parameters and this type of methods is valid only for calculating that kind of quantities. On the contrary, in the non-empirical methods, the exchange-correlation functional is expressed in terms of the variables such as the electron density and its gradient. This kind of approximation is universal and can be used for a large group of systems compared to the non-empirical method. Some of the widely used approximations are a local density approximation (LDA), a generalized gradient approximation (GGA), hybrid methods, B3LYP (empirical method), *etc*.

Local density approximation (LDA) is analogous to the Thomas-Fermi approximation. In LDA, we assume that the system under consideration can be divided into smaller regions with a homogeneous electron gas distribution and electron density $n(\vec{r})$ and hence, we can define the exchange-correlation energy density (ε_{XC}^{hom}) for such regions. The total exchange-correlation energy in LDA is defined as [11, 12]

$$E_{XC}^{LDA}[n(\vec{r})] = \int d\vec{r}\ \varepsilon_{XC}^{hom}[n(\vec{r})]n(\vec{r}). \tag{2.28}$$

This exchange-correlation energy density can be split into the exchange energy density $\left(\varepsilon_X^{hom}\right)$ and correlation energy density (ε_C^{hom}). The exchange energy density for the uniform electron gas is given by [2, 3, 13]

$$\varepsilon_X^{hom}[n] = -\frac{3}{4}\left(\frac{3}{\pi}\right)^{\frac{1}{3}} n^{\frac{1}{3}} \ . \tag{2.29}$$

The correlation energy density for a uniform electron gas is not known exactly but can be found using quantum Monte-Carlo calculations for a homogeneous system [14– 17]. LDA does not contain any free parameters and hence, it belongs to a non-empirical method. LDA is a very simple approximation and hence, it is used extensively in the DFT calculations. LDA predicts fairly accurate bond lengths, lattice constants, phase stability, *etc*. However, LDA overestimates the atomization energy and underestimates the energy band gaps of semiconductors and insulators [18].

In magnetic systems, LDA can be extended to local spin density approximation by incorporating the spin-up $(n_\uparrow(\vec{r}))$ and spin-down $(n_\downarrow(\vec{r}))$ electron densities, so that the exchange-correlation energy is expressed as

$$E_{XC}^{LSDA}[n_\uparrow(\vec{r}), n_\downarrow(\vec{r})] = \int d\vec{r}\ \varepsilon_{XC}^{hom}[n_\uparrow(\vec{r}), n_\downarrow(\vec{r})]n(\vec{r}), \tag{2.30}$$

where the electron density is $n(\vec{r}) = n_\uparrow(\vec{r}) + n_\downarrow(\vec{r})$.

Another widely used DFT approach is generalized gradient approximation (GGA). Real condensed matter systems are not generally homogeneous. There are always some changes in the electron density at different regions. The inhomogeneity can be well defined by including a gradient of the electron density. The GGA is just the extension of

the LDA but with extra dependence on the gradient. The exchange-correlation functional can be defined as [19]

$$E_{XC}^{GGA}[n(\vec{r})] = \int d\vec{r}\ \varepsilon_{XC}^{hom}[n(\vec{r}), |\nabla n(\vec{r})|]n(\vec{r}). \quad (2.28)$$

In the case of the spin-polarized calculations, the GGA exchange-correlation functional can be expressed in terms of the spin-up and spin-down electron density and their gradients. Usually, the GGA more correctly predicts the atomic structure (bond lengths and lattice parameters) than LDA. Similar to LDA, GGA also underestimates the band gaps. The experimentally found ground states of magnetic systems (like Fe (bcc), Ni (fcc), Cr (bcc), *etc*.) are well predicted by both GGA and LDA. In some cases, however, GGA provides a more realistic description. In this work, we studied the magnetic systems using GGA approximation within the Perdew-Burke-Ernzerhof (PBE) approach [19].

Although GGA is an improvement over LDA, both approximations have deficiencies. In particular, they are not able to describe weak van der Waals interactions. Also, electronic structures of the systems with strongly localized d and f electrons are not well described by LDA and GGA. In such cases, LDA+U methods with empirical parameters U and J are more appropriate [20, 21]. There are also other functionals like hybrid functionals (*e.g.,* B3LYP, HSE06) which use a combination of the exchange-correlation energy obtained from the Hartree-Fock and DFT methods through some fitting parameters [2,3].

2.2. Wannier Function

In the condensed matter systems, we generally deal with the crystalline solids which has a periodic crystal potential ($V(\vec{r}) = V(\vec{r} + \vec{R})$), where $\vec{R}$ is the crystal lattice vector. According to the Bloch theorem, the solution of the Kohn-Sham equations for such systems can be written in terms of the function [3]

$$\psi_{n,\vec{k}}(\vec{r}) = e^{i\,\vec{k}.\vec{r}} u_{n,\vec{k}}(\vec{r})\,, \tag{2.29}$$

where n is the band index, $\vec{k}$ is the quasi-momentum in a Brillouin zone, $e^{i\,\vec{k}\cdot\vec{r}}$ is the envelope function, and $u_{n,\vec{k}}(\vec{r})$ is the periodic Bloch function ($u_{n,\vec{k}}(\vec{r} + \vec{R}) = u_{n,\vec{k}}(\vec{r})$). Eq. (2.29) implies that the Bloch wavefunction $\psi_{n,\vec{k}}(\vec{r})$ is periodic in the reciprocal space ($\psi_{n,\vec{k}+\vec{G}}(\vec{r}) = \psi_{n,\vec{k}}(\vec{r})$), where $\vec{G}$ is the reciprocal lattice vector. The isolated bands would be better explained using the atomic functions instead of the Bloch functions. But the atomic functions lack the orthogonality. Wannier proposed to use orthogonal functions constructed from the Bloch functions – now known as Wannier functions (WFs) [22]. The WFs can be constructed by the superposition of the Bloch functions across the Brillouin zone (BZ) as

$$w_{n,0}(\vec{r}) = \frac{V}{(2\pi)^3}\int_{BZ} d\vec{k}\,\psi_{n,\vec{k}}(\vec{r})\,, \tag{2.30}$$

where V is the volume of the unit cell, the integral is carried over the BZ. The real-space WFs has translational invariance and hence, more WFs can be constructed by inserting a phase factor $e^{-i\,\vec{k}\cdot\vec{R}}$. In the Dirac bra-ket representation, the WF in a cell $\vec{R}$ associated with the band index n is given by

$$|n\,\vec{R}\,\rangle = \frac{V}{(2\pi)^3}\int_{BZ} d\vec{k}\; e^{-i\,\vec{k}\cdot\,\vec{R}}\left|\psi_{n,\vec{k}}\right\rangle\,. \tag{2.31}$$

This represents a Fourier transform of the Bloch wavefunction and hence, its inverse transform is

$$\left|\psi_{n,\vec{k}}\right\rangle = \sum_{\vec{R}} e^{i\,\vec{k}.\vec{R}}\left|n\,\vec{R}\right\rangle. \tag{2.32}$$

The Bloch wavefunctions can be constructed by a linear superposition of the WFs with the corresponding phase factor. Equation (2.31) shows that the WFs are real space functions centred near $\vec{R}$ and decay rapidly with increasing $|\vec{r}-\vec{R}|$. WFs are localized like atomic wavefunctions, but they are also orthonormal, $\langle n\,\vec{R}|m\,\vec{R}'\rangle = \delta_{nm}\delta_{\vec{R}\,\vec{R}'}$ as follows from

$$\langle n\,\vec{R}|m\,\vec{R}'\rangle = \left(\frac{V}{(2\pi)^3}\right)^2 \int d\vec{r}\;\int_{BZ} d\vec{k}\int_{BZ} d\vec{k}'\,\langle\psi_{n,\vec{k}}|\psi_{m,\vec{k}'}\rangle e^{-i\,\vec{k}.\vec{R}-i\vec{k}'.\vec{R}'}$$

$$= \frac{V}{(2\pi)^3}\int_{BZ} d\vec{k}\int_{BZ} d\vec{k}'\;\delta_{nm}\delta\left(\vec{k}-\vec{k}'\right)e^{-i\,\vec{k}.\vec{R}-i\vec{k}'.\vec{R}'} = \delta_{nm}\delta_{\vec{R}\,\vec{R}'}\,. \tag{2.33}$$

The Bloch wavefunctions can differ by the overall phase. A gauge transformation of the Bloch wavefunction gives a Bloch wavefunction which has the same physical meaning as the original one because the electron density remains unchanged. In this regard, the Bloch wavefunction can be considered as unique. For the real gauge function $\theta(\vec{k})$, which is periodic in the reciprocal space, the gauge transformation of the Bloch wavefunction has form

$$\left|\tilde{\psi}_{n,\vec{k}}\right\rangle = e^{i\theta_n(\vec{k})}\left|\psi_{n,\vec{k}}\right\rangle. \tag{2.34}$$

This gauge transformation changes the shape and spread of the WF [23]. The WF for the band n under the gauge transformation given by Eq. (2.34) can be expressed as

$$\left|\widetilde{n\,\vec{R}}\right\rangle = \frac{V}{(2\pi)^3}\int_{BZ} d\vec{k}\, e^{i\theta_n(\vec{k})} e^{-i\,\vec{k}.\vec{R}} \left|\psi_{n,\vec{k}}\right\rangle \,. \tag{2.35}$$

If some bands remain degenerate and cross at some points in the BZ, the gauge transformation can be defined by the unitary transformation ($U_{mn}^{\vec{k}}$) of the set of these bands $\{n\}$ as

$$\left|\tilde{\psi}_{n,\vec{k}}\right\rangle = \sum_{\{n\}} U_{mn}^{\vec{k}} \left|\psi_{m,\vec{k}}\right\rangle . \tag{2.36}$$

The corresponding WF constructed from this gauge transformed Bloch wavefunction is

$$\left|\widetilde{n\,\vec{R}}\right\rangle = \frac{V}{(2\pi)^3}\int_{BZ} d\vec{k}\, e^{-i\,\vec{k}.\vec{R}} \sum_{\{n\}} U_{mn}^{\vec{k}} \left|\psi_{m,\vec{k}}\right\rangle \,. \tag{2.37}$$

The smoothness of these unitary transformation determines whether the WF are maximally localized or not. The criterion for the maximally localized WF can be described by calculating the spread Ω of the WF as

$$\Omega = \sum_{n} [\langle 0\; n|r^2|0\; n\rangle - \langle 0\; n|\vec{r}|0\; n\rangle^2] \,. \tag{2.38}$$

A set of the Bloch wavefunctions is selected in such a way that the unitary transformation chosen will minimize the spread of the WF. Nicola Marzari and David Vanderbilt proposed the steepest descent algorithm to find the maximally localized WF [23]. In this approach, initially orthonormal Bloch wavefunctions are defined in terms of the smooth trial functions through projection. The periodic wavefunctions at each quasi-momenta for each band can be extracted and their overlap can be calculated using equation (2.38) and

minimized. Using the band structure obtained from DFT, k-point mesh, and unit cell volume, we can build the Hamiltonian matrix written within a basis of the obtained localized WF. Using this tight-binding Hamiltonian, we can then calculate the Berry curvature, anomalous Hall conductivity, spin Hall conductivity, and other properties [24, 25].

2.3. Berry Curvature

Consider a parametric space defined by $\vec{R} = (R_1, R_2, \dots \dots)$ where the set of parameters is implicitly included in the Schrödinger equation

$$H(\vec{R})|\psi_n\rangle = E_n(\vec{R})|\psi_n\rangle . \tag{2.39}$$

This parametric space may evolve in time so that $\vec{R}(t) = (R_1(t), R_2(t), \dots \dots)$ and hence, the Hamiltonian depends on time through these parameters. Consider a system slowly moving along a path Γ_c in the parameter space from $\vec{R}(t = 0)$ to $\vec{R}(t = t_f)$, we can find the corresponding state by solving the time-dependent Schrödinger equation

$$i\hbar \frac{\partial|\psi_n(t)\rangle}{\partial t} = H\left(\vec{R}(t)\right)|\psi_n(t)\rangle . \tag{2.40}$$

According to the quantum adiabatic theorem, the instantaneous eigenstate of the Hamiltonian remains still in the initial eigenstate. Hence, due to the gauge freedom, the eigenstate can be expressed as $e^{i\xi_n(t)}|\psi_n(t)\rangle$ with the time dependent phase $\xi_n(t)$. Equation (2.40) has the following solution

$$-\hbar \frac{\partial \xi_n(t)}{\partial t}\ |\psi_n(t)\rangle + i\hbar \frac{\partial|\psi_n(t)\rangle}{\partial t} = E_n\left(\vec{R}(t)\right)|\psi_n(t)\rangle . \tag{2.41}$$

Multiplying by $\langle\psi_n(t)|$ and integrating over time, the phase factor for this eigenstate can be obtained as

$$\xi_n(t) = i\int dt\langle\psi_n(t)|\frac{\partial}{\partial t}|\psi_n(t)\rangle - \frac{1}{\hbar}\int_0^t dt'\, E_n\left(\vec{R}(t')\right). \tag{2.42}$$

There are two contributions to the phase. The second term is the usual dynamical phase factor seen in quantum-mechanics books. While the first term, as further analysis shows, determines the geometric phase that is independent of time and only depends on the path Γ_c followed during the evolution in the parametric space:

$$\gamma_n(\Gamma_c) = i\int dt\frac{d\vec{R}}{dt}\ \langle\psi_n|\nabla_{\vec{R}}|\psi_n\rangle = i\int_{\Gamma_c} d\vec{R}\cdot\langle\psi_n|\nabla_{\vec{R}}|\psi_n\rangle. \tag{2.43}$$

This geometric phase gained during the adiabatic evolution is known as the Berry phase and the integrand is known as the Berry connection (analogous to the vector potential) defined by $\vec{A}_n(\vec{R}) = i\langle\psi_n|\nabla_{\vec{R}}|\psi_n\rangle$ for the n^{th} band.

Let us consider a gauge transformation $\widetilde{|\psi_n\rangle} = e^{-i\beta(\vec{R})}|\psi_n\rangle$ so that the transformed Berry connection is

$$\widetilde{\vec{A}_n(\vec{R})} = \vec{A}_n(\vec{R}) + \nabla_{\vec{R}}\beta(\vec{R}). \tag{2.44}$$

This shows that the Berry connection is gauge dependent. The corresponding Berry phase under this gauge transformation is

$$\widetilde{\gamma_n(\Gamma_c)} = \int_{\Gamma_c} d\vec{R}\cdot\widetilde{\vec{A}_n(\vec{R})} = \gamma_n(\Gamma_c) + \beta(\vec{R}_f) - \beta(\vec{R}_i). \tag{2.45}$$

The Berry phase is not gauge invariant as we traversed from the initial position $\vec{R}_i$ to the final position $\vec{R}_f$ in the parametric space. The gauge invariant Berry phases cannot be

observed in real life according to quantum mechanics. But, if we considered a closed path in the parametric space, $\beta(\vec{R}_f) - \beta(\vec{R}_i) = 2\pi \times integer$, the Berry phase becomes gauge invariant and hence, a meaningful physical quantity. In the 3D space, we can define this closed boundary Γ_c on the surface S and the corresponding Berry phase as

$$\gamma_n(\Gamma_c) = \oint_{\Gamma_c} d\vec{R} \cdot \vec{A}_n(\vec{R}) = \iint d\vec{S} \cdot \nabla \times \vec{A}_n(\vec{R}) \ , \tag{2.46}$$

The integrand in the surface integral is analogous to the magnetic field and the whole integral is analogous to the magnetic flux coming out of the surface S [26, 27]. The integrand term is well known as the Berry curvature $\vec{\Omega}_n(\vec{R}) = \nabla \times \vec{A}_n(\vec{R})$. The curl of the Berry connection shows that the Berry curvature is gauge invariant, *i.e.*, $\nabla \times \nabla\beta = 0$. The Berry curvature can be written as

$$\vec{\Omega}_n(\vec{R}) = \nabla_{\vec{R}} \times \vec{A}_n(\vec{R}) = \ i\langle \nabla_{\vec{R}} \psi_n | \times | \nabla_{\vec{R}} \psi_n \rangle,$$

$$\vec{\Omega}_n(\vec{R}) = i\langle \nabla_{\vec{R}} \psi_n | \sum_m |\psi_m\rangle\langle\psi_m| \times |\nabla_{\vec{R}} \psi_n\rangle$$

$$= \sum_{m \neq n} i\langle \nabla_{\vec{R}} \psi_n | \psi_m \rangle \times \langle \psi_m | \nabla_{\vec{R}} \psi_n \rangle \ . \tag{2.47}$$

Here, we used the completeness relation $\hat{1}=\sum_m |\psi_m\rangle\langle\psi_m|$ and the fact that $m = n$ term vanishes. Using the Equation (2.39) and taking the inner product with ket $\langle\psi_m|$, we can rewrite Equation (2.47) as

$$\vec{\Omega}_n(\vec{R}) = i \sum_{m \neq n} \frac{\langle \psi_m | \nabla_{\vec{R}} H | \psi_n \rangle \times \langle \psi_m | \nabla_{\vec{R}} H | \psi_n \rangle}{(E_n - E_m)^2} \ . \tag{2.48}$$

This equation shows that the sum of the Berry curvatures of all the eigenstates for a given Hamiltonian vanishes and the Berry curvature is usually large at avoided crossing regions.

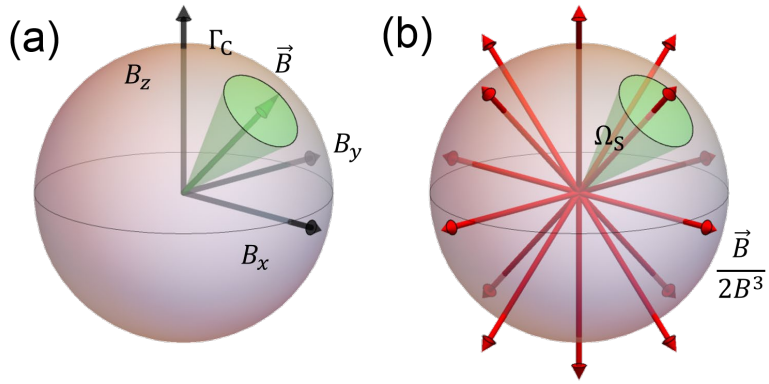

Figure 2.1. The parametric space for the spin 1/2 system in the presence of magnetic field is defined by the Bloch sphere. (a) Magnetic field $\vec{B}$ denoted by the green arrow traces the path Γ_c in the parametric space (B_x, B_y, B_z). (b) The Berry curvature field is acting like a field due to monopole at the origin (point of degeneracy). The surface S enclosed by the boundary Γ_C makes a solid angle Ω_S. The number of lines of the Berry curvature field traversing through the green conic section determines the Berry phase and hence, the corresponding geometric phase obtained on traversing this closed path is $\frac{1}{2}\Omega_S$.

To further understand the Berry curvature and the Berry phase, let us consider an example of the spin 1/2 system in the presence of a magnetic field in the parameter space $(B_x, B_y, B_z) \rightarrow (\theta, \phi)$ of the Bloch sphere as shown in Fig. 2.1. The Hamiltonian is given by H=$\vec{B} \cdot \vec{\sigma}$ where $\vec{\sigma}$ is the Pauli matrices and $\vec{B} = B(sin\theta cos\phi, sin\theta sin\phi, cos\theta)$ as

shown in Figure 2.1(a) by the green arrow. The eigenstate obtained for this Hamiltonian is $E_{\pm} = \pm B$ and corresponding eigenfunctions are

$$|+\rangle = \begin{bmatrix} \cos\frac{\theta}{2} & e^{-i\phi} \\ \sin\frac{\theta}{2} & \end{bmatrix}, \qquad |-\rangle = \begin{bmatrix} \sin\frac{\theta}{2} & e^{-i\phi} \\ \cos\frac{\theta}{2} & \end{bmatrix}. \tag{2.49}$$

The Berry connection in the parametric space (θ, ϕ) for the n[th] band is $\vec{A}_n(\theta,\phi) = (A_n(\theta), A_n(\phi))$ where $A_n(\theta) = i < \left\langle n\left|\frac{1}{B}\partial_\theta\right|n\right\rangle$ and $A_n(\phi) = i < \left\langle n\left|\frac{1}{Bsin\theta}\partial_\phi\right|n\right\rangle$ are the corresponding components in the spherical coordinates. For the lower band $|-\rangle$, the Berry connection is found to be $\vec{A}_{|-\rangle}(\theta,\phi) = (0, \frac{1}{2B}\tan\frac{\theta}{2})$ and the corresponding Berry curvature in the spherical coordinates is $\vec{\Omega} = \nabla \times \vec{A}_{|-\rangle}(\theta,\phi) = \frac{1}{2B}\tan\frac{\theta}{2}\,\hat{B} = \frac{\vec{B}}{2B^3}$. The Berry curvature is pointing radially outward as shown in Figure 2.1(b). The high energy state also has the same Berry connection and Berry curvature but opposite in sign. The sum of the total berry curvature due to the total band is zero.

The corresponding Berry connection and Berry curvature are analogous to the vector potential and the magnetic field generated by the magnetic monopole at the origin $(B = 0)$ where the two energy levels are degenerate. The region of the degeneracy points acts as a source and drain of the Berry curvature flux. Consider a magnetic field $\vec{B}$ tracing around the Bloch sphere an enclosed surface S with boundary path Γ_c as shown in Figure 2.1 (a). Then, we have

$$\gamma_n = \iint d\vec{S} \cdot \frac{\vec{B}}{2B^3} = \frac{1}{2}\,\Omega_S\,. \tag{2.50}$$

Equation (2.50) explains that the Berry phase gained on moving across the closed boundary Γ_c enclosing the surface S is half of the solid angle Ω_S subtended by this surface as shown by the green conic section in Figure 2.1(b). If the enclosed surface is a half of the sphere ($\theta = 0$ to $\frac{\pi}{2}$), $\gamma_n = \pi$ and the Berry phase for the whole surface of the sphere ($\theta = 0$ to $\frac{\pi}{2}$) is 2π.

In condensed matter systems, the periodic potential in the crystal provides the momentum space which acts like the parameter space. On integrating over the closed loop in the BZ, we gain the Berry phase due to the Bloch Hamiltonian providing the torus like topology. The modern theory of polarization is developed in terms of the Berry phase. Similarly, the Berry curvature explains the intrinsic anomalous Hall conductivity, the spin Berry curvature determines the intrinsic spin Hall conductivity [26, 27, 28]. The variations of the magnetic moment in the real space forming a noncoplanar configuration provide the parametric space in which the traversing electron gains the Berry phase. This phenomenon gives rise to the topological Hall effect [29].

The Bloch Hamiltonian in the presence of the adiabatic perturbation can be written to first order as [30]

$$|\widetilde{u_n}\rangle = |u_n\rangle - i\,\hbar \sum_{m \neq n} \frac{|u_m\rangle \left\langle u_m \middle| \frac{\partial u_n}{\partial t} \right\rangle}{E_n - E_m} \quad . \tag{2.51}$$

The velocity operator is given by

$$\vec{v}_n(\vec{k}) = \frac{1}{\hbar} \langle \widetilde{u_n} | \nabla_{\vec{k}} H | \widetilde{u_n} \rangle$$

$$= \frac{1}{\hbar}\langle u_n|\nabla_{\vec{k}}H|u_n\rangle - i\sum_{m\neq n}\left\{\frac{\langle u_n|\nabla_{\vec{k}}H|u_m\rangle\left\langle u_m\middle|\frac{\partial u_n}{\partial t}\right\rangle}{E_n - E_m} + cc\right\}$$

$$= \frac{1}{\hbar}\langle u_n|\nabla_{\vec{k}}H|u_n\rangle$$

$$- i\sum_{m\neq n}\left\{\frac{\langle u_n|\nabla_{\vec{k}}H|u_m\rangle\langle u_m|\nabla_{\vec{k}}u_n\rangle}{E_n - E_m}\,\dot{\vec{k}} + cc\right\},$$

$$\vec{v}_n(\vec{k}) = \frac{1}{\hbar}\frac{\partial E_n(\vec{k})}{\partial \vec{k}} - \dot{\vec{k}} \times \vec{\Omega}(\vec{k})\,. \tag{2.52}$$

Equation (2.52) has an extra term compared to the regularly used velocity term in the Bloch bands. This kind of anomalous velocity appears in some magnetic systems. The anomalous velocity term depends upon the Berry curvature. Eq. (2.52) can be used to analyze the symmetry relationship of the Berry curvature. For example, under the operation of the time reversal symmetry ($\hat{T}$), Eq. (2.52) is valid if $\hat{T}\,\vec{\Omega}(\vec{k}) = -\vec{\Omega}(-\vec{k})$ and under the operation of the inversion symmetry operator ($\hat{P}$), the Berry curvature relation is $\hat{P}\,\vec{\Omega}(\vec{k}) = \vec{\Omega}(-\vec{k})$. The sum of the Berry curvature over the BZ in the presence of the time reversal symmetry vanishes and hence, the absence of the time reversal symmetry leads to a finite anomalous velocity. Magnetic materials break the time reversal symmetry. The presence of the finite Berry curvature changes the transport properties of the magnetic materials.

2.4. Landau-Lifshitz-Gilbert-Slonczewski Equation

The transport properties of the magnetic materials are determined by the dynamics of the magnetization. Consider a free electron with spin angular momentum $\vec{S}$, in the presence of the magnetic field. The spin dynamics is described by the following equation

$$\frac{d\langle\vec{S}(t)\rangle}{dt} = -\frac{g\mu_B}{\hbar}\langle\vec{S}(t)\rangle \times \vec{H}\,(t). \tag{2.53}$$

For a volume of the electron gas, we can define the magnetic moment $\vec{m} = \frac{\vec{M}}{V}$ where the magnetization is $\vec{M} = \frac{g\mu_B}{\hbar}\langle\vec{S}(t)\rangle = \gamma\langle\vec{S}(t)\rangle$. Equation (2.53) in terms of the magnetic moment determines the magnetization dynamics

$$\frac{d\vec{m}}{dt} = -\gamma\,\vec{m} \times \vec{H}(t)\,. \tag{2.54}$$

This equation only describes the precession motion of the magnetic moment around the magnetic field. In practice, however, the magnetic moment dissipates which can be described by an additional damping term in Equation (2.54):

$$\frac{d\vec{m}}{dt} = -\gamma\,\vec{m} \times \vec{H}(t) + \alpha\,\vec{m} \times \frac{d\vec{m}}{dt}\,. \tag{2.55}$$

Eq. (2.55) is known as the Landau-Lifshitz-Gilbert (LLG) equation [31] where, α is the damping constant.

Eq. (2.55) can be generalized to describe the magnetization dynamics of the system with multiple magnetic sublattices with magnetic moments $\vec{m}_i$ on the i^{th} site. The magnetic field felt by the i^{th} lattice site is $\vec{H}_i = -\frac{1}{\mu}\frac{\partial H}{\partial\,\vec{m}_i}$. The spin Hamiltonian of such a system can be represented as follows

$$H = \sum_{i \neq j} J_{ij}\,\vec{m}_i.\vec{m}_j + H_K + H_Z + H_{DMI}\,, \tag{2.56}$$

where the first term is the Heisenberg exchange coupling between the neighbouring atoms, H_K is the magnetic anisotropy Hamiltonian which depends upon symmetry of the magnetic crystal, H_Z is the Zeeman term due to the external magnetic field, and H_{DMI} is

the Dzyaloshinskii-Moriya interaction (DMI) which ensures the non-coplanarity in the magnetic system. The exchange term makes the magnetic moments to align either parallel or antiparallel resulting in the FM or AFM phases. The terms in the spin Hamiltonian can be extracted from the DFT calculations using the energy mapping method [32].

The internal field cannot switch the magnetic moment. Therefore, we need an external source to overcome the energy barrier provided by the anisotropy term to switch the magnetic moment. The application of the spin-polarized electric current in a system with noncollinear magnetic moments leads to the spin transfer torque, as was discussed in the introduction. The effect of the spin transfer torque on the magnetization dynamics can be described by adding a new term in the LLG equation [33, 34]

$$\frac{d\vec{m}_i}{dt} = -\gamma\, \vec{m}_i \times \vec{H}_i + \alpha\, \vec{m}_i \times \frac{d\vec{m}_i}{dt} + \frac{\gamma}{\mu_0 M_s}\left[a[I_s]\, \vec{m}_i \times \vec{m}_i \times \vec{I}_S + b[I_s]\vec{m}_i \times \vec{I}_S\right], \quad (2.57)$$

where μ_0 is the magnetic permeability, M_s is the saturation magnetization, and $\vec{I}_S$ is the spin polarized current which exerts the spin transfer torque on the magnetic moment. $a[I_s]$ and $b[I_s]$ are the current dependent functions for the longitudinal and transverse torque, respectively. The spin current produces dual effect of the precession and switching. This equation is known as the Landau-Lifshitz-Gilbert-Slonczewski (LLGS) equation. It can be applied to describe the magnetization dynamics driven by the spin transfer torque on different magnetic sublattices [35].

References

[1] I. Levine, Quantum chemistry. *Prentice-Hall of India Pvt. Ltd.* **6** (2010).

[2] R. M. Dreizler and E. Engel, Density functional theory. *Springer* (2011).

[3] R. M. Martin, Electronic structure: basic theory and practical methods. *Cambridge University Press* (1999).

[4] P. Hohenberg and W. Kohn, Inhomogeneous electron gas. *Phys. Rev.* **136**, B864 (1964).

[5] W. Kohn and L. J. Sham, Self-consistent equations including exchange and correlation effects. *Phys. Rev.* **140**, A1133 (1965).

[6] K. Capelle, A bird's-eye view of density functional theory. *Braz. J. Phys.* **36**, 1318 (2006).

[7] W. Kohn, Nobel Lecture: Electronic structure of matter-wave functions and density functionals. *Rev. Mod. Phys.* **71**, 1253 (1999).

[8] J. Kubler, K. -H. Hock, and J. Sticht, Local spin-density functional theory of noncollinear magnetism (invited). *J. Appl. Phys.* **63**, 3482 (1988).

[9] J. Kubler, K. -H. Hock, J. Sticht and A. R. Williams, Density functional theory of noncollinear magnetism (invited). *J. Phys.F: Met. Phys.* **18**, 469 (1988).

[10] E. H. Lieb, Thomas-Fermi and related theories of atoms and molecules. *Rev. Mod. Phys.* **53**, 603 (1981).

[11] W. Kohn and L. J. Sham, Self-consistent equations including exchange and correlation effects. *Phys. Rev.* **140**, A1133 (1965)

[12] R. O. Jones and O. Gunnarsson, The density functional formalism, its applications and prospects. *Rev. Mod. Phys.* **61**, 689 (1989).

[13] R. G. Parr and W. Yang, Density-functional theory of atoms and molecules. *Oxford University Press* (1989).

[14] D. M. Ceperley and B. J. Alder, Ground state of the electron gas by a stochastic method. *Phys. Rev. Lett.* **45**, 566 (1980).

[15] S. H. Vosko, L. Wilk, and M. Nusair, Accurate spin-dependent electron liquid correlation energies for local spin density calculations: a critical analysis. *Can. J. Phys.* **58**, 1200 (1980).

[16] J. P. Perdew and A. Zunger, Self-interaction correction to density-functional approximations for many-electron systems. *Phys. Rev. B* **23**, 5048 (1981).

[17] J. P. Perdew and Y. Wang, Accurate and simple analytic representation of the electron-gas correlation energy. *Phys. Rev. B* **45**, 13244 (1992).

[18] J. P. Perdew and M. Levy, Physical content of the exact Kohn-Sham Orbital energies: Band gaps and derivative discontinuities. *Phys. Rev. Lett.* **51**, 1884 (1983).

[19] J. P. Perdew, K. Burke, M. Ernzerhof, Generalized gradient approximation made simple. *Phys. Rev. Lett.* **77**, 3865 (1996).

[20] A. I. Licechtenstein, V. I. Anisimov, and J. Zaanen, Density-functional theory and strong interactions: Orbital ordering in Mott-Hubbard insulators. *Phys. Rev. B* **52**, R5467(R) (1995).

[21] S. L. Dudarev, G. A. Botton, S. Y. Savrasov, C. J. Humphreys, and A. P. Sutton, Electron-energy-loss spectra and the structural stability of nickel oxide: An LSDA+U study. *Phys. Rev. B* **57**, 1505 (1998).

[22] G. H. Wannier, The structure of electronic excitation levels in insulating crystals. *Phys. Rev.* **52**, 191 (1937).

[23] N. Marzari, A. A. Mostofi, J. R. yates, I. Souza, and D. Vanderbilt, Maximally localized Wannier functions: Theory and applications. *Rev. Mod. Phys.* **84**, 1419 (2012).

[24] A. A. Mostofi, J. R. yates, Y. -S. Lee, I. Souza, D. Vanderbilt, and N. Marzari, Wannier90: A tool for obtaining maximally localised Wannier functions. *Comp. Phys. Commun.* **178**, 685 (2007).

[25] X. Wang, J. R. yates, I. Souza, and D. Vanderbilt, *Ab initio* calculation of the anomalous Hall conductivity by Wannier interpolation. *Phys. Rev. B* **74**, 195118 (2006).

[26] M.-C. Chang and Q. Niu, Berry curvature, orbital moment, and effective quantum theory of electrons in electromagnetic fields. *J. Phys.*: *Condens. Matt.* **20**, 193202 (2008).

[27] D. Xiao, M.-C. Chang, and Q. Niu, Berry phase effects on electronic properties. *Rev. Mod. Phys.* **82**, 1959 (2010).

[28] M. Gradhand, D. V. Fedorov, F. Pientka, P. Zahn, I. Mertig, and B. L. Gyorffy, First-principle calculations of the Berry curvature of Bloch states for charge and spin transport of electrons. *J. Phys.: Condens. Matter* **24**, 213202 (2012).

[29] A. Neubauer, C. Pfleiderer, B. Binz, A. Rosch, R. Ritz, P. G. Niklowitz, and P. Böni, Topological Hall effect in the A phase of MnSi. *Phys. Rev. Lett.* **102**, 186602 (2013).

[30] D. J. Griffiths and D. F. Schroeter, Introduction to quantum mechanics. *Cambridge Univ. Press.* (2018).

[31] T. L. Gilbert, A phenomenological theory of damping in ferromagnetic materials. *IEEE Trans. Magn.* **40**, 3443 (2004).

[32] H. J. Xiang, E. J. Kan, S. H. Wei, M.-H. Whagngbo, and X. G. Gong, Predicting the spin-lattice order of frustrated systems from first principles. *Phys. Rev. B* **84**, 224429 (2011).

[33] J. C. Slonczewski, Current-driven excitation of magnetic multilayers. *J. Magn. Magn. Mater.* **159**, L1 (1996).

[34] D. C. Ralph and M. D. Stiles, Spin transfer torques. *J. Magn. Magn. Mater.* **320**, 1190 (2008).

[35] H. V. Gomonay and V. M. Loktev, Spin transfer and current-induced switching in antiferromagnets. *Phys. Rev. B* **81**, 144427 (2010).

Chapter 3 Symmetry Dependent Anomalous Hall Conductivity

It is known that the anomalous Hall effect (AHE) emerges in metals with broken time-reversal symmetry (TRS) and strong spin-orbit coupling (SOC) [1]. Usually, the AHE is found in ferromagnetic (FM) metals, where a transverse voltage generated by a longitudinal charge current is sensitive to the net magnetization. The intrinsic AHE is driven by a fictitious magnetic field in the momentum space associated with the Berry curvature, a quantity inherent in the electronic band structure [2]. With the magnitude and direction determined by the magnetization and SOC, this fictitious magnetic field controls the charge current in a similar way as a real magnetic field in the ordinary Hall effect. The AHE vanishes in conventional collinear antiferromagnetic (AFM) metals due to the anomalous Hall conductivities being opposite in sign and hence cancelling each other for the two ferromagnetic sublattices with opposite magnetization. In other words, the existence of symmetry combining time reversal and lattice translation prohibits the AHE. This observation suggested that the presence of a non-vanishing net magnetic moment is the necessary condition to break the related symmetry and produce the AHE [3].

It appeared, however, that the AHE can be observed in certain types of non-collinear antiferromagnets, such as Mn_3X alloys (X = Ga, Ge, Ir, etc.) [4– 8]. In these metals, the Mn moments are arranged in a Kagome-type lattice within the (111) plane. The magnetic space group symmetry operations in these compounds cannot eliminate the total Berry curvature, leading to a non-vanishing AHE [4]. The presence of a sizable AHE in non-collinear AFM metals is interesting for AFM spintronics, where an AFM order parameter (Néel vector) can be used as a state variable and can be controlled on a

much shorter time scale compared to magnetization in ferromagnets as discussed in Section 1.1 [9– 11].

Importantly, specifics of magnetic ordering in non-collinear AFM materials associated with different magnetic space group symmetries have a strong impact on the AHE [12, 13]. For example, it was found that the AHC tensors have a different form in Mn_3X (X = Ga, Ge, and Sn) and Mn_3Y (Y = Rh, Ir, and Pt) compounds, due to different magnetic moment configurations. One can expect therefore that a significant change in the anomalous Hall conductivity (AHC) can emerge at the magnetic phase transition associated with switching between different non-collinear magnetic orderings. Realizing such an effect in practice would be interesting for potential spintronic applications, and therefore exploring the AHE in possible material systems with competing and tuneable non-collinear magnetic phases is valuable.

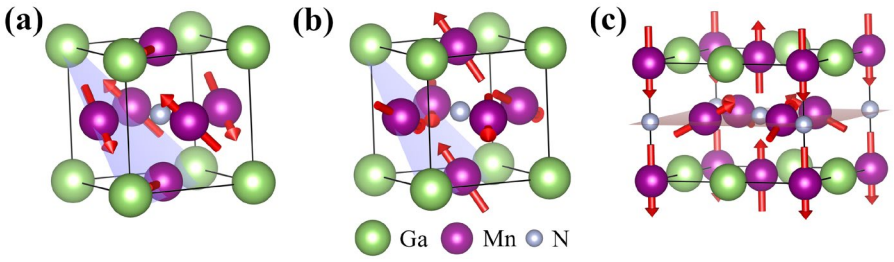

Figure 3.1. Different non-collinear magnetic phases in AFM antiperovskite $GaNMn_3$. (a) Γ_{5g}, (b) Γ_{4g}, and (c) M-1. Red arrows denote magnetic moments.

As discussed in Chapter 1 (Section 1.4), antiperovskite [Fig. 3.1] materials are potential candidates for the control of the AHE by tuneable non-collinear magnetism. Manganese nitride antiperovskites $ANMn_3$ (A = Ga, Cu, Ni, etc.) are typically metallic and often reveal complex magnetic orderings [14, 15, 16]. Various magnetic phases,

such as non-collinear AFM Γ_{5g} and Γ_{4g} phases and a non-collinear ferrimagnetic M-1 phase have been found in these compounds [Fig. 3.1]. Transformations between these magnetic phases can be induced by perturbations, such as doping, pressure, and temperature [16– 18]. It has also been predicted that the transition between the Γ_{5g} and Γ_{4g} phases can be achieved using a spin transfer torque [19]. These properties make $ANMn_3$ compounds promising for a functional control of the non- collinear magnetism and thus interesting for exploring the AHE in different magnetic phases.

In this work, we consider gallium manganese nitride $GaNMn_3$ as a representative antiperovskite material to investigate the magnetic phase dependent AHC of the whole $ANMn_3$ family. The high temperature paramagnetic phase of $GaNMn_3$ has a cubic crystal structure with the space group $Pm\bar{3}m$. The Γ_{5g} phase emerges below room temperature [Fig. 3.1(a)] and represents the most common non-collinear AFM phase of the $ANMn_3$ compounds. In this phase, to avoid the frustration from the triangular geometry of the Ga-Mn Kagome-type lattice in the (111) plane, the magnetic moments of the three Mn atoms form a chiral configuration with the 120° angle between each other. The Γ_{4g} magnetic structure is another common non-collinear AFM phase in the $ANMn_3$ family, which can be obtained from the Γ_{5g} phase by rotating all magnetic moments around the [111] axis by 90° [Fig. 3.1(b)]. Both the Γ_{5g} and Γ_{4g} phases have zero net magnetization. $GaNMn_3$ also exhibits a non-collinear ferrimagnetic M-1 phase [Fig. 3.1(c)], which can be stabilized by stoichiometric deficiency or high pressure [16]. In this phase, the Mn magnetic moments are antiferromagnetically (ferromagnetically) coupled in (between) the Ga-Mn (001) planes, resulting in collinear AFM sublattices within these planes. On the other hand, the magnetic moments in the Mn-N (002) planes are arranged

non-collinearly [Fig. 3.1(c)], leading to the net magnetic moment along the [001] direction.

Using symmetry analyses and first-principles density-functional theory (DFT) calculations, we explore the AHE of the three non-collinear magnetic phases of $GaNMn_3$. We show that with nearly identical band structure, the nearly degenerate AFM Γ_{5g} and Γ_{4g} phases have zero and finite AHC, respectively. A similar behaviour is exhibited by non-collinear antiferromagnetic antiperovskites $SnNMn_3$ and $NiNMn_3$. In a non-collinear ferrimagnetic M-1 phase, $GaNMn_3$ exhibits a large AHC due to the presence of a sizeable net magnetization. With a possibility to control the appearance of these magnetic phases by external stimulus, the predicted variation of the AHC between different magnetic phases in the same material point to a new approach of designing the AHE-based functional devices for spintronic applications.

3.1. Symmetry Analysis

Within the linear response theory, the intrinsic AHC is expressed as the integral of the total Berry curvature ($\Omega_{\alpha\beta}$) over the Brillouin zone (BZ) of the crystal [1, 20]

$$\sigma_{\alpha\beta} = -\frac{e^2}{\hbar}\int_{BZ}\frac{d^3\vec{k}}{(2\pi)^3}\Omega_{\alpha\beta}(\vec{k}), \tag{3.1}$$

where the total Berry curvature $\Omega_{\alpha\beta} = \sum_n f_n(\vec{k})\Omega_n^{\gamma}(\vec{k})$ is the sum of the Berry curvatures $\Omega_{n,\alpha\beta}(\vec{k})$ corresponding the individual bands n, $f_n(\vec{k})$ is the Fermi distribution function, and indices (α, β) denote Cartesian co-ordinates. The expression for the Berry curvature $\Omega_{n,\alpha\beta}(\vec{k})$ is given by [1, 20]

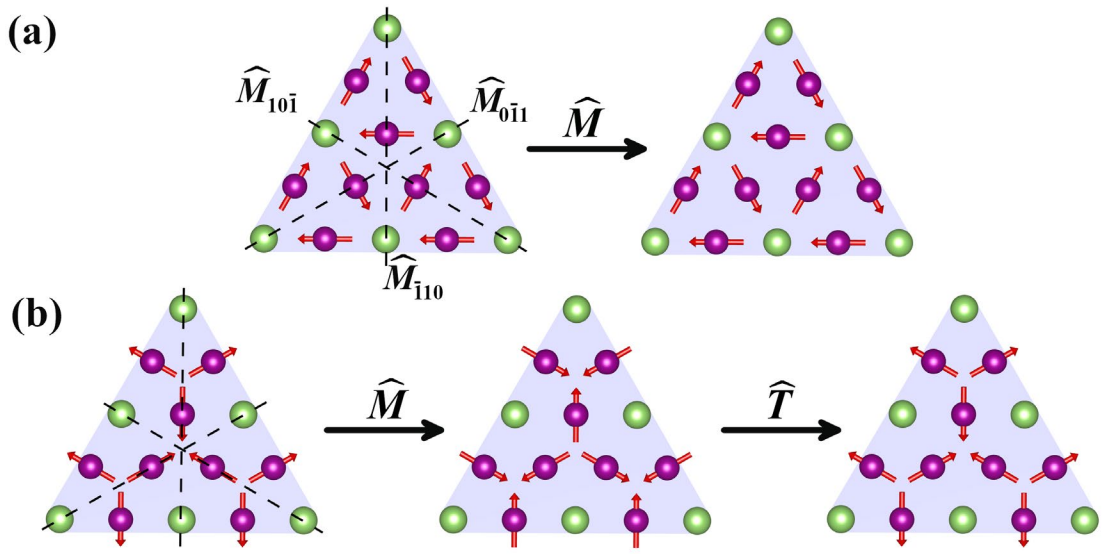

Figure 3.2. Symmetry operations for non-collinear AFM phases Γ_{5g} (a) and Γ_{4g} (b) in the (111) Ga-Mn plane of $GaNMn_3$. (a) The Γ_{5g} phase preserves mirror planes $(\bar{1}10)$, $(10\bar{1})$ and $(0\bar{1}1)$ (denoted by dashed lines) and is invariant under symmetry transformations $\widehat{M} = \widehat{M}_{0\bar{1}1}, \widehat{M}_{10\bar{1}}$, or $\widehat{M}_{\bar{1}10}$. (b) The Γ_{4g} phase does not preserve the mirror planes but is invariant under the product of mirror symmetry $\widehat{M}$ and time reversal symmetry $\hat{T}$. Red arrows denote the magnetic moments. Dotted lines denote the mirror planes.

$$\Omega_{n,\alpha\beta}(\vec{\mathrm{k}}) = -2\mathrm{i}\hbar^2 \sum_{\mathrm{m}\neq\mathrm{n}} \frac{\langle\psi_{n,\vec{\mathrm{k}}}|v_\alpha|\psi_{\mathrm{m},\vec{k}}\rangle\langle\psi_{m,\vec{k}}|v_\beta|\psi_{n,\vec{k}}\rangle}{(E_m(\vec{k}) - E_n(\vec{k}))^2}, \tag{3.2}$$

where $\psi_{n,\vec{k}}$ is the Bloch function and $\vec{v}$ is the velocity operator. Equation (3.2) represents one of the components of the Berry curvature vector given in Eq. (2.48). Space group symmetry of a material determines the presence or absence of a finite AHC. For example, as discussed in Chapter 2 (Section 2.3), since $\Omega_{n,\alpha\beta}(\vec{k})$ is odd with respect to time reversal symmetry, *i.e.*, $\Omega_{n,\alpha\beta}(-\vec{k}) = -\Omega_{n,\alpha\beta}(\vec{k})$, the total Berry curvature $\Omega_{\alpha\beta}$ and

hence the AHC are zero for non-magnetic materials. Similarly, if there is symmetry operation $\widehat{0}$ transforming $\vec{k}$ to $\vec{k}'$ (i.e., $\vec{k}' = \widehat{0}\vec{k}$), such as two-fold rotation or mirror reflection, for which $\widehat{0}\Omega_n(\vec{k}') = -\Omega_n(\vec{k})$, the AHC vanishes [12, 13]. In non-collinear AFM materials, such as $GaNMn_3$, various magnetic phases are associated with different magnetic space group symmetries (Table 3.1), resulting in different AHC.

Table 3.1. Matrix elements of the AHC tensor for different magnetic phases in $GaNMn_3$. Here, the ordinary Cartesian coordinates are used, *i.e.*, $\hat{x}||[100]$, $\hat{y}||[010]$, and $\hat{z}||[001]$.

Magnetic Phase	Γ_{5g}	Γ_{4g}	M-1
Magnetic Space Group	$R\bar{3}m$	$R\bar{3}m'$	P4
AHC tensor	$\begin{bmatrix} 0 & 0 & 0 \\ 0 & 0 & 0 \\ 0 & 0 & 0 \end{bmatrix}$	$\begin{bmatrix} 0 & \sigma_{xy} & -\sigma_{xy} \\ -\sigma_{xy} & 0 & \sigma_{xy} \\ \sigma_{xy} & -\sigma_{xy} & 0 \end{bmatrix}$	$\begin{bmatrix} 0 & \sigma_{xy} & 0 \\ -\sigma_{xy} & 0 & 0 \\ 0 & 0 & 0 \end{bmatrix}$

The Γ_{5g} phase of $GaNMn_3$ is characterized by a lattice of magnetic "whirls" composed of non collinear Mn magnetic moments in the (111) plane [Fig. 3.2(a)]. This arrangement forms the magnetic space group $R\bar{3}m$, which has three mirrors planes perpendicular to the (111) plane. Mirror symmetry *M* preserves the spin component perpendicular to the mirror plane and reverses the spin components parallel to the mirror plane. As shown in Fig. 3.2(a), the magnetic moments of the Mn atoms at the mirror plane are always perpendicular to this plane. Therefore, application of the symmetry transformations $\widehat{M} = \widehat{M}_{0\bar{1}1}, \widehat{M}_{10\bar{1}}$, or $\widehat{M}_{\bar{1}10}$ preserves the original configuration of magnetic moments. The invariance under these three mirror symmetry transformations

causes the AHE in the Γ_{5g} phase to vanish. For example, under the $M_{\bar{1}10}$ symmetry operation, the Berry curvature is transformed as $\widehat{M}_{\bar{1}10}\Omega_{xy}(k_y, k_x, k_z) = -\Omega_{xy}(k_x, k_y, k_z)$, which implies that the integral over the whole Brillouin zone in Eq. (3.1) leads to a zero σ_{xy}. Similarly, Ω_{yz} and Ω_{zx} are odd with respect to $\widehat{M}_{0\bar{1}1}$ and $\widehat{M}_{10\bar{1}}$, respectively. Table 3.2 shows details of different symmetry transfromations. These transformations are obtained using the symmetry properties of Eq. (2.52).

This odd property of the Berry curvature in $GaNMn_3$ under the mirror symmetry transformations is broken in the Γ_{4g} phase. In this phase, the Mn magnetic moments form a lattice of "vertices" in the (111) plane, in which the magnetic moments of the Mn atoms within the mirror plane are parallel to this plane [Fig. 3.2(b)]. This configuration corresponds to the magnetic space group $R\bar{3}m'$, in which the mirror symmetries are broken. As seen from Fig. 3.2(b), mirror symmetry transformation M reverses all the magnetic moments.

In contrast, the product of mirror symmetry $\widehat{M}$ and time reversal symmetry $\hat{T}$ is preserved in the Γ_{4g} phase. As shown in Fig. 3.2(b), when reversal of all moments by the mirror symmetry operation $\widehat{M}$ is followed by the time reversal symmetry transformation $\hat{T}$ all the moments are reversed back to their initial configuration. This clearly illustrates that $\hat{T}\widehat{M}$ symmetry allows finite out of plane magnetization (along [111] axis) but $\widehat{M}$ completely prohibits any finite magnetization. The presence of the combined $\hat{T}\widehat{M}$ symmetry makes the Berry curvature an even function of wave vector $\vec{k}$. For example, applying the $\hat{T}\widehat{M}_{\bar{1}10}$ transformation we obtain $\hat{T}\widehat{M}_{\bar{1}10}\Omega_{xy}(k_y, k_x, k_z) = \Omega_{xy}(-k_x, -k_y, -k_z)$. This even property of the Berry curvature with respect to

$\hat{T}\hat{M}_{\bar{1}10}$, $\hat{T}\hat{M}_{0\bar{1}1}$, and $\hat{T}\hat{M}_{10\bar{1}}$ makes the AHC non-zero in the Γ_{4g} phase. The complete analysis of the $\hat{T}\hat{M}$ symmetry transformations is given in Table 3.2.

Table 3.2. Symmetry transformations of wave vector $\vec{k}$ and Berry curvature $\vec{\Omega}$.

Transformation of $\vec{k}$	Transformation of $\vec{\Omega}$
$\hat{M}_{\bar{1}10}(k_y, k_x, k_z) = (k_x, k_y, k_z)$	$\hat{M}_{\bar{1}10}\Omega_{xy}(k_y, k_x, k_z) = -\Omega_{xy}(k_x, k_y, k_z)$ $\hat{M}_{\bar{1}10}\Omega_{zx}(k_y, k_x, k_z) = -\Omega_{yz}(k_x, k_y, k_z)$ $\hat{M}_{\bar{1}10}\Omega_{yz}(k_y, k_x, k_z) = -\Omega_{zx}(k_x, k_y, k_z)$
$\hat{M}_{0\bar{1}1}(k_x, k_z, k_y) = (k_x, k_y, k_z)$	$\hat{M}_{0\bar{1}1}\Omega_{xy}(k_x, k_z, k_y) = -\Omega_{zx}(k_x, k_y, k_z)$ $\hat{M}_{0\bar{1}1}\Omega_{yz}(k_x, k_z, k_y) = -\Omega_{yz}(k_x, k_y, k_z)$ $\hat{M}_{0\bar{1}1}\Omega_{zx}(k_x, k_z, k_y) = -\Omega_{xy}(k_x, k_y, k_z)$
$\hat{M}_{10\bar{1}}(k_z, k_y, k_x) = (k_x, k_y, k_z)$	$\hat{M}_{10\bar{1}}\Omega_{xy}(k_z, k_y, k_x) = -\Omega_{yz}(k_x, k_y, k_z)$ $\hat{M}_{10\bar{1}}\Omega_{yz}(k_z, k_y, k_x) = -\Omega_{xy}(k_x, k_y, k_z)$ $\hat{M}_{10\bar{1}}\Omega_{zx}(k_z, k_y, k_x) = -\Omega_{zx}(k_x, k_y, k_z)$
$\hat{T}\hat{M}_{\bar{1}10}(k_y, k_x, k_z) = (-k_x, -k_y, -k_z)$	$\hat{T}\hat{M}_{\bar{1}10}\Omega_{xy}(k_y, k_x, k_z) = \Omega_{xy}(-k_x, -k_y, -k_z)$ $\hat{T}\hat{M}_{\bar{1}10}\Omega_{yz}(k_y, k_x, k_z) = \Omega_{zx}(-k_x, -k_y, -k_z)$ $\hat{T}\hat{M}_{\bar{1}10}\Omega_{zx}(k_y, k_x, k_z) = \Omega_{yz}(-k_x, -k_y, -k_z)$
$\hat{T}\hat{M}_{0\bar{1}1}(k_x, k_z, k_y) = (-k_x, -k_y, -k_z)$	$\hat{T}\hat{M}_{0\bar{1}1}\Omega_{xy}(k_x, k_z, k_y) = \Omega_{zx}(-k_x, -k_y, -k_z)$ $\hat{T}\hat{M}_{0\bar{1}1}\Omega_{yz}(k_x, k_z, k_y) = \Omega_{yz}(-k_x, -k_y, -k_z)$ $\hat{T}\hat{M}_{0\bar{1}1}\Omega_{zx}(k_x, k_z, k_y) = \Omega_{xy}(-k_x, -k_y, -k_z)$
$\hat{T}\hat{M}_{10\bar{1}}(k_z, k_y, k_x) = (-k_x, -k_y, -k_z)$	$\hat{T}\hat{M}_{10\bar{1}}\Omega_{xy}(k_z, k_y, k_x) = \Omega_{yz}(-k_x, -k_y, -k_z)$ $\hat{T}\hat{M}_{10\bar{1}}\Omega_{yz}(k_z, k_y, k_x) = \Omega_{xy}(-k_x, -k_y, -k_z)$ $\hat{T}\hat{M}_{10\bar{1}}\Omega_{zx}(k_z, k_y, k_x) = \Omega_{zx}(-k_x, -k_y, -k_z)$

Magnetic space group symmetry determines the shape of the AHC tensor. While in the Γ_{5g} phase, all the nine components of the AHC tensor are zero, in the Γ_{4g} phase, corresponding to the magnetic space group $R\bar{3}m'$, the AHC tensor is non-zero. Table 3.1

shows that there are six non-vanishing matrix elements of the AHC tensor in the Γ_{4g} phase with only one σ_{xy} being independent.

In the non-collinear ferrimagnetic M-1 phase, the unit cell is a tetragonal $\sqrt{2} \times \sqrt{2} \times 1$ supercell of the conventional cubic unit cell without any distortion [Fig. 3.1 (c)]. In this phase, $GaNMn_3$ has a net magnetization along the [001] direction. Therefore, a non-zero AHC is expected in this case similar to that in ferromagnetic metals. Table 3.1 shows the AHC tensor for the magnetic space group symmetry P4 corresponding to the M-1 phase. Like in collinear ferromagnetic metals, the AHC tensor has two non-zero components with only one σ_{xy} being independent.

3.2. Calculation Methods

Next, we perform first-principles DFT calculations to obtain the AHC of the three non-collinear magnetic phases of $GaNMn_3$. The DFT calculations are performed using a plane-wave pseudopotential method with the fully-relativistic ultrasoft pseudopotentials [21] implemented in Quantum-ESPRESSO [22]. The exchange and correlation effects are treated within the generalized gradient approximation (GGA) [23]. We use the plane-wave cut-off energy of 52 Ry, the charge density cut-off energy of 520 Ry, and the *k*-point mesh of 16 × 16 × 16 for the cubic Γ_{5g} and Γ_{4g} phases and 12 × 12 × 16 for the tetragonal M-1 phase in $GaNMn_3$. Spin-orbit coupling is included in all the calculations. The electronic structure is converged to 10^{-7} eV/cell. The lattice parameters are obtained by fitting the calculated total energy to the Murnaghan equation of state [24].

The AHC is calculated using the PAOFLOW code [25] based on pseudo-atomic orbitals (PAO) [26, 27]. Tight-binding Hamiltonians are constructed from the non-self-

consistent DFT calculations with a 16 × 16 × 16 *k*-point mesh for the Γ_{5g} and Γ_{4g} phases and a 12 × 12 × 16 *k*-point mesh for the M-1 phase. Then, the AHC are calculated with a 48 × 48 × 48 *k*-point mesh for the Γ_{5g} and Γ_{4g} phases and a 46 × 46 × 48 *k*-point mesh for the M-1 phase using the adaptive broadening method. We find satisfactory convergence of the calculated AHC for a *k*-mesh of denser than 40×40×40. Increasing the grid size to 100×100×100 changed the AHC negligibly.

The symmetry determined geometries of the AHC tensor are obtained using the FINDSYM code and the linear response symmetry code [28]. The figures are created using VESTA [29] and gnuplot [30].

Table 3.3. Calculated lattice parameters *a* and AHC σ_{xy} for different magnetic phases of $ANMn_3$ (A = Ga, Ni, Sn).

	a (Å)			σ_{xy} ($\Omega^{-1}\mathrm{cm}^{-1}$)		
$ANMn_3$	Γ_{5g}	Γ_{4g}	M-1	Γ_{5g}	Γ_{4g}	M-1
$GaNMn_3$	3.87	3.87	3.82	0	40	377
$NiNMn_3$	3.84	3.84	-	0	130	-
$SnNMn_3$	3.99	3.99	-	0	133	-

3.3. Anomalous Hall Conductivity

The calculated lattice parameters of $GaNMn_3$ in different magnetic phases are listed in Table 3.3. For the Γ_{5g} phase of $GaNMn_3$, we find *a* = 3.869 Å, which is close to the experimental and previously calculated values [15, 16, 31– 33], and is identical to the calculated lattice parameter of Γ_{4g}. The calculated lattice parameter of the M-1 phase is smaller, which is consistent with the emergence of the M-1 phase in $GaNMn_3$ under high

pressure in experiment. We find that the Γ_{5g} phase is the ground state of $GaNMn_3$, while the total energies of the Γ_{4g} and M-1 phases are higher by 0.49 meV/f.u. and 164.35 meV/f.u., respectively [see Appendix B for ground state of other $ANMn_3$ antiperovskites]. This result is consistent with the experimental observations showing the appearance of the Γ_{5g} phase in $GaNMn_3$ at low temperature [15, 17, 34].

The calculated local magnetic moment in the Γ_{5g} and Γ_{4g} phases is about 2.16 μ_B/Mn atom, which is in a qualitative agreement with the experimental and previously calculated values [15, 16, 31, 32]. As expected, the non-collinear AFM configuration leads to a zero net magnetic moment. For the ferrimagnetic M-1 phase, we obtain 2.00 μ_B per Mn atom in the (001) plane and 1.47 μ_B/Mn atom in the (002) plane, resulting in the net magnetic moment of 1.80 μ_B /f.u pointing along the *z* direction.

Since Γ_{5g} and Γ_{4g} have similar magnetic structures, we first investigate the AHE in these two phases of $GaNMn_3$. Figure 3.3(a) shows the band structure of the Γ_{5g} phase. Five bands cross the Fermi energy (E_F). These dispersive bands are largely composed of the Mn-3*d* orbitals. It is seen that in some directions the bands are very close to each other. For example, along the Γ-Z and R-Γ directions, there are nearly degenerate bands. Figure 3.3(b) shows the calculated Berry curvature Ω_{xy}. It is seen that there are peaks along the R-Γ direction, which appear, according to Eq. (3.2), due to the small band separation between the three bands crossing E_F along this direction close to the Γ point [see Fig. 3.3(a)]. Along the Γ-Z direction, the Berry curvature Ω_{xy} is zero within the computation accuracy. This is due to the mirror symmetry $\widehat{M}_{\bar{1}10}$ which holds along this high symmetry direction, resulting in $\widehat{M}_{\bar{1}10}\Omega_{xy}(0,0,k_z) = -\Omega_{xy}(0,0,k_z)$, and hence $\Omega_{xy}(0,0,k_z) = 0$. In order to demonstrate the odd nature of the Berry curvature under the

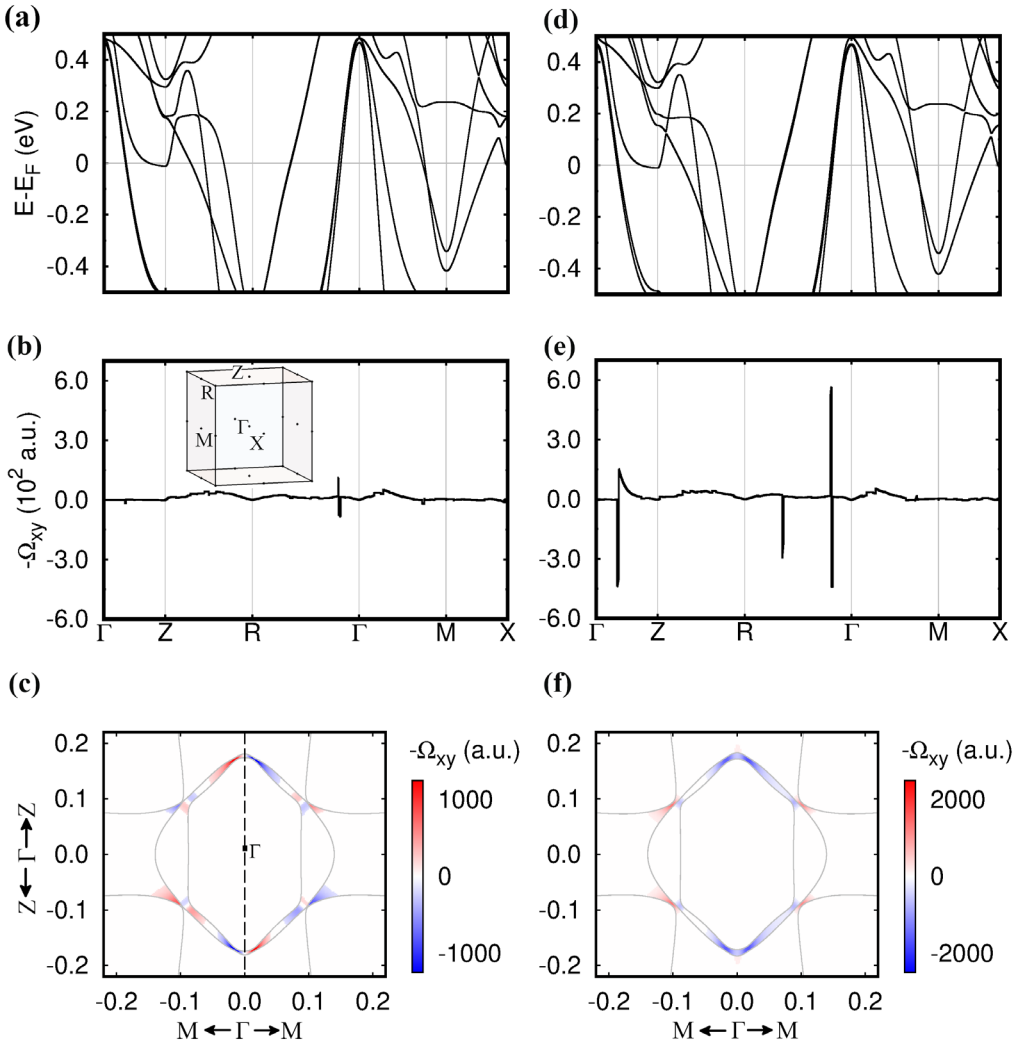

Figure 3.3. (a-c) The calculated band structure (a), Berry curvature Ω_{xy} along high symmetry path (b), and the color map of Ω_{xy} in the $(\bar{1}10)$ plane (c) for the Γ_{5g} phase of $GaNMn_3$. (d-f) The calculated band structure (d), Ω_{xy} along high symmetry path (e), and the color map of Ω_{xy} in the $(\bar{1}10)$ plane (f) for the Γ_{4g} phase of $GaNMn_3$. The inset of (b) shows the Brillouin zone. The solid lines and the dashed line in (c) and (f) denote the Fermi surfaces and the mirror plane $\widehat{M}_{\bar{1}10}$.

mirror symmetry $\widehat{M}_{\bar{1}10}$, we plot in Figure 3.3(c) the color map of Ω_{xy} around the Γ point in the (110) plane, which is perpendicular to the $(\bar{1}10)$ plane. It is seen that hot spots (*i.e.* regions where the absolute values of the Berry curvature are large) appear around the *k*-points where the Fermi surfaces of different bands (indicated by solid lines in [Fig. 3.3(c)]) cross. As is evident from Figure 3.3(c), Ω_{xy} changes sign with respect to the mirror symmetry transformation $\widehat{M}_{\bar{1}10}$ (reflection with respect to the dashed line in [Fig. 3.3(c)]). Clearly, integration of the Ω_{xy} over the whole Brillouin zone using Eq. (3.1) leads to zero AHC (within the computational accuracy) for the Γ_{5g} phase. As seen from Fig. 3.5(a), this property is independent of energy (Fermi energy).

Figure 3.3(d) shows the band structure of $GaNMn_3$ in the Γ_{4g} phase. The Γ_{4g} phase can be obtained from the Γ_{5g} phase by rotation of all magnetic moments around the [111] axis by 90°, in the absence of SOC the band structure of the two phases should be identical. Thus, the subtle differences in the bands structures in Figures 3.3(a) and 3.3(d) are due to SOC. These differences are seen, particularly, along the Γ-Z and Γ-R directions, where there is a slight increase in the band splitting around the Fermi energy.

Figure 3.3(e) shows the calculated Berry curvature of $GaNMn_3$ in the Γ_{4g} phase and reveals pronounced peaks in Ω_{xy} along the Γ-Z and Γ-R directions. According to the $\hat{T}\widehat{M}_{\bar{1}10}$ symmetry, Ω_{xy} is an even function of the wave vector $\vec{k}$, *i.e.* $\hat{T}\widehat{M}_{\bar{1}10}\Omega_{xy}(k_y, k_x, k_z) = \Omega_{xy}(-k_x, -k_y, -k_z)$. This is reflected in the calculated color map of Ω_{xy} around the Γ point in the (110) plane, which is shown in Figure 3.3(f). It is seen that the hot spots of Ω_{xy} appear nearly at the same locations as for the Γ_{5g} phase [Fig. 3.3 (c)]. However, in the Γ_{4g} phase, they are distributed symmetrically and have the

same sign, proving that Ω_{xy} is an even function with respect the $\hat{T}\hat{M}_{\bar{1}10}$ symmetry transformation. The AHC is calculated by integration of Ω_{xy} according to Eq. (3.2). Figure 3.5(a) shows that σ_{xy} is finite as a function of energy and at the Fermi energy $\sigma_{xy} = -40\ \Omega^{-1}cm^{-1}$. Clearly, the difference in the AHC between the Γ_{5g} and Γ_{4g} phases is due to the different magnetic space group symmetry of these phases.

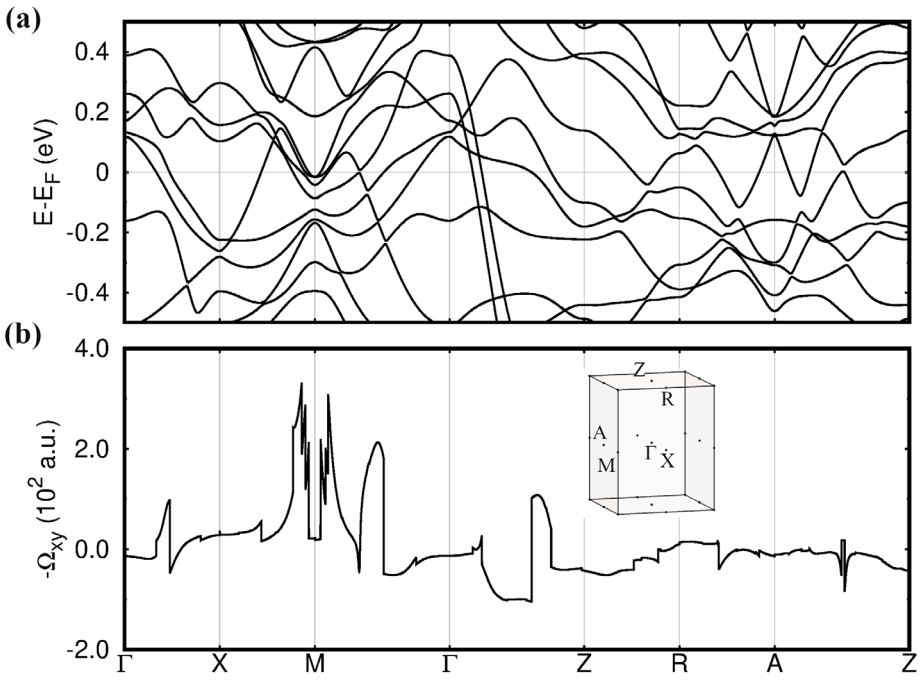

Figure 3.4. Calculated band structure (a) and Berry curvature Ω_{xy} (b) of $GaNMn_3$ in the M-1 phase along high symmetry paths in the Brillouin zone. The inset of (b) shows the Brillouin zone.

Figure 3.4(a) shows the calculated band structure of $GaNMn_3$ in the M-1 phase along high symmetry directions in the Brillouin zone. The band structure is more intricate compared to those for the Γ_{5g} and Γ_{4g} phases, because of a larger unit cell and more

complex magnetic configuration. The presence on the net magnetic moment breaks time reversal symmetry, which makes the AHC non-zero. Figure 3.4(b) shows the calculated Berry curvature Ω_{xy} along the high symmetry directions. It is seen that there are number of pronounced broad peaks which are associated with the multiple low dispersive bands around the Fermi energy which are coupled by the spin-orbit interaction. Figure 3.5(b) shows the calculated AHC as a function of energy in the M-1 phase. At the Fermi energy, $\sigma_{xy} = 377\ \Omega^{-1}cm^{-1}$ which is much larger than the AHC in the Γ_{4g} phase, due to the presence of the net magnetic moment in the M-1 phase. It is notable that σ_{xy} can be strongly enhanced in the M-1 phase by hole doping. For example, at $E = E_F - 0.1$ eV, the calculated value of σ_{xy} is as large as 816 $\Omega^{-1}cm^{-1}$ which is larger than the AHC in Fe (σ_{xy}~700 $\Omega^{-1}cm^{-1}$ [35]). The dependence of the AHC on different growth direction of the antipeovskite thin film can be find using Eq. C1 (Appendix C). The transformation of the AHC matrix tensors for Γ_{5g} and Γ_{4g} magnetic phases with $\hat{x}||[\bar{1}10]$, $\hat{y}||[\bar{1}\bar{1}2]$ and $\hat{z}||[111]$ are listed in Table C1 (Appendix C).

Similar properties are expected for other antiperovskite compounds, which may exhibit the non-collinear magnetic Γ_{4g} or Γ_{5g} phases. For comparison, we have calculated the AHC of antiperovskites $NiNMn_3$ and $SnNMn_3$, in which the Γ_{4g} phase exists at room temperature [14]. Consistent with the experiment, our calculations find that the Γ_{4g} phase is the ground state for these compounds. The calculated energy difference $\Delta E = E_{5g} - E_{4g}$ is 0.19 meV/f.u. for $NiNMn_3$ and 0.16 meV/f.u. for $SnNMn_3$. Large AHC over 100 $\Omega^{-1}\text{cm}^{-1}$ is predicted for the Γ_{4g} phase of $NiNMn_3$ and $SnNMn_3$, as indicated in Table 3.3. The AHE in the Γ_{4g} phase of $NiNMn_3$ has been recently observed experimentally,

which confirms our results [36]. Contrary to $GaNMn_3$, we find that the M-1 magnetic configuration is unstable in the $NiNMn_3$ and $SnNMn_3$ antiperovskites.

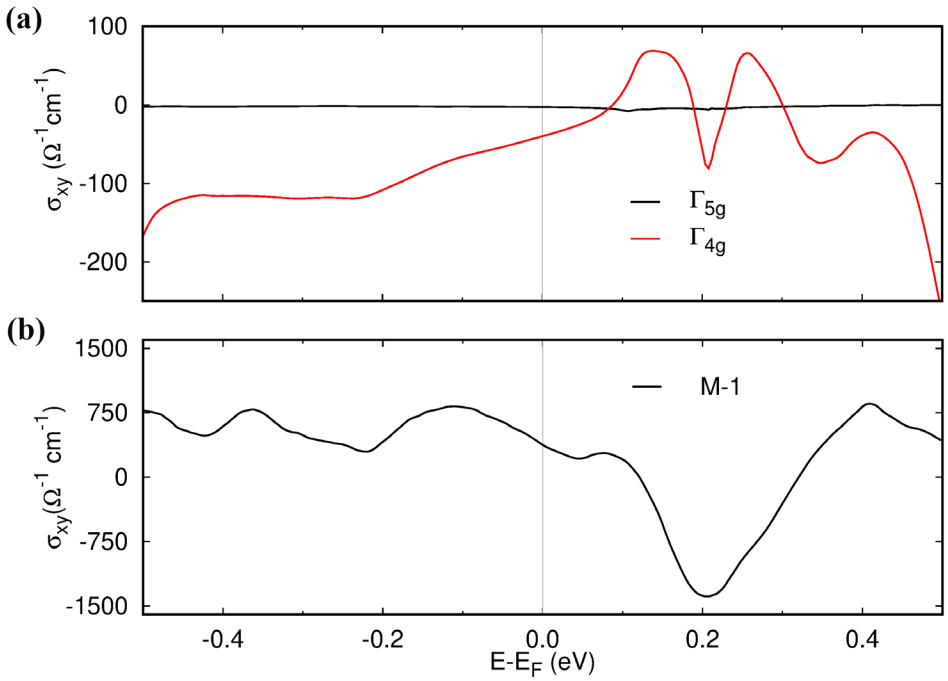

Figure 3.5. (a,b) Calculated AHC σ_{xy} as a function of energy for the Γ_{5g} and Γ_{4g} (a) and M-1 (b) phases of $GaNMn_3$.

Our results demonstrate that in the family of antiperovskite compounds, as represented by $ANMn_3$, the AHC is strongly dependent on the specific magnetic configuration. A significant change in the AHC can be produced by transitions between different magnetic phases. Such transitions can be driven by an external stimulus, provided that the energies of the different non-collinear magnetic phases are engineered to be nearly degenerate.

In experiment, the Γ_{5g} phase is found in the $ANMn_3$ compounds with A = Zn, Ga, and the Γ_{4g} phase is found for A = Ni, Ag, Sn [14]. The M-1 phase can be produced by non-stoichiometry and pressure [16]. These facts imply the sensitivity of the non-collinear magnetic phases to the chemical composition and lattice volume. Recently, monocrystalline $ANMn_3$ films have been successfully grown on different substrates, such as $SrTiO_3$, $BaTiO_3$, and LSAT [37, 38]. This opens a possibility to engineer antiperovskite compounds with nearly degenerate energies of the different magnetic phases by proper doping and suitable epitaxial strain produced by the substrate. In particular, the dynamic strain generated by a piezoelectric substrate, such as PMN-PT, can be used to realize the reversible switching between different magnetic phases.

Furthermore, since the AHC is odd under time reversal symmetry, the antiferromagnetic Γ_{4g} phase with a reversed Néel vector (corresponding to 180^o rotation of all magnetic moments in the (111) plane) is expected to have AHC of opposite sign. The Néel vector can be switched using a spin transfer torque induced by a spin polarized current [19], and its switching can be detected by the sign change of AHC. This functionality can be engineered by stoichiometry design of the antiperovskite compounds to tune the energy barrier between the two Γ_{4g} states of the opposite Néel vector ($\Delta E = E_{5g} - E_{4g}$) to a lower positive value. These possibilities make the $ANMn_3$ family of materials a promising platform for the AHE based applications of spintronic devices. In this work, we have studied the intrinsic AHC in different non-collinear magnetic phases of $GaNMn_3$, as a representative of a broader materials family of antiperovskite compounds $ANMn_3$ (A is a main group element). Based on the symmetry analysis and first-principles DFT calculations, we showed that the nearly degenerate non-collinear

AFM Γ_{5g} and Γ_{4g} phases of $GaNMn_3$ have zero and finite AHC, respectively. This difference was explained by the different magnetic space group symmetry of these phases. After the submission of our work, anomalous Hall effect in $ANMn_3$ compounds with similar results were published [36, 39]. We also predicted that $GaNMn_3$, in the non-collinear ferrimagnetic M-1 phase, exhibits large AHC which is comparable to the AHC in elemental ferromagnets, such as iron, and calculated the AHC of antiperovskites $SnNMn_3$ and $NiNMn_3$ exhibiting the Γ_{4g} ground state. We argued that by doping and strain it is possible to engineer the $ANMn_3$ compounds where the energy difference between these magnetic phases could be small, so that an external stimulus, such as the dynamic strain or the spin transfer torque could produce switchable magnetic phase transitions. Our work demonstrates that the antiperovskite family of non-collinear magnetic materials is a good platform to realize the multiple AHE states in a single compound, which is promising for novel spintronic applications.

References

[1] N. Nagaosa, J. Sinova, S. Onoda, A. H. MacDonald, and N. P. Ong, Anomalous Hall effect. *Rev. Mod. Phys.* **82**, 1539 (2010).

[2] D. Xiao, M.-C. Chang, and Q. Niu, Berry phase effects on electronic properties. *Rev. Mod. Phys.* **82**, 1959 (2010).

[3] Z. Fang, N. Nagosa, K. S. Takahashi, A. Asamitsu, R. Mathieu, T. Ogasawara, H. Yamada, M. Kawasaki, Y. Tokura, and K. Terakura, The anomalous Hall effect and magnetic monopoles in momentum space. *Science* **302**, 92 (2003).

[4] H. Chen, Q. Niu, and A. H. MacDonald, Anomalous Hall effect arising from noncollinear antiferromagnetism. *Phys. Rev. Lett*. **112**, 017205 (2014).

[5] J. Kübler and C. Felser, Non-collinear antiferromagnets and the anomalous Hall effect. *EPL* **108**, 67001 (2014).

[6] S. Nakatsuji, N. Kiyohara, and T. Higo, Large anomalous Hall effect in a non-collinear antiferromagnet at room temperature. *Nature* **527**, 212 (2015).

[7] A. K. Nayak, J. E. Fischer, Y. Sun, B. Yan, J. Karel, A. C. Komarek, C. Shekhar, N. Kumar, W. Schnelle, J. Kübler, C. Felser, and S. P. P. Parkin, Large anomalous Hall effect driven by a nonvanishing Berry curvature in the noncollinear antiferromagnet Mn_3Ge. *Sci. Adv.* **2**, e1501870 (2016).

[8] Y. Zhang, Y. Sun, H. Yang, J. Železný, S. P. P. Parkin, C. Felser, and B. Yan, Strong anisotropic anomalous Hall effect and spin Hall effect in the chiral antiferromagnetic compounds Mn_3X (X = Ge, Sn, Ga, Ir, Rh, and Pt). *Phys. Rev. B* **95**, 075128 (2017).

[9] A. H. MacDonald and M. Tsoi, Antiferromagnetic metal spintronics. *Phil. Trans. R. Soc. A* **369**, 3098 (2011).

[10] T. Jungwirth, X. Marti, P. Wadley, and J. Wunderlich, Antiferromagnetic spintronics. *Nat. Nanotech.* **11**, 231 (2016).

[11] O. Gomonay, V. Baltz, A. Brataa, and Y. Tserkovnyak, Antiferromagnetic spin textures and dynamics. *Nat. Phys.* **14**, 213 (2018).

[12] M. Seeman, D. Ködderitzsch, S. Wimmer, and H. Ebert, Symmetry-imposed shape of linear response tensors. *Phys. Rev. B* **92**, 155138 (2015).

[13] M. T. Suzuki, T. Koretsune, M. Ochi, and R. Arita, Cluster multipole theory for anomalous Hall effect in antiferromagnets. *Phys. Rev. B* **95**, 094406 (2017).

[14] D. Fruchart and E. F. Bertaut, Magnetic studies of the metallic perovskite-type compounds of manganese. *J. Phys. Soc. Jap.* **44**, 781 (1978).

[15] E. F. Bertaut, D. Fruchart, J. P. Bouchaud, and R. Fruchart, Diffraction neutronique de Mn_3GaN. *Solid St. Commun.* **6**, 251 (1968).

[16] K. Shi, Y. Sun, J. Yan, S. Deng, L. Wang, H. Wu, P. Hu, H. Lu, M. I. Malik, Q. Huang, and C. Wang, Baromagnetic effect in antiperovskite $Mn_3Ga_{0.95}N_{0.94}$ by neutron powder diffraction analysis. *Adv. Mater.* **28**, 3761 (2016).

[17] K. Takenaka, T. Inagaki, and H. Takagi, Conversion of magnetic structure by slight dopants in geometrically frustrated antiperovskite Mn_3GaN. *Appl. Phys. Lett.* **95**, 132508 (2009).

[18] S. Likubo, K. Kodama, K. Takenaka, H. Takagi, and S. Shamoto, Magnetovolume effect in $Mn_3Cu_{1-x}Ge_xN$ related to the magnetic structure: Neutron powder diffraction measurements. *Phys. Rev. B* **77**, 020409 (2008).

[19] H. Fujita, Field-free, spin-current control of magnetization in non-collinear chiral antiferromagnets. *Phys. Stat. Sol. (RRL)* **11**, 1600360 (2017).

[20] M. Gradhand, D. V. Fedorov, F. Pientka, P. Zahn, I. Mertig, and B. K. Györffy, First-principle calculations of the Berry curvature of Bloch states for charge and spin transport of electrons. *J. Phys.: Condens. Matt.* **24**, 213202 (2012).

[21] D. Vanderbilt, Soft self-consistent pseudopotentials in a generalized eigenvalue formalism. *Phys. Rev. B* **41**, 7892 (1990).

[22] P. Giannozzi et al., QUANTUM ESPRESSO: A modular and open-source software project for quantum simulations of materials. *J. Phys.: Condens. Matter* **21**, 395502 (2009).

[23] J. P. Perdew, K. Burke, and M. Ernzerhof, Generalized gradient approximation made simple. *Phys. Rev. Lett.* **77**, 3865 (1996).

[24] F. D. Murnaghan, The compressibility of media under extreme pressures. *Proc. Natnl. Acad. Sci. USA* **30**, 244 (1944).

[25] M. B. Nardelli, F. T. Cerasoli, M. Costa, S. Curtarolo, R. De Gennaro, M. Fornari, L. Liyanage, A. Supka, and H. Wang, PAOFLOW: A utility to construct and operate on ab-initio Hamiltonians from the projections of electronic wavefunctions on atomic orbital bases, including characterization of topological materials. *Comp. Mat. Sci.* **143**, 462 (2017).

[26] L. A. Agapito, A. Ferretti, A. Calzolari, S. Curtarolo, and M. B. Nardelli, Effective and accurate representation of extended Bloch states on finite Hilbert spaces. *Phys. Rev. B* **88**, 165127 (2013).

[27] L. A. Agapito, S. Ismail-Beigi, S. Curtarolo, M. Fornari, and M. B. Nardelli, Accurate tight-binding hamiltonian matrices from ab-initio calculations: Minimal basis sets. *Phys. Rev. B* **93**, 035104 (2016).

[28] J. Železný, *https://bitbucket.org/zeleznyj/linear*.

[29] K. Momma, and F. Izumi, VESTA: a three-dimensional visualization system for electronic and structural analysis. *J. Appl. Crystal.* **41**, 653 (2008).

[30] T. Williams, C. Kelley, H. B. Broker, J. Campbell, R. Cunningham, D. Denholm, E. Elber, R. Fearick, C. Grammes, and L. Hart, *Gnuplot* **4.5**: *An interactive plotting program, 2011. URL http://www. gnuplot. Info* (2017).

[31] P. Lukashev, R. F. Sabirianov, and K. Belashchenko, Theory of piezomagnetic effect in Mn-based antiperovskites. *Phys. Rev. B* **78**, 184414 (2008).

[32] J. Zemen, Z. Gercsi, and K. G. Sandeman, Piezomagnetism as a counterpart of the magnetovolume effect in magnetically frustrated Mn-based antiperovskite nitrides. *Phys. Rev. B* **96**, 024451 (2017).

[33] D.F. Shao, G. Gurung, T. R. Paudel, and E. Y. Tsymbal, Electrically reversible magnetization at the antiperovskite/ perovskite interface. *Phys. Rev. Mater.* **3**, 024405 (2019).

[34] D. Matsunami, A. Fujita, K. Takenaka, and M. Kano, Giant barocaloric effect enhanced by the frustration of the antiferromagnetic phase in Mn_3GaN. *Nat. Mater.* **14**, 73 (2015).

[35] Y. Yao, L. Kleinman, A. H. MacDonald, J. Sinova, T. Jungwirth, D. Wang, and Q. Niu, First-principles calculation of anomalous Hall conductivity in ferromagnetic bcc Fe. *Phys. Rev. Lett.* **92**, 037204 (2004).

[36] D. Boldrin, I. Samathrakis, J. Zemen, A. Mihai, B. Zou, B. Esser, D. McComb, P. Petrov, H. Zhang, and L. F. Cohen, The anomalous Hall effect in non-collinear antiferromagnetic Mn_3NiN thin films. *Phys. Rev. Mater.* **3**, 094409 (2019).

[37] D. Boldrin, A. P. Mihai, B. Zou, J. Zemen, R. Thompson, E. Ware, B. V. Neamtu, L. Ghivelder, B. Esser, D. W. McComb, P. Petrov, and L. F. Cohen, Giant piezomagnetism in Mn_3NiN. *ACS Appl. Mater. Interfaces* **10**, 18863 (2018).

[38] C. X. Quintela, K. Song, D.-F. Shao, L. Xie, T. R. Paudel, N. Campbell, M. S. Rzchowski, E. Y. Tsymbal, S.-Y. Choi, and C.B. Eom, Epitaxial antiperovskite/ perovskite heterostructures for materials design. *Sci. Adv.* **6**, eaba4017 (2020).

[39] X. Zhou, J. -P. Hanke, W. Feng, F. Li, G.-Y. Guo, Y. Yao, S. Blügel, and Y. Mokrousov, Spin-order dependent anomalous Hall effect and magneto-optical effect

in the noncollinear antiferromagnets Mn_3XN with X = Ga, Zn, Ag, or Ni. *Phys. Rev. B* **99**, 104428 (2019).

Chapter 4 Spin Torque Switching

As was discussed in the Chapter 1 (Section 1.4), antiferromagnets are promising candidates to replace ferromagnets in spintronic devices for information processing and storage [1- 3]. To realize this potential, however, new schemes to write and read the information, which is stored in the AFM Néel vector, are required. The absence of net magnetization in antiferromagnets makes the realization of these schemes more challenging compared to their ferromagnetic counterparts.

In Chapter 1 (Sections 1.2 and 1.3), we described different methods to manipulate and detect the Néel vector in antiferromagnets. As was discussed there, recent studies showed that manipulation of the AFM Néel vector can be achieved by passing an electric current across a metallic collinear antiferromagnet of certain magnetic group symmetry. For example, in the antiferromagnets, such as CuMnAs [4] and Mn_2Au [5], where the space-inversion symmetry is broken but the two spin sublattices form space-inversion partners, the inverse spin galvanic effect produces staggered field-like spin-torque on different sublattices [6, 7, 8]. When the electric current exceeds the critical value, this leads to switching of the Néel vector [4, 5]. In the bilayer heterostructures, such as NiO/Pt [9, 10] or Mn_2Au/Pt [11], switching of the Néel vector can be achieved as a result of the antidamping spin-torque produced by an injected spin current due to the spin-Hall effect. The detection of the AFM Néel vector in these structures is usually performed using anisotropic magnetoresistance (AMR) [12- 14] or spin-Hall magnetoresistance (SMR) effects [15- 18]. However, very small magnitudes of these effects (usually <1%) limit possible miniaturization and readout speed of these devices. Also, some of the observed magnetoresistive phenomena could have been an artifact of

the large writing currents and the associated thermal effects, rather than the Néel vector switching [19].

Using the anomalous Hall effect (AHE) [20] may be a more promising way to realize a detection scheme of the AFM order parameter [21]. In this regard, noncollinear AFM materials [22] could provide a viable alternative to their collinear counterparts. Recent studies have also shown that a number of high temperatures noncollinear antiferromagnets, such as Mn_3X (X = Ga, Ge, Sn or Ir) [23- 28] exhibit large anomalous Hall conductivities (AHC). Similarly, our results presented in chapter 3 also show that the noncollinear antiferromagnets $ANMn_3$ (A = Ga, Ag or Ni) possess large anomalous Hall conductivities (AHC) which agree well with other published results [29-31]. Due to the AHC being odd with respect to time reversal symmetry, reversal of the Néel vectors [32] in these compounds is expected to change sign of the AHE that can be used as an efficient detection scheme of the AFM order using the standard Hall measurements.

Switching of the AFM order in these non-collinear antiferromagnets can be achieved using a spin torque. It was argued that the magnetic structure of a non-collinear antiferromagnet can be dynamically controlled by injecting a spin current [33]. Using a simple two-dimensional model of a chiral antiferromagnet described by a single Kagomé layer, it was shown that spin structure can be rotated in the in-plane by spin-transfer torque [34]. Very recently, it was predicted that the injected spin current, when it is polarized perpendicular to the triangular plane, can drive a translational motion of a domain wall in the Γ_{4g}-type antiferromagnet [35].

These modelling results provide important insights into the spin-torque driven magnetization dynamics in noncollinear antiferromagnets. However, a realistic description of the AFM order switching based on the magnetic properties of these antiferromagnets obtained from first principles is missing. In this work, we combine density functional theory (DFT) calculations and atomistic spin-dynamics modelling based on the Landau-Lifshitz Gilbert-Slonczewski (LLGS) equation and predict that the spin torque can efficiently control the noncollinear AFM order in antiperovskite materials. We demonstrate that in antiperovskites $ANMn_3$ (A=Ga, Ni, etc.), the AFM order of the Γ_{4g} ground state can be switched on the picosecond scale by a spin current. The threshold switching current density can be tuned by the $ANMn_3$ stoichiometry engineering that changes the magnetocrystalline anisotropy. The anomalous Hall effect then can be used to detect the spin-torque switching of the AFM order.

A special interest has been attracted to Mn based antiperovskite nitrides $ANMn_3$ (A=Ga, Ni, Cu, Zn, etc,), where the AFM coupling within the frustrated Kagome lattice in the (111) plane results in a noncollinear alignment of the magnetic moments in the AFM phase such as Γ_{4g} [Fig. 4.1(a)] and Γ_{5g} (where all the Mn magnetic moments are rotated by 90º in the (111) plane). As mentioned in Chapter 1 (Section 1.4), these noncollinear AFM orderings lead to various functionalities such as magnetovolume [22, 36, 37], magnetocaloric [38, 39], piezomagnetic [40- 42], and magnetoelectric [43, 44] effects.

Recently, the AHE has been predicted theoretically and confirmed experimentally in Mn based antiperovskite nitrides with the Γ_{4g} AFM order [31, 45- 48]. Due to the

AHC being odd with respect to the time reversal symmetry operation, reversal of the AFM

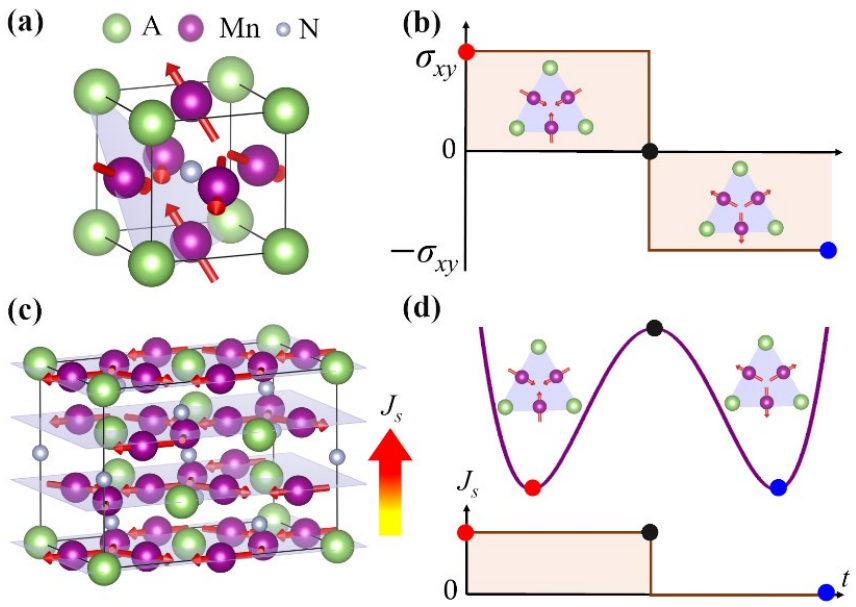

Figure 4.1. (a) A cubic unit cell of antiperovskite $ANMn_3$ in the noncollinear AFM Γ_{4g} state. Red arrows denote the Mn magnetic moments. (b) The sign change of the anomalous Hall conductivity σ_{xy} induced by AFM order switching. The insets show magnetic configurations of $ANMn_3$ in the (111) plane. (c) The orthorhombic supercell of $ANMn_3$ used for the modelling of spin dynamics. Spin current J_s along the [111] direction exerts a spin torque on the magnetic moments of $ANMn_3$. (d) The switching process of the AFM order driven by the spin torque. The spin torque rotates the magnetic moments of the AFM Γ_{4g} phase away from their initial energy minimum thought the metastable AFM Γ_{5g} phase. After overcoming the magnetic anisotropy barrier and releasing the current, the system relaxes to another minimum with the reversed AFM order.

order in the Γ_{4g} type antiperovskites is expected to change sign of the AHE [Fig. 4.1(b)]. This provides an efficient approach to distinguish between the two reversed AFM states in the Γ_{4g}-phase compounds. Thus, demonstrating a feasible method to switch between the two AFM states in the Γ_{4g} compounds would open a promising direction in AFM spintronics based on the AHE read-out.

Here, we explore spin-torque switching of the AFM order in antiperovskite compounds exhibiting the Γ_{4g} noncollinear antiferromagnetism. We consider an antiperovskite thin film stacked in the (111) plane with the Mn magnetic moments aligned noncollinear in this plane due to the AFM exchange coupling. The magnetic dynamics is induced by spin current J_s injected along the [111] direction, as shown in Fig. 4.1(c). The spin current may be carried by a spin-polarized charge current from an adjacent ferromagnetic layer or may be produced by an adjacent heavy-metal layer due to the spin Hall effect. The spin current J_s exerts a spin-transfer torque rotating the Mn magnetic moments in the (111) plane. The related magnetization dynamics is determined by the LLGS equation as discussed in the theoretical methods (Chapter 2) [49, 50, 51]:

$$\frac{\partial \vec{m}_i}{\partial t} = -\gamma\left(\vec{m}_i \times \vec{H}_i\right) + \alpha_G\left(\vec{m}_i \times \frac{\partial \vec{m}_i}{\partial t}\right) + +\gamma\left(\vec{m}_i \times \vec{H}_i^s\right). \tag{4.1}$$

Here α_G is the Gilbert damping constant, γ is the gyromagnetic ratio, $\vec{m}_i = \frac{\vec{M}_i}{|\vec{M}_i|}$ is the unit magnetization vector for each sublattice with the magnetization $\vec{M}_i$. The magnetic field $\vec{H}_i = -\frac{1}{\mu}\frac{\partial H}{\partial \vec{m}_i}$ is determined by the spin Hamiltonian:

$$H = -\sum_{i \neq j} J_{ij}\vec{m}_i \cdot \vec{m}_j - K\sum_i (\hat{n}_i \cdot \vec{m}_i)^2, \tag{4.2}$$

where μ is the magnetic moment of a Mn atom, J_{ij} is the exchange coupling energy between sublattices, K is the magnetic anisotropy energy per Mn atom, and $\hat{n}_i$ is the direction of the easy axis for each sublattice. $\vec{H}_i^S = h_s(\vec{m}_i \times \vec{p}_s)$ is the effective magnetic field produced by the spin current J_s with the spin polarization along the $\vec{p}_s$ direction. The coefficient h_s is given by $h_s = \frac{\hbar J_s}{eLM}$, where $M = |\vec{M}_i|$ is the magnitude of the sublattice magnetization, e is the electronic charge, $\hbar$ is the Planck's constant, L is thickness of the sample. This effective field generates the spin torque ~$\vec{m}_i \times \vec{H}_i^S$, which drives the magnetization dynamics.

To reverse the AFM order, all the moments need to be rotated by 180° within the horizontal plane [Fig. 4.1(d)]. If $\vec{p}_s$ is along an in-plane direction, the induced out-of-plane field $\vec{H}_i^S$ will have a tendency to reorient the moments out-of-plane. This will produce an additional parallel magnetic component which is energetically unfavourable due to the intrinsic AFM exchange coupling between the moments. On the other hand, if $\vec{p}_s$ is along the out-of-plane direction, i.e., $\vec{p}_s = \hat{z}$, the induced field $\vec{H}_i^S = h_s(\vec{m}_i \times \hat{z})$ is along the in-plane direction perpendicular to $\vec{m}_i$ (black arrows in Fig. 4.2(a)). In this case, the staggered field $\vec{H}_i^S$ will rotate the magnetic moments in three sublattices nearly uniformly, not affecting the 120° angles between the nearest magnetic moments. This won't cost the exchange energy and thus is more favourable for the switching. Therefore, below we consider the spin-torque switching driven by spin current J_s with the spin polarization $\vec{p}_s$ along the $\hat{z}$ direction.

4.1. Calculation Methods

In this work, we perform DFT calculations using VASP [52] and Quantum-ESPRESSO [53] codes. In VASP, the projector augmented wave method [54] is used. In Quantum-ESPRESSO, the plane-wave pseudopotential method with the fully relativistic ultrasoft pseudopotentials [55] is employed. The exchange and correlation effects are treated within the generalized gradient approximation (GGA) similar as we did in Chapter 3 [56]. The *k*-point mesh of 16×16×16 is used in the irreducible Brillouin zone. Spin-orbit coupling is included in all the calculations. All the atomic co-ordinates are relaxed until the force on each atom was less than 0.01 eV/Å. In the calculations, we firstly set the initial magnetic configurations according to the experimentally observed magnetic states, and then perform full relaxations for both the crystal structure, the magnetic structure, and the electronic structure without any constraint. The magnetic ground state is determined by comparing the energies of those states with the converged magnetic structures.

In order to simulate the doping effect in $Ga_{1-x}Ni_xNMn_3$, we consider a $ANMn_3$ cell where the pseudopotential is generated by compositionally averaging the potentials of Ga and Ni as $\hat{V}_{ps}^{A} = x\hat{V}_{ps}^{Ni} + (1-x)\hat{V}_{ps}^{Ga}$ based on the virtual crystal approximation. This is a widely used treatment of the A-site doping effect in antiperovskite AXM_3 [57], since the band structures near the Fermi level of AXM3 are majorly contributed by the d electrons of the transition metal M.

The atomistic spin-dynamics modelling is performed using the Vampire code [58]. The AHC is calculated using the PAOFLOW code [59] based on pseudo-atomic orbitals (PAO) [60, 61]. Tight-binding Hamiltonians are constructed from the non-self-

consistent DFT calculations with a 16×16×16 *k*-point mesh. Then, the AHC is calculated with a 48×48×48 *k*-point mesh using the adaptive broadening method [62].

4.2. Atomistic Modelling of Spin Torque Switching

The atomistic modelling of the spin-torque dynamics is performed using an $ANMn_3$ (111) slab of thickness L = 6 nm which consists of periodically repeated supercells [Fig. 4.1(c)]. Specifically, we consider $NiNMn_3$, an antiperovskite metal, which AFM Γ_{4g} order and non-vanishing AHE effect near room temperature have been confirmed recently [31, 46]. Consistent with the experiments, our DFT calculation shows that the Γ_{4g} order with negligible net magnetization has the lowest energy among the tested magnetic states in $NiNMn_3$. The parameters in Eq. (4.2) for $NiNMn_3$ are obtained from our DFT calculations. We found that each Mn atom has the moment of 2.76 μ_B and Ni atom doesn't have the local magnetic moment. The exchange constant J_{ij} is found to be –24 meV, using the energy mapping method [63]. Reversal of the Γ_{4g} magnetic structure by 180° rotation of all magnetic moments about the [111] axis passes through the Γ_{5g} magnetic structure (90° rotation), which has higher energy due to magnetic anisotropy [Fig. 4.1(d)]. By calculating the energy difference between the Γ_{5g} and Γ_{4g} phases, we find that the magnetic anisotropy constant $K = (E_{5g} - E_{4g})/3 \approx 0.03$ meV per Mn atom. The damping constant α_G has been found experimentally to be in the range of 0.05 to 0.28 for similar non-collinear magnets [64, 65]. In our modelling, we assume $\alpha_G = 0.1$ and gyromagnetic ratio $\gamma = 1.76 \times 10^{11} \mathrm{T^{-1}s^{-1}}$.

Figure 4.2(a) (top panel) shows the initial magnetic configuration, where the magnetic moments $\vec{m}_1$, $\vec{m}_2$, and $\vec{m}_3$ for the three sublattices point toward the centre of the triangle formed by the nearest Mn atoms. In order to track the simulated spin-torque

switching process, we observe variation of $\vec{m}_1$, which initially has zero *x*-component (m_{1x}) and maximum *y*-component (m_{1y}). Figure 4.2(a) (bottom panel) shows the rotation of $\vec{m}_1$ due to the spin torque produced by spin current density $J_s = 1.8\times 10^{12}$ A/m^2: when the current is turned on, m_{1x} and m_{1y} start to oscillate, revealing the clockwise rotation of the moments. The time period of these oscillations is $\tau \approx 9.8$ ps, which corresponds to the frequency of $f \approx 0.1$ THz as expected in antiferromagnets. The observed oscillation frequency qualitatively agree with that predicted in ref. 33, i.e. $f \approx \frac{1}{4\pi\sqrt{3}}\frac{J_s}{J_c}\frac{\gamma K}{\alpha_G \mu}$, where J_c is the critical current density (see discussion below). We note that the predicted AFM dynamics may be interesting for the development of compact generators of coherent radiation in the THz frequency range, which are important for different technological applications [66, 67, 68].

The 180° rotation of the moments can be achieved by application of a spin current pulse, which duration is a half time of the oscillation period, *i.e.*, $\tau/2 \approx 4.9$ ps. As shown in Figure 4.2(b), applying such a pulse to the original magnetic configuration of $NiNMn_3$, where all three Mn magnetic moments $\vec{m}_1$, $\vec{m}_2$, and $\vec{m}_3$ are pointing to the center of the triangle formed by the nearest Mn atoms, switches $\vec{m}_1$, $\vec{m}_2$, and $\vec{m}_3$ to be pointing away from the center of the triangle. The switching occurs through an intermediate Γ_{5g} phase where the magnetic moments are aligned in a vortex. Applying a 4.9 ps pulse again switches the magnetic structure back to the initial configuration. These results demonstrate a possibility of an ultrafast spin-torque switching of the AFM order in $NiNMn_3$.

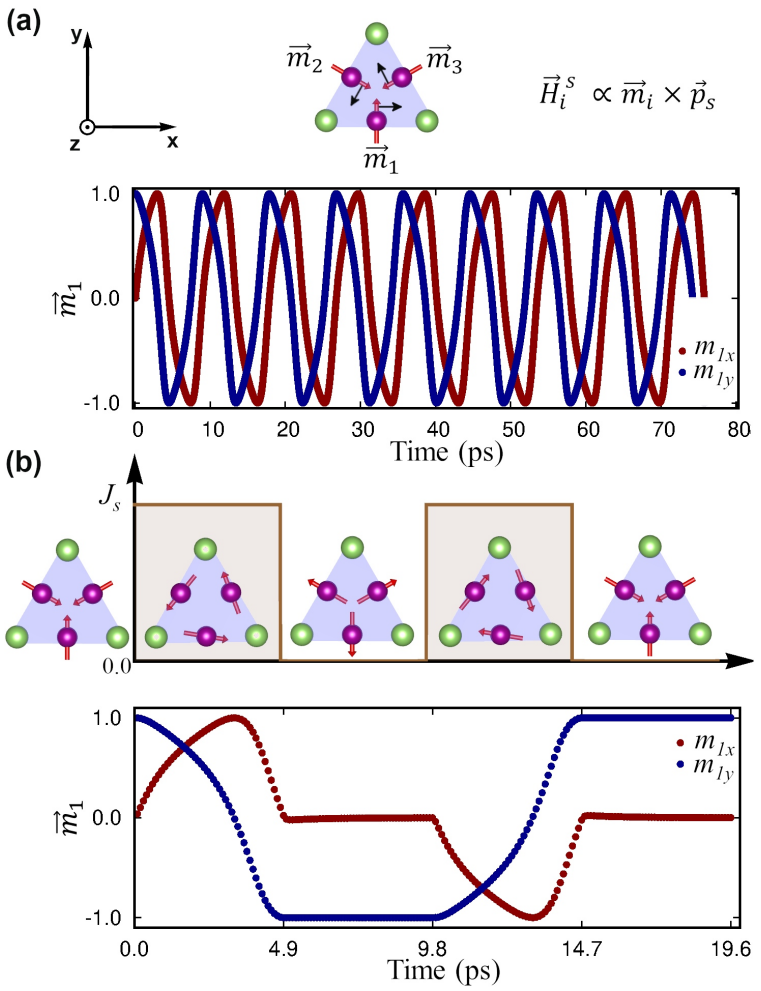

Figure 4.2. Spin dynamics in antiperovskite $NiNMn_3$. (a) Top panel: schematic of effective magnetic field $\vec{H}_i^s$ (black arrows) on the three sublattices $\vec{m}_1$, $\vec{m}_2$, and $\vec{m}_3$ generated by spin current Js with the spin polarization $\vec{p}_s$ along the z-direction. Bottom panel: time-dependent variations of the x- and y- components of $\vec{m}_1$ during the application of spin current $J_s = 1.8\times 10^{12}$ A/m^2. (b) Top panel: schematic of the spin-torque switching process induced by two spin-current pulses. Bottom panel: time-dependent variations of the x- and y- components of $\vec{m}_1$ driven by applying the two spin-current pulses of 4.9 ps in duration.

The spin current is produced either by a spin-polarized charge current or a charge current resulting in the spin Hall effect. Since a large charge current generates Joule heat and thus energy consuming, it is desirable to reduce its density and hence J_s required for the spin-torque switching. The major factor influencing J_s is the anisotropy energy [33, 69]. In order to reorient Mn magnetic moments, the Zeeman energy μh_s of the magnetic moment in the effective field $\vec{H}_i^S$ generated by J_s should overcome the anisotropy energy K, *i.e.*, $\mu h_s > K$. This condition leads to the critical current density $J_c = \frac{KLe}{\hbar V}$, where V is the volume of the cubic unit cell of $NiNMn_3$. This result for J_c is identical to that obtained in ref. 33. Since J_c is proportional to K, reducing the magnetic anisotropy is expected to reduce the critical current density.

This expectation is confirmed by our atomistic modelling of the spin-torque switching of $NiNMn_3$, where we fix all the parameters but vary the magnetic anisotropy constant K. As expected, and seen from Fig. 4.3(a), with decreasing K the J_c decreases linearly. According to our modelling results, the critical current density J_c is reduced to about 10^{10} A/m^2 if the anisotropy constant K is 0.01 meV per Mn atom. The calculated critical current density is in agreement with that predicted by the simple estimate $J_c = \frac{KLe}{\hbar V}$ [see the solid line in Fig. 4.3(a)].

The magnetic anisotropy of the antiperovskite can be controlled by chemical doping. There are a number of antiperovskites with the AFM Γ_{5g} order, such as $GaNMn_3$. Therefore, a doped compound $Ga_{1-x}Ni_xNMn_3$ is expected to exhibit the ground Γ_{5g} state in the Ga rich phase and the Γ_{4g} state in the Ni rich phase. At the intermediate doping x, there should be a transition point between these two phases, where the magnetic

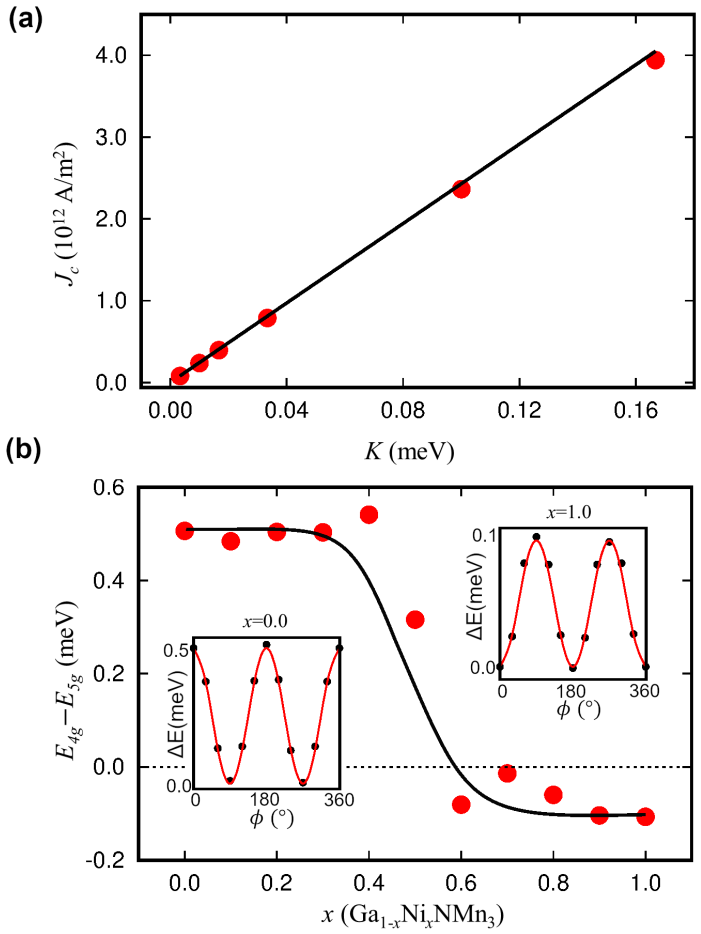

Figure 4.3. (a) Critical current density J_c for switching of the AFM order in $ANMn_3$ antiperovskite as a function of the anisotropy energy. The red dots are J_c obtained by the atomistic spin dynamics modelling. The solid black line is obtained from $J_c = \frac{KLe}{\hbar V}$. (b) The energy difference between the Γ_{4g} and Γ_{5g} magnetic configurations in $Ga_{1-x}Ni_xNMn_3$. The insets show the energy as a function of rotation angle ϕ of the magnetic moments around the [111] axis in $Ga_{1-x}Ni_xNMn_3$ for x = 0 ($GaNMn_3$) and x = 1 ($NiNMn_3$), where $\Delta E = E_{4g} - E(\phi)$.

anisotropy is zero. Figure 4.3(b) shows the calculated energy difference between the Γ_{5g} and Γ_{4g} magnetic orderings as a function of doping x. Consistent with experimental results, we find that the ground state is Γ_{5g} for $GaNMn_3$ ($x = 0$) and Γ_{4g} for $NiNMn_3$ ($x = 1$). There is a transition between the two phases for $x \approx 0.58$. At this region, the magnetic anisotropy is strongly reduced, and the small critical current density $\sim 10^{10}\ \mathrm{A}/m^2$ is expected for spin-torque switching of the AFM order.

Switching of the AFM order in the Γ_{4g} phase can be detected by measuring the anomalous Hall conductivity, as was discussed in Chapter 3. The Berry curvature is odd under certain symmetry operations, *i.e.*, $\hat{O}\Omega_n(\vec{k}') = -\Omega_n(\vec{k})$, where $\hat{O}$ is a symmetry operation such as time reversal symmetry or mirror symmetry as was discussed in Chapter 3 and seen from Table 3.2 [70 , 71]. Table 3.2 shows that in the Γ_{4g} AFM state, there is no such symmetry operation $\hat{O}$ with respect to which Ω_n is odd [31]. Therefore, a finite value can be obtained according to Eq. (4.4), leading to the appearance of the anomalous Hall effect. Figure 4.4 shows the calculated AHC σ_{xy} of $Ga_{1-x}Ni_xNMn_3$ as a function of energy for $x = 0.58$. We find sizable $\sigma_{xy} = 260\ \Omega^{-1}cm^{-1}$ at the Fermi energy. Rotating the magnetic moments around the [111] axis changes the magnetic space group and thus the band structure, which affects the magnitude of σ_{xy} [72]. As shown in Appendix D, σ_{xy} decreases when the moments are rotated away from their initial alignment in the Γ_{4g} state and vanishes when the moments are aligned in the Γ_{5g} state. The AHC changes sign with reversal of the AFM order, as shown in Fig. 4.4.

We note that the AFM order can be switched in the antiperovskite $ANMn_3$ films layered in the plane different from (111). As long as the spin-polarization of the spin current has the component perpendicular to the (111) plane, the spin-torque switching of

the noncollinear AFM order can be achieved. The spin current can be generated from a non-metal bottom layer through the spin Hall effect. Recently, such a spin-Hall torque switching has been reported in the $GaNMn_3$ (001)/Pt bilayer structure [73]. In this

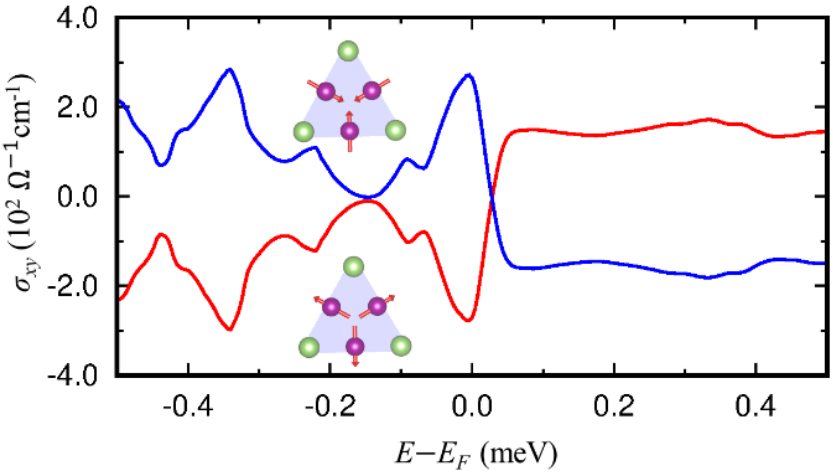

Figure 4.4. Calculated anomalous Hall conductivity (AHC) σ_{xy} of antiperovskite $Ga_{0.42}Ni_{0.58}NMn_3$ with the AFM Γ_{4g} order as a function of energy. The red and blue lines denote the AHC for the two AFM states with reversed magnetic structure shown in the insets.

experiment that AFM switching was detected using a conventional AMR effect, since the noncollinear AFM Γ_{5g} phase in Mn_3GaN does not support the AHE [31]. The sign change of the AHC in noncollinear AFM antiperovskites exhibiting the AFM Γ_{4g} phase, which is demonstrated in our paper, is advantageous for the AFM order detection compared to the conventional AMR and SMR measurements.

In conclusion, we have predicted a possibility of spin-torque switching of the noncollinear AFM order in Mn-based antiperovskite nitrides, such as $NiNMn_3$. We have shown that this switching can be achieved on the picosecond time scale using a spin-

current density feasible in experiment. The critical current density for AFM switching can be reduced by controlling the magnetocrystalline anisotropy through the stoichiometry engineering. For the antiperovskite compound $Ga_{1-x}Ni_xNMn_3$ with $x \approx 0.58$, we have predicted the critical spin-current density $J_c \sim 10^{10}$ A$/m^2$ and sizable anomalous Hall conductivity $\sigma_{xy} = 260\ \Omega^{-1}cm^{-1}$. The anomalous Hall conductivity changes sign with the AFM switching and hence can be used for the AFM order detection. Our prediction offers a new material platform based on noncollinear AFM antiperovskites to realize both the efficient manipulation and detection of the AFM order, which is promising for the next generation of the AFM spintronic devices.

References

[1] T. Jungwirth, X. Marti, P. Wadley, and J. Wunderlich, Antiferromagnetic spintronics. *Nat. Nanotech.* **11**, 231 (2016).

[2] V. Baltz, A. Manchon, M. Tsoi, T. Moriyama, T. Ono, and Y. Tserkovnyak, Antiferromagnetic spintronics. *Rev. Mod. Phys.* **90**, 015005 (2018).

[3] T. Jungwirth, J. Sinova, A. Manchon, X. Marti, J. Wunderlich, and C. Felser, The multiple directions of antiferromagnetic spintronics. *Nat. Phys.* **14**, 200 (2018).

[4] P. Wadley, B. Howells, J. Železný, C. Andrews, V. Hills, R. P. Campion, V. Novák, K. Olejník, F. Maccherozzi, S. S. Dhesi, S. Y. Martin, T. Wagner, J. Wunderlich, F. Freimuth, Y. Mokrousov, J. Kuneš, J. S. Chauhan, M. J. Grzybowski, A. W. Rushforth, K. W. Edmonds, B. L. Gallagher, and T. Jungwirth, Electrical switching of an antiferromagnet. *Science* **351**, 587 (2016).

[5] S. Y. Bodnar, L. Šmejkal, I. Turek, T. Jungwirth, O. Gomonay, J. Sinova, A. A. Sapozhnik, H.-J. Elmers, M. Kläui, and M. Jourdan, Writing and reading

antiferromagnetic Mn_2Au by Néel spin-orbit torques and large anisotropic magnetoresistance. *Nat. Commun.* **9**, 348 (2018).

[6] J. Železný, H. Gao, K. Výborný, J. Zemen, J. Mašek, A. Manchon, J. Wunderlich, J. Sinova, and T. Jungwirth, Relativistic Néel-order fields induced by electrical current in antiferromagnets. *Phys. Rev. Lett.* **113**, 157201 (2014).

[7] J. Železný, H. Gao, A. Manchon, F. Freimuth, Y. Mokrousov, J. Zemen, J. Mašek, J. Sinova, and T. Jungwirth, Spin-orbit torques in locally and globally noncentrosymmetric crystals: Anti-ferromagnets and ferromagnets. *Phys. Rev. B* **95**, 014403 (2017).

[8] A. Manchon, J. Zelezný, I. M. Miron, T. Jungwirth, J. Sinova, A. Thiaville, K. Garello, and P. Gambardella, Current-induced spin-orbit torques in ferromagnetic and antiferromagnetic systems. *arXiv*:1801.09636 (2018).

[9] X. Z. Chen, R. Zarzuela, J. Zhang, C. Song, X. F. Zhou, G. Y. Shi, F. Li, H. A. Zhou, W. J. Jiang, F. Pan, and Y. Tserkovnyak, Antidamping torque-induced switching in biaxial antiferromagnetic insulators. *Phys. Rev. Lett.* **120**, 207204 (2018).

[10] T. Moriyama, K. Oda, T. Ohkochi, M. Kimata, and T. Ono, Spin torque control of antiferromagnetic moments in NiO. *Sci. Rep.* **8**, 14167 (2018).

[11] X. F. Zhou, X. Z. Chen, J. Zhang, F. Li, G. Y. Shi, Y. M. Shun, M. S. Saleem, Y. F. You, F. Pan, and C. Song, From fieldlike torque to antidamping torque in antiferromagnetic Mn_2Au. *Phys. Rev. Applied* **11**, 054030 (2019).

[12] B. G. Park, J. Wunderlich, X. Martí, V. Holý, Y. Kurosaki, M. Yamada, H. Yamamoto, A. Nishide, J. Hayakawa, H. Takahashi, A. B. Shick, and T. Jungwirth, A

spin-valve-like magnetoresistance of an antiferromagnet-based tunnel junction. *Nat. Mater.* **10**, 347 (2011).

[13] X. Martí, B. G. Park, J. Wunderlich, H. Reichlová, Y. Kurosaki, M. Yamada, H. Yamamoto, A. Nishide, J. Hayakawa, H. Takahashi, and T. Jungwirth, Electrical measurement of antiferromagnetic moments in exchange-coupled IrMn/NiFe stacks. *Phys. Rev. Lett.* **108**, 017201 (2012).

[14] Y. Y. Wang, C. Song, B. Cui, G. Y. Wang, F. Zeng, and F. Pan, Room-temperature perpendicular exchange coupling and tunneling anisotropic magnetoresistance in an antiferromagnet-based tunnel junction. *Phys. Rev. Lett.* **109**, 137201 (2012).

[15] H. Nakayama, M. Althammer, Y.-T. Chen, K. Uchida, Y. Kajiwara, D. Kikuchi, T. Ohtani, S. Geprägs, M. Opel, S. Takahashi, R. Gross, G. E. W. Bauer, S. T. B. Goennenwein, and E. Saitoh, Spin Hall magnetoresistance induced by a nonequilibrium proximity effect. *Phys. Rev. Lett.* **110**, 20 6601 (2013).

[16] H. Wang, D. Hou, Z. Qiu, T. Kikkawa, E. Saitoh, and X. Jin, Antiferromagnetic anisotropy determination by spin Hall magnetoresistance. *J. Appl. Phys.* **122**, 083907 (2017).

[17] D. Hou, Z. Qiu, J. Barker, K. Sato, K. Yamamoto, S. Vélez, J. M. Gomez-Perez, L. E. Hueso, F. Casanova, and E. Saitoh, Tunable sign change of spin Hall magnetoresistance in Pt/NiO/YIG structures. *Phys. Rev. Lett.* **118**, 147202 (2017).

[18] L. Baldrati, A. Ross, T. Niizeki, C. Schneider, R. Ramos, J. Cramer, O. Gomonay, M. Filianina, T. Savchenko, D. Heinze, A. Kleibert, E. Saitoh, J. Sinova, and M. Kläui, Full angular dependence of the spin Hall and ordinary magnetoresistance in epitaxial antiferromagnetic NiO(001)/Pt thin films. *Phys. Rev. B* **98**, 024422 (2018).

[19] C. C. Chiang, S. Y. Huang. D. Qu, P. H. Wu, and C. L. Chien, Absence of evidence of electrical switching of the antiferromagnetic Néel vector. *Phys. Rev. Lett.* **123**, 227203 (2019).

[20] N. Nagaosa, J. Sinova, S. Onoda, A. H. MacDonald, and N. P. Ong, Anomalous Hall effect. *Rev. Mod. Phys.* **82**, 1539 (2010).

[21] T. Kosub, M. Kopte, R. Hühne, P. Appel, B. Shields, P. Maletinsky, R. Hübner, M. O. Liedke, J. Fassbender, O. G. Schmidt, and D. Makarov, Purely antiferromagnetic magnetoelectric random access memory. *Nat. Commun.* **8**, 13985 (2017).

[22] D. Fruchart and E. F. Bertaut, Magnetic studies of the metallic perovskite-type compounds of manganese. *J. Phys. Soc. Jap.* **44**, 781 (1978).

[23] H. Chen, Q. Niu, and A. H. MacDonald, Anomalous Hall effect arising from noncollinear antiferromagnetism. *Phys. Rev. Lett*. **112**, 017205 (2014).

[24] J. Kübler and C. Felser, Non-collinear antiferromagnets and the anomalous Hall effect. *EPL* **108**, 67001 (2014).

[25] S. Nakatsuji, N. Kiyohara, and T. Higo, Large anomalous Hall effect in a non-collinear antiferromagnet at room temperature. *Nature* **527**, 212 (2015).

[26] A. K. Nayak, J. E. Fischer, Y. Sun, B. Yan, J. Karel, A. C. Komarek, C. Shekhar, N. Kumar, W. Schnelle, J. Kübler, C. Felser, and S. P. P. Parkin, Large anomalous Hall effect driven by a nonvanishing Berry curvature in the noncollinear antiferromagnet Mn_3Ge. *Sci. Adv.* **2**, e1501870 (2016).

[27] Y. Zhang, Y. Sun, H. Yang, J. Železný, S. P. P. Parkin, C. Felser, and B. Yan, Strong anisotropic anomalous Hall effect and spin Hall effect in the chiral

antiferromagnetic compounds Mn_3X (X = Ge, Sn, Ga, Ir, Rh, and Pt). *Phys. Rev. B* **95**, 075128 (2017).

[28] N. Kiyohara, T. Tomita, and S. Nakatsuji, Giant Anomalous Hall Effect in the Chiral Antiferromagnet Mn_3Ge. *Phys. Rev. Applied* **5**, 064009 (2016).

[29] G. Gurung, D.-F. Shao, T. R. Paudel, and E. Y. Tsymbal, Anomalous Hall conductivity of non-collinear magnetic antiperovskites. *Phys. Rev. Mater.* **3**, 044409 (2019).

[30] D. Boldrin, I. Samathrakis, J. Zemen, A. Mihai, B. Zou, B. Esser, D. McComb, P. Petrov, H. Zhang, and L. F. Cohen, The anomalous Hall effect in non-collinear antiferromagnetic Mn_3NiN thin films. *Phys. Rev. Mater.* **3**, 094409 (2019).

[31] X. Zhou, J. -P. Hanke, W. Feng, F. Li, G.-Y. Guo, Y. Yao, S. Blügel, and Y. Mokrousov, Spin-order dependent anomalous Hall effect and magneto-optical effect in the noncollinear antiferromagnets Mn_3XN with X = Ga, Zn, Ag, or Ni. *Phys. Rev. B* **99**, 104428 (2019).

[32] There are several Néel vectors describing an AFM order in noncollinear antiferromagnets. Switching of the antiferromagnet implies reversal of all of them. Below we refer to this process as "AFM order switching."

[33] H. V. Gomonay, and V. M. Loktev, Spin transfer and current-induced switching in antiferromagnets, *Phys. Rev. B* **81**, 144427 (2010).

[34] H. Fujita, Field-free, spin-current control of magnetization in non-collinear chiral antiferromagnets. *Phys. Stat. Sol. (RRL)* **11**, 1600360 (2017).

[35] Y. Yamane, O. Gomonay, and J. Sinova, Dynamics of noncollinear antiferromagnetic textures driven by spin current injection. *Phys. Rev. B* **100**, 054415 (2019).

[36] T. Kaneko, T. Kanomata, and K. Shirakawa, Pressure effect on the magnetic transition temperatures in the intermetallic compounds Mn_3MC (M = Ga, Zn and Sn). *J. Phys. Soc. Jap.* **56**, 4047 (1987).

[37] K. Takenaka, M. Ichigo, T. Hamada, A. Ozawa, T. Shibayama, T. Inagaki, and K. Asano, Magnetovolume effects in manganese nitrides with antiperovskite structure. *Sci. Tech. Adv. Mat.* **15**, 015009 (2014).

[38] T. Tohei, H. Wada, and T. Kanomata, Negative magnetocaloric effect at the antiferromagnetic to ferromagnetic transition of Mn_3GaC. *J. Appl. Phys.* **94**, 1800 (2003).

[39] B. S. Wang, P. Tong, Y. P. Sun, X. Luo, X. B. Zhu, G. Li, X. D. Zhu, S. B. Zhang, Z. R. Yang, and W. H. Song, Large magnetic entropy change near room temperature in antiperovskite $SnCMn_3$. *EPL* **85**. 47004 (2009).

[40] P. Lukashev, R. F. Sabirianov, and K. Belashchenko, Theory of piezomagnetic effect in Mn-based antiperovskites. *Phys. Rev. B* **78**, 184414 (2008).

[41] J. Zemen, Z. Gercsi, and K. G. Sandeman, Piezomagnetism as a counterpart of the magnetovolume effect in magnetically frustrated Mn-based antiperovskite nitrides. *Phys. Rev. B* **96**, 024451 (2017).

[42] D. Boldrin, A. P. Mihai, B. Zou, J. Zemen, R. Thompson, E. Ware, B. V. Neamtu, L. Ghivelder, B. Esser, D. W. McComb, P. Petrov, and L. F. Cohen, Giant piezomagnetism in Mn_3NiN. *ACS Appl. Mater. & Int.* **10**, 18863 (2018).

[43] P. Lukashev, K. D. Belashchenko, R. F. Sabirianov, Large magnetoelectric effect in ferroelectric/piezomagnetic heterostructures. *Phys. Rev. B* **84**, 133420 (2011).

[44] D. F. Shao, G. Gurung. T. R. Paudel, and E. Y. Tsymbal, Electrically reversible magnetization at the antiperovskite/perovskite interface. *Phys. Rev. Mater.* **3**, 024405 (2019).

[45] X. Zhou, J. P. Hanke, W. Feng, F. Li, G. Y. Guo. Y. Yao, S. Blugel, and Y. Mokrousov, Spin-order dependent anomalous Hall effect and magneto-optical effect in the noncollinear antiferromagnets Mn_3XN with X = Ga, Zn, Ag or Ni. *Phys. Rev. B* **99**, 104428 (2019)

[46] K. Zhao, T. Hajiri, H, Chen, R. Miki, H. Asano, and P. Gegenwart, Anomalous Hall effect in the noncollinear antiferromagnetic antiperovskite $Mn_3Ni_{1-x}Cu_xN$. *Phys. Rev. B* **100**, 045109 (2019).

[47] D. Boldrin, I. Samathrakis, J. Zemen, A. Mihai, B. Zou, F. Johnson, B. D. Esser, D. W. McComb, P. K. Petrov, H. Zhang, and L. F. Cohen, Anomalous Hall effect in noncollinear antiferromagnetic Mn_3NiN thin films. *Phys. Rev. Mater.* **3**, 094409 (2019).

[48] V. T. N. Huyen, M. T. Suzuki, K, Yamauchi, and T. Oguchi, Topology analysis for anomalous Hall effect in the noncollinear antiferromagnetic states of Mn_3AN (A = Ni, Cu, Zn, Ga, Ge, Pd, In, Sn, Ir, Pt). *Phys. Rev. B* **100**, 094426 (2019).

[49] J. C. Slonczewski, Current-driven excitation of magnetic multilayers. *J. Magn. Magn. Matter* **159**, L1 (1996).

[50] Z. Li and S. Zhang, Magnetization dynamics with a spin-transfer torque. *Phys. Rev. B* **68**, 024404 (2003).

[51] S. Zhang, P. M. Levy, and A. Fert, Mechanisms of spin-polarized current-driven magnetization switching. *Phys. Rev. Lett.* **88**, 236601 (2002).

[52] G. Kresse and D. Joubert, Fully unconstrained noncollinear magnetism within the projector augmented-wave method. *Phys. Rev. B* **59**, 1758 (1999).

[53] P. Giannozzi, S. Baroni, N. Bonini, M. Calandra, R. Car, C. Cavazzoni, D. Ceresoli, G. L. Chiarotti, M. Cococcioni, I. Dabo, A. D. Corso, S. d. Gironcoli, S. Fabris, G. Fratesi, R. Gebauer, U. Gerstmann, C. Gougoussis, A. Kokalj, M. Lazzeri, L. M. Samos, N. Marzari, F. Mauri, R. Mazzarello, S. Paolini, A. Pasquarello, L. Paulatto, C. Sbraccia, S. Scandolo, G. Sclauzero, A. P. Seitsonen, A. Smogunov, P. Umari, and R. M. Wentzcovitch, Quantum ESPRESSO: A modular and open-source software project for quantum simulations of materials. *J. Phys.: Condens. Matt.* **21**, 395502 (2009).

[54] P. E. Blöchl, Projected augmented-wave method. *Phys. Rev. B* **50**, 17953 (1994).

[55] D. Vanderbilt, Soft self-consistent pseudopotentials in a generalized eigenvalue formalism. *Phys. Rev. B* **41**, 7892 (1990).

[56] J. P. Perdew, K. Burke, and M. Ernzerhof, Generalized gradient approximation made simple. *Phys. Rev. Lett.* **77**, 3865 (1996).

[57] H. Rosner, R. Weht, M. D. Johannes, W. E. Pickett, and E. Tosatti, Superconductivity near ferromagnetism in $MgCNi_3$. Phys. Rev. Lett. 88, 027001 (2001)

[58] R. F. L. Evans, W. J. Fan, P. Chureemart, T. A. Ostler, M. A. Ellis and R. W. Chantrell, Atomistic spin model simulations of magnetic nanomaterials. *J. Phys.: Condens. Matter* **26**, 103202 (2014).

[59] M. B. Nardelli, F. T. Cerasoli, M. Costa, S. Curtarolo, R. De Gennaro, M. Fornari, L. Liyanage, A. Supka, and H. Wang, PAOFLOW: A utility to construct and operate on *ab-initio* Hamiltonians from the projections of electronic wavefunctions on atomic orbital bases, including characterization of topological materials. *Comp. Mat. Sci.* **143**, 462 (2017).

[60] L. A. Agapito, A. Ferretti, A. Calzolari, S. Curtarolo, and M. B. Nardelli, Effective and accurate representation of extended Bloch states on finite Hilbert spaces. *Phys. Rev. B* **88**, 165127 (2013).

[61] L. A. Agapito, S. Ismail-Beigi, S. Curtarolo, M. Fornari, and M. B. Nardelli, Accurate tight-binding Hamiltonian matrices from *ab-initio* calculations: Minimal basis sets. *Phys. Rev. B* **93**, 035104 (2016).

[62] J. R. Yates, X. Wang, D. Vanderbilt, and I. Souza, Spectral and Fermi surface properties from Wannier interpolation. *Phys. Rev. B* **75**, 195121 (2007).

[63] H. J. Xiang, E. J. Kan, S. H. Wei, M.-H. Whagngbo, and X. G. Gong, Predicting the spin-lattice order of frustrated systems from first principles. *Phys. Rev. B* **84**, 224429 (2011).

[64] T. Schwarze, J. Waizner, M. Garst, A. Bauer, I. Stasinopoulos, H. Berger, C. Pfleiderer, and D. Grundler, Universal helimagnon and skyrmion excitations in metallic, semiconducting, and insulating chiral magnets. *Nat. Mater.* **14**, 478 (2015).

[65] M. Beg, M. Albert, M.-A. Bisotti, D. Cortés-Ortuño, W. Wang, R. Carey, M. Vousden, O. Hovorka, C. Ciccarelli, C. S. Spencer, C. H. Marrows, and H. Fangohr, Dynamics of skyrmionic states in confined helimagnetic nanostructures. *Phys. Rev. B* **95**, 014433 (2017).

[66] B. Ferguson, and X. Zhang, Materials for terahertz science and technology. *Nat. Mater.* **1**, 26 (2002).

[67] M. Tonouchi, Cutting-edge terahertz technology. *Nat. Photon.* **1**, 97 (2007).

[68] R. Kleiner, Filling the terahertz gap. *Science* **318**, 1254 (2007).

[69] O. V. Gomonay and V. M. Loktev, Using generalized Landau-Lifshitz equations to describe the dynamics of multi-sublattice antiferromagnets induced by spin-polarized current. *Low Temp. Phys.* **41**, 698 (2015).

[70] M. Gradhand, D. V. Fedorov, F. Pientka, P. Zahn, I. Mertig, and B. K. Györffy, First-principle calculations of the Berry curvature of Bloch states for charge and spin transport of electrons. *J. Phys.: Condens. Matt.* **24**, 213202 (2012).

[71] M. V. Berry, Quantal phase factors accompanying adiabatic changes. *Proc. R. Soc. A* **392**, 45 (1984).

[72] M. P. Ghimire J. I. Facio, J.-S. You, L. Ye, J. G. Checkelsky, S. Fang, E. Kaxiras, M. Richter, and J. van den Brink., Creating Weyl nodes and controlling their energy by magnetization rotation. *Phys. Rev. Res.* **1**, 032044(R) (2019).

[73] T. Hajiri, S. Ishino, K. Matsuura, and H. Asano, Electrical current switching of the noncollinear antiferromagnet Mn_3GaN. *Appl. Phys. Lett.* **115**, 052403 (2019).

Chapter 5 Spin Polarization in Noncollinear Antiferromagnets

As mentioned earlier, spintronics exploits the spin degree of freedom in electronic devices for information processing and storage [1]. The magnetic order parameter is used as the state variable in these devices, and its detection and manipulation manifest the read and write operations of the stored information. Currents with sizable spin polarization play a central role in the electric performance of such operations used in realistic nanoscale spintronic devices. For example, in magnetic tunnel junctions (MTJs), which are employed in commercial magnetic random-access memories (MRAMs) [2], the electrical detection is realized via the tunnelling magnetoresistance (TMR) effect signifying a response of the longitudinal spin-polarized charge current to the relative magnetization orientation of the two ferromagnetic electrodes [3- 5]. On the other hand, the electric manipulation of magnetization can be achieved via a spin transfer torque driven by a longitudinal spin-polarized charge current [6, 7] or via a spin Hall effect [8- 10] where a transverse pure spin current is generated by spin-orbit coupling. Generally, in the case of the heavy nonmagnetic metals, charge currents flowing along the in-plane direction generate out-of-plane spin currents that have spin polarization $\vec{p}$ perpendicular to the charge current direction and spin current direction. This spin current with spin polarization $\vec{p}$ generated due to the conventional spin Hall effect (SHE) exerts an anti-damping spin torque $\vec{m} \times \vec{m} \times \vec{p}$ in the adjacent ferromagnet with magnetization $\vec{m}$. This type of torque can only manipulate magnetization which lies along an in-plane direction. But the ferromagnet with out-of-plane magnetization is favoured over the in-plane magnetization for the development of the high-density memory spintronic devices. The conditions for the spin polarization to be along the spin current directions will be required

for out-of-plane magnetization manipulations. Such process will be defined as unconventional properties from now onwards.

Ferromagnetic metals have been widely used in spintronics due to their finite magnetization which can easily spin-polarize electric currents. More recently, it was argued that antiferromagnetic spintronics is more promising, due to antiferromagnets being robust against magnetic perturbations, producing no stray fields, and exhibiting ultrafast spin dynamics [11- 13]. Nevertheless, until recently antiferromagnets have been rarely considered efficient to generate spin-polarized currents. This is because most antiferromagnets exhibit a combined $\hat{T}\hat{O}$ symmetry, where $\hat{T}$ is the time reversal symmetry and $\hat{O}$ is a crystal symmetry (translation symmetry and Inversion symmetry). The $\hat{T}\hat{O}$ symmetry enforces Kramers' spin degeneracy and hence vanishing magnetization. While the antiferromagnetic order may lower the symmetry to support some unconventional spin Hall current useful for spin-orbit torque devices [14], the efficiency of the intrinsic charge-to-spin conversion of antiferromagnets [14- 16] do not show obvious advantages compared to those of the widely used nonmagnetic heavy metal spin sources [15- 17].

Recently, it was found that the $\hat{T}\hat{O}$ symmetry in antiferromagnets can be broken by the noncollinear magnetic order [18] or non-centrosymmetric arrangement of nonmagnetic atoms [19]. The broken $\hat{T}\hat{O}$ symmetry was shown to result in interesting electronic, magnetic and transport properties that previously were only known for ferromagnets, such as the anomalous Hall effect [26- 34], the non-relativistic Zeeman-like band splitting [35- 37], and the unconventional charge-to-spin conversion [38- 43]. In Table 3.2, the $\hat{T}\hat{M}$ symmetry does not enforce Kramers' spin degeneracy and

hence, allows the finiteness of the anomalous Hall effect. The emergence of electric currents with sizable spin polarization is particularly exciting, due to the possible use of these currents and the antiferromagnets generating them in spintronic devices [46, 44, 45].

In the diffusive transport regime, the spin conductivity has two contributions: [8, 46]

$$\sigma_{ij}^{k} = -\frac{e\hbar}{\pi}\int \frac{d^3\vec{k}}{(2\pi)^3}\sum_{n,m}\frac{\Gamma^2 \mathrm{Re}\left(\langle n\vec{k}|J_i^k|m\vec{k}\rangle\langle m\vec{k}|v_j|n\vec{k}\rangle\right)}{\left[\left(E_F - E_{n\vec{k}}\right)^2 + \Gamma^2\right]\left[\left(E_F - E_{m\vec{k}}\right)^2 + \Gamma^2\right]}, \tag{5.1}$$

and

$$\sigma_{ij}^{k} = -\frac{2e}{\hbar}\int \frac{d^3\vec{k}}{(2\pi)^3}\sum_{m\neq n}\frac{\mathrm{Im}\left(\langle n\vec{k}|J_i^k|m\vec{k}\rangle\langle m\vec{k}|v_j|n\vec{k}\rangle\right)}{\left(E_{n\vec{k}} - E_{m\vec{k}}\right)^2}. \tag{5.2}$$

Here $J_i^k = \frac{1}{2}\{v_i, s_k\}$ is the spin current operator, Γ is the scattering rate in a constant relaxation time approximation, $f_{n\vec{k}}$ is the Fermi-Dirac distribution function for band n and wave vector $\vec{k}$, v_i and s_k are velocity and spin operators, respectively, and i, j and k are the spin-current, charge-current, and spin polarization directions, respectively. The spin conductivity σ_{ij}^k given by Eq. (5.1) is the Fermi surface property odd under time reversal symmetry ($\hat{T}$-odd). As a result, this contribution is allowed only for ferromagnetic and some antiferromagnetic metals without $\hat{T}$ or $\hat{T}\hat{O}$ symmetries, such as noncollinear antiferromagnet ANMn$_3$. In these materials, the Fermi surface is intrinsically spin textured resulting in spin-polarized currents even in the absence of spin-orbit coupling. This leads to finite non-relativistic components of the $\hat{T}$-odd spin conductivity

tensor. Spin-orbit coupling alters the spin texture and hence the spin conductivity tensor. In contrast to the $\hat{T}$-odd σ_{ij}^{k} , the spin conductivity tensor given by Eq. (5.2) is determined by the interband contributions that are even under time reversal symmetry ($\hat{T}$-even). As a result, non-vanishing $\hat{T}$-even σ_{ij}^{k} components can only appear in the presence of spin-orbit coupling. Therefore, these relativistic components are expected to be small compared to the non-relativistic components of the $\hat{T}$-odd σ_{ij}^{k}.

Here, we explore spin polarization of Mn-based antiperovskite nitrides ANMn$_3$ (A = Ga, Ni, Sn, and Pt) [47]. The electronic structure of ANMn$_3$ [see Fig. 3.3] at the Fermi energy (E_F) being majorly controlled by the Mn atoms which do not produce strong spin-orbit coupling, spin conductivities are not expected to be significant (Note though that the spin-orbit coupling makes some σ_{ij}^{k} components finite, which were zero in its absence). We find that the spin Hall effect in the noncollinear antiferromagnet GaNMn$_3$ allow generation of spin current with different spin polarization (even parallel to the spin current or charge current direction). This unconventional spin Hall effect leads to unconventional spin-torques. The theoretical calculations support the experimental findings. We also found out that the longitudinal charge currents passing through ANMn$_3$ can have a sizable spin polarization, which allows using antiperovskites in magnetic tunnel junctions and spin transfer torque devices. Moreover, we show that the out-of-plane transverse spin currents with giant charge-to-spin conversion efficiencies can be achieved by controlling the film growth direction. These properties make ANMn$_3$ compounds promising for application in spintronics.

5.1. Calculation Methods

DFT calculations were performed using a Quantum-ESPRESSO code [48]. The plane-wave pseudopotential method with the fully relativistic ultrasoft pseudopotentials [49] was employed in the calculations. The exchange and correlation effects were treated within the generalized gradient approximation (GGA) [50]. The *k*-point mesh of 16×16×16 and plane-wave cut-off energy of 52 Ry were used for the integration in the irreducible Brillouin zone. Spin-orbit coupling was included in all the calculations. Charge and spin conductivities were calculated using a Wannier linear response code [51] based on the tight-binding Hamiltonian utilizing the maximally localized Wannier functions [52] obtained using a Wannier90 code [53]. Symmetry of the spin conductivity tensors was obtained using a linear response symmetry code [54]. The integration in equations (1) and (2) in the main text was performed using a $200 \times 200 \times 200$ k-point mesh. Even spin Hall conductivities in the Table 5.1 and Fig. 5.1(d) were calculated by constructing the tight-binding Hamiltonians using PAOFLOW code [55] based on the projection of the pseudo-atomic orbitals (PAO) [56, 57] from the non-self-consistent calculations with a $16 \times 16 \times 16$ *k*-point mesh. In this case, we use the tight-binding Hamiltonians with a $48 \times 48 \times 48$ *k*-point mesh by the adaptive broadening method to get the converged values.

The figures were created using VESTA [58], Matplotlib, and Fermi Surfer [59]. We also present the experimental work done by our collaborator at University of Wisconsin-Madisson. The experimental work was carried out by epitaxial $GaNMn_3$ thin films on (001)-oriented LSAT substrates. Spin torque-ferromagnetic resonance (ST-

FMR) measurements were done to extract the spin torque. Further experimental methods can be found in the reference 14.

5.2. Unconventional Spin Torque

Antiperovskite $GaNMn_3$ transforms from the ground state noncollinear antiferromagnetic Γ_{5g} phase to paramagnetic phase on passing through the Néel temperature ($T_N \sim 350K$). The paramagnetic phase has higher symmetry with space group group $Pm\bar{3}m$ only allows the conventional components in spin-Hall conductivity tensors [60]. But below the Néel temperature, $GaNMn_3$ exhibit antiferromagnetic ordering with a noncollinear Γ_{5g} Kagome-like structure (magnetic space group: $R\bar{3}m$) stabilized by the magnetic frustration of the Mn atoms in the (111) plane. Figure 5.1 (b) and (e) shows the $GaNMn_3$ (001) plane with and without noncollinear spins respectively. The blue dotted lines show the available mirror symmetry which commutes with the respective Hamiltonian. Noncollinear Γ_{5g} phase of $GaNMn_3$(001) thin film has only one (110) mirror plane and hence, the restriction on the spin Hall tensors is hugely reduced compared to the nonmagnetic phase. Only the conventional components (with mutually perpendicular current, spin current and spin polarization direction) is allowed in the paramagnetic phase due to the cancellation of other components of total Berry curvature upon imposing the preserved symmetry operations [see Fig. 5.1 (f), four mirror planes in the crystal plane]. Three of these mirror planes symmetries are broken in Γ_{5g} phase (only (110) mirror plane symmetry allowed) and hence, the cancellation of the Berry curvature does not occur leading to finite unconventional components [see Fig. 5.1 (d) and (f)]. The experimental and theoretical work finds that on application of the charge currents along x generate transverse spin current along z with usual conventional spin polarization along y and in

addition, unconventional spin polarization along x and z. Hence, in Fig. 5.1 (d), we have finite even spin Hall conductivities σ_{zx}^{x}, σ_{zx}^{y} and σ_{zx}^{z} (σ_{jk}^{i} where i, j and k corresponds to spin polarization, spin flow and charge flow directions). This symmetry allowed components correspond to the anti-damping torque components in the form of $\vec{\tau}_p \propto \vec{m} \times \vec{m} \times \vec{p}$ with finite unconventional term with spin polarization $\vec{p} = x, z$ and conventional term with $\vec{p} = y$. Figure 5.1(d) shows that the σ_{zx}^{x}, σ_{zx}^{y} and σ_{zx}^{z} components calculated theoretically for the bulk $GaNMn_3$ is finite and large within a wide energy window around the fermi level which implies the existence of a sizable even spin Hall current even in the presence of charge carrier doping by defects. The even spin Hall conductivity tensors obtained from symmetry analysis and calculations for Γ_{5g} and paramagnetic phases are shown in Table 5.1.

Experimental collaborators measure the symmetry of the spin torques using the ST-FMR [61, 62] in Py/$GaNMn_3$ interface. The torque components were found quantitatively by performing ST-FMR measurements as a function of the in-plane magnetic field angle. They found non-zero anti-damping torque terms $\vec{\tau}_{x,y,z}$ with unconventional torque due to the spin polarizations along x and z. Angular-dependent ST-FMR measurements across antiferromagnetic-to-paramagnetic phase transition shows that the noncollinear spin structure in $GaNMn_3$ is correlated with the unconventional spin polarization [see Fig. 5.2 (b)-(d)]. Figure 5.2 shows the temperature dependence (300 K to 380 K) of the ratios between anti-damping torque components and the Oersted torque,

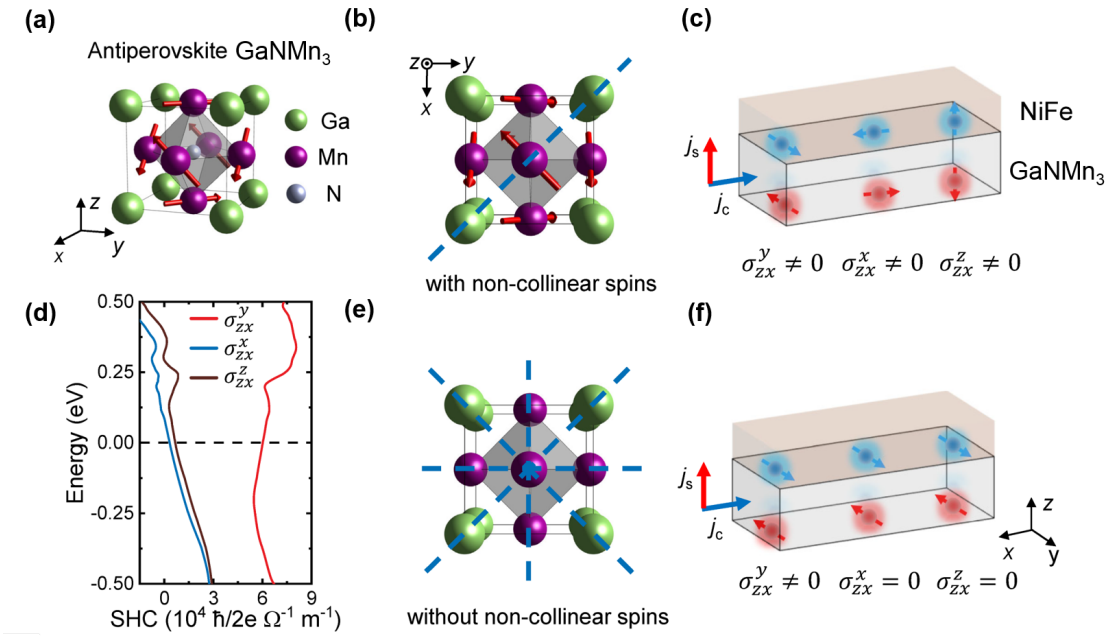

Figure 5.1. The concept of the unconventional spin-Hall effect in $GaNMn_3$. (a) The crystallographic unit cell of antiperovskite $GaNMn_3$ with the AFM Γ_{5g} spin structure where Mn spins (arrows) form a Kagome-type lattice in the (111) plane. The *x*, *y*, and *z* correspond to the cubic [100], [010], and [001] axis, respectively. (b) Spin structure of $GaNMn_3$ in the (001) plane. The blue dashed line corresponds to the (110) mirror plane. (**c**) Schematic illustrations of the Py/$GaNMn_3$ bilayer and the allowed spin-Hall spin polarization in the low-symmetry state (a). This indicates non-zero spin-Hall conductivities σ_{zx}^{y}, σ_{zx}^{x} and σ_{zx}^{z}, which correspond to spin polarizations along *y*, *x* and *z* direction, respectively (with the charge current along *x* and spin current along *z*). (d) Calculated spin-Hall conductivities σ_{zx}^{y}, σ_{zx}^{x} and σ_{zx}^{z} for $GaNMn_3$ as a function of Fermi energy. (e) Crystal structure of $GaNMn_3$ without non-collinear spin structure (*i.e.*, above the Neel temperature T_N) in the (001) plane, which gives rise to a high-symmetry state. (f) Allowed spin polarization in the high-symmetry state, where only the conventional spin-Hall conductivity σ_{zx}^{y} is non-zero.

Table 5.1. The theoretical and calculated even spin Hall conductivity tensor for Γ_{5g} phase and paramagnetic phase $GaNMn_3$.

		σ^x	σ^y	σ^z
Γ_{5g}	Tensor shape	$\begin{bmatrix} 0 & -\sigma_{yx}^{y} & \sigma_{yx}^{y} \\ \sigma_{yx}^{x} & -\sigma_{xx}^{y} & -\sigma_{yx}^{z} \\ -\sigma_{yx}^{x} & \sigma_{yx}^{z} & \sigma_{xx}^{y} \end{bmatrix}$	$\begin{bmatrix} \sigma_{xx}^{y} & -\sigma_{yx}^{x} & \sigma_{yx}^{z} \\ \sigma_{yx}^{y} & 0 & -\sigma_{yx}^{y} \\ -\sigma_{yx}^{z} & \sigma_{yx}^{x} & -\sigma_{xx}^{y} \end{bmatrix}$	$\begin{bmatrix} -\sigma_{xx}^{y} & -\sigma_{yx}^{z} & \sigma_{yx}^{x} \\ \sigma_{yx}^{z} & \sigma_{xx}^{y} & -\sigma_{yx}^{x} \\ -\sigma_{yx}^{y} & \sigma_{yx}^{y} & 0 \end{bmatrix}$
	Calculated tensor	$\begin{bmatrix} 0 & 45 & -45 \\ -29 & 40 & 114 \\ 29 & -114 & -40 \end{bmatrix}$	$\begin{bmatrix} -40 & 29 & -114 \\ -45 & 0 & 45 \\ 114 & -29 & 40 \end{bmatrix}$	$\begin{bmatrix} 40 & 114 & -29 \\ -114 & -40 & 29 \\ 45 & -45 & 0 \end{bmatrix}$
Paramagnetic	Tensor shape	$\begin{bmatrix} 0 & 0 & 0 \\ 0 & 0 & -\sigma_{yx}^{z} \\ 0 & \sigma_{yx}^{z} & 0 \end{bmatrix}$	$\begin{bmatrix} 0 & 0 & \sigma_{yx}^{z} \\ 0 & 0 & 0 \\ -\sigma_{yx}^{z} & 0 & 0 \end{bmatrix}$	$\begin{bmatrix} 0 & -\sigma_{yx}^{z} & 0 \\ \sigma_{yx}^{z} & 0 & 0 \\ 0 & 0 & 0 \end{bmatrix}$
	Calculated tensor	$\begin{bmatrix} 0 & 0 & 0 \\ 0 & 0 & 41 \\ 0 & -41 & 0 \end{bmatrix}$	$\begin{bmatrix} 0 & 0 & -41 \\ 0 & 0 & 0 \\ 41 & 0 & 0 \end{bmatrix}$	$\begin{bmatrix} 0 & 41 & 0 \\ -41 & 0 & 0 \\ 0 & 0 & 0 \end{bmatrix}$

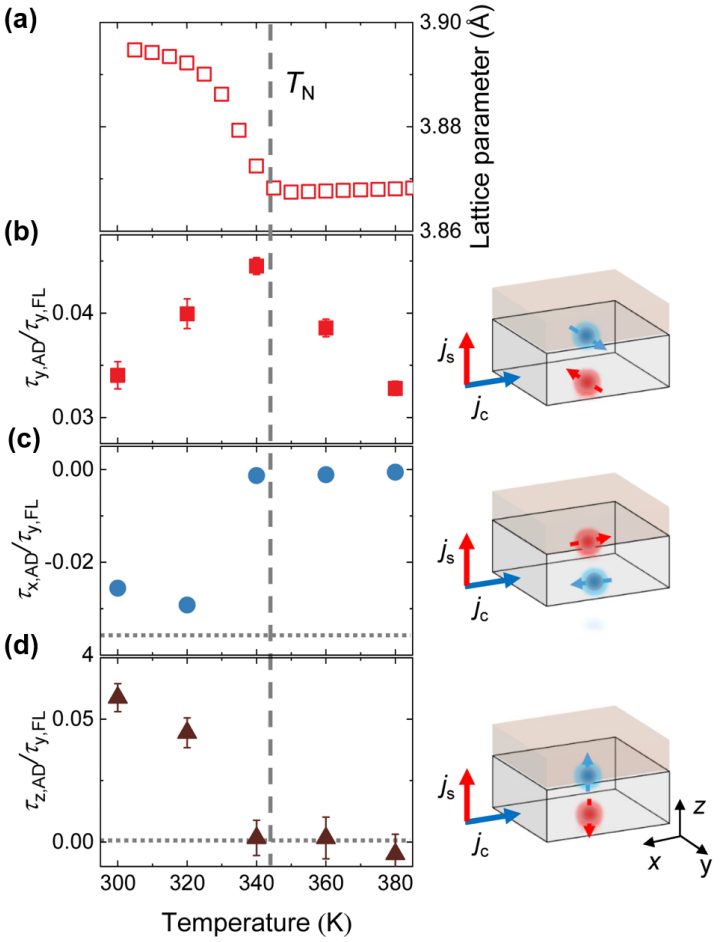

Figure 5.2. Temperature dependence of spin-orbit torques. (a) Out-of-plane lattice parameter of a 30 nm $GaNMn_3$/LSAT sample as a function of temperature, where the decrease of the lattice parameter indicates the $GaNMn_3$ Néel temperature T_N of ~345 K. (b)-(d) The torque ratios $\tau_{y,AD}/\tau_{y,FL}$, $\tau_{x,AD}/\tau_{y,FL}$ and $\tau_{z,AD}/\tau_{y,FL}$ as a function of the temperature. The schematic on the right panel shows the geometry of the spin-Hall effect with different spin polarizations.

$\tau_{y,AD}/\tau_{y,FL}$, $\tau_{x,AD}/\tau_{y,FL}$and $\tau_{z,AD}/\tau_{y,FL}$ (extracted from the full angular dependent ST-FMR measured at each temperature). All three torque ratios drastically reduce at the Néel temperature of $GaNMn_3$. In particular, the unconventional torque ratios $\tau_{x,AD}/\tau_{y,FL}$and

$\tau_{z,AD}/\tau_{y,FL}$ vanish when the sample temperature is above the Néel temperature. This directly demonstrate the strong correlation between the non-collinear spin structure and the existence of unconventional spin torque.

5.3. Spin Polarized Current

In addition to the Γ_{5g} magnetic phase (ground state of $GaNMn_3$) considered in Section 5.2; we take into consideration Γ_{4g} magnetic phases for different antiperovksite $ANMn_3$. Γ_{5g} is a compensated antiferromagnetic phase due to three mirror planes $\widehat{M}_{0\bar{1}1}$, $\widehat{M}_{10\bar{1}}$, or $\widehat{M}_{\bar{1}10}$ perpendicular to the (111) plane in the magnetic space group $R\bar{3}m$ which prohibit the net magnetization [see Fig. 3.2 (a)]. Another common noncollinear antiferromagnetic phase is Γ_{4g}, which can be obtained from the Γ_{5g} phase by rotating all magnetic moments about the [111] axis by 90° [Fig. 3.2(b)]. The mirror symmetries are broken in the Γ_{4g} phase so that the corresponding magnetic space group $R\bar{3}m'$ allows an uncompensated magnetization (though very small) and the anomalous Hall effect as observed in Chapter 3.

We find that the magnetic group symmetries of both Γ_{5g} and Γ_{4g} phases support sizable longitudinal and transverse spin currents. Table 5.3 displays the $\hat{T}$-odd σ_{ij}^{k} of $A\mathrm{NMn_3}$ according to the magnetic space group symmetry of the crystal. For a (001)-stacked $ANMn_3$ with the *x*, *y*, and *z* axes aligned along the [100], [010], and [001] crystal directions, there are four independent tensor components (denoted by *a*, *b*, *c*, and *d*) in the Γ_{5g} phase. These include the off-diagonal tensor components σ_{ij}^{k} $(i \neq j)$ which determine the transverse spin current generated by a longitudinal charge current and are related to the magnetic spin Hall effect proposed recently [46-49]. However, these off-

diagonal components are relativistic in nature and are non-zero only in the presence of spin-orbit coupling. Therefore, these relativistic contributions to spin conductivity are not expected to be large, due to the weak spin-orbit coupling in ANMn$_3$.

There are also non-relativistic diagonal components of the spin conductivity tensor σ_{jj}^{k} $(k \neq j)$. These components determine a longitudinal spin current carrying a transverse spin polarization generated by a longitudinal charge current. These diagonal components are non-zero even in the absence of spin-orbit coupling and hence are expected to be large. This implies that a longitudinal spin-polarized charge current can be produced in the compensated antiferromagnetic Γ_{5g} phase.

In order to obtain a more intuitive understanding of why the longitudinal charge current is spin-polarized, we use GaNMn$_3$ as a representative example and explore its momentum-dependent spin texture. Due to the broken $\hat{T}$ symmetry in antiferromagnetic GaNMn$_3$, the spin degeneracy is lifted and hence the spin expectation values $\langle s \rangle$ are finite. Since the $\hat{T}$-odd spin conductivity is a purely Fermi surface property [see Eq. (5.1)], it is the spin texture at the Fermi surface that matters. Figure 5.3(a) shows the calculated expectation values of the x, y, and z components of the spin at the Fermi surface of GaNMn$_3$ in the Γ_{5g} phase, indicating a rather intricate distribution. The same spin texture, but within the (110) plane, is displayed in Figure 5.3(b) and enlarged in Figure 5.3(c) to focus on the Fermi pocket at the centre of the Brillouin zone. These spin textures can make the electric currents flowing along certain crystallographic directions of GaNMn$_3$ spin polarized.

To demonstrate this, we consider symmetry transformations of the spin texture within this Fermi pocket. The inversion-symmetric fragments of the Fermi pocket have the same spin expectation values, since the inversion symmetry $\hat{P}$ does not change the spin:

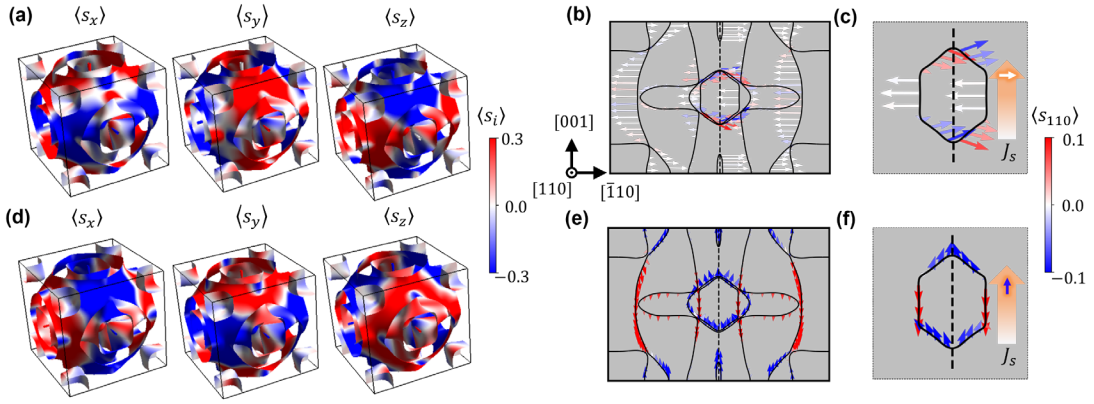

Figure 5.3. Spin texture of noncollinear antiferromagnetic phases. (a) The spin-projected Fermi surface of $GaNMn_3$ in the Γ_{5g} phase. (b) The (110) plane cut of the Fermi surfaces shown in (a), where the solid lines denote the Fermi surface, the colored arrows denote the spin textures, and the dashed line denote the $\hat{M}_{\bar{1}10}$ mirror plane. (c) The zoomed plot of (b) showing only the central Fermi pocket. (d,e,f) The same in (a,b,c) for $GaNMn_3$ in the Γ_{4g} phase.

$$\hat{P}(k_{110}, k_{\bar{1}10}, k_{001}) = (-k_{110}, -k_{\bar{1}10}, -k_{001}),$$

$$\hat{P}(\langle s_{110} \rangle, \langle s_{\bar{1}10} \rangle, \langle s_{001} \rangle) = (\langle s_{110} \rangle, \langle s_{\bar{1}10} \rangle, \langle s_{001} \rangle). \quad (5.3)$$

Further, the spin expectation values for the wave vectors being symmetric with respect to the $\hat{M}_{\bar{1}10}$ mirror plane have the same $\langle s_{\bar{1}10} \rangle$ components but opposite $\langle s_{001} \rangle$

and $\langle s_{110} \rangle$ components. This is due to the mirror symmetry operation conserving the spin component normal to the mirror plane but flipping the spin component parallel to it:

$$\widehat{M}_{\bar{1}10}(k_{110}, k_{\bar{1}10}, k_{001}) = (k_{110}, -k_{\bar{1}10}, k_{001}),$$

$$\widehat{M}_{\bar{1}10}(\langle s_{110} \rangle, \langle s_{\bar{1}10} \rangle, \langle s_{001} \rangle) = (-\langle s_{110} \rangle, \langle s_{\bar{1}10} \rangle, -\langle s_{001} \rangle). \quad (5.4)$$

As a result, the longitudinal electric current parallel to the $(\bar{1}10)$ plane, such as the current along the [001] direction shown in Fig. 5.3(c) is polarized by this spin texture. The associated spin current J_c has a finite $\langle s_{\bar{1}10} \rangle$ component but zero $\langle s_{110} \rangle$ and $\langle s_{001} \rangle$ components, since only $\langle s_{\bar{1}10} \rangle$ is even with respect to $\widehat{M}_{\bar{1}10}$. This implies finite matrix elements of the longitudinal spin conductivity tensor $\sigma_{zz}^{x} = -\sigma_{zz}^{y} = c$, as shown in Table 5.1 for *A*NMn$_3$ in the Γ_{5g} phase.

In contrast to the Γ_{5g} phase, the Γ_{4g} phase of *A*NMn$_3$ has five independent components (denoted by *A*, *B*, *C*, *D*, and *E*) of the $\hat{T}$-odd spin conductivity tensor for a (001)-stacked *A*NMn$_3$. We find that both the diagonal components with spin polarization normal to the charge current direction, $\sigma_{jj}^{k} = C$ $(k \neq j)$, and those parallel to it, $\sigma_{jj}^{j} = E$, do not vanish in the absence of spin-orbit coupling. This can be illustratively understood by analyzing the spin projected Fermi surfaces of the Γ_{4g} GaNMn$_3$ (Fig. 5.2(d-f)). The spin textures in the Γ_{4g} phase are very different from those in the Γ_{5g} phase due to different magnetic-space group symmetry. The mirror $\widehat{M}_{\bar{1}10}$ plane is broken in the Γ_{4g} phase, while a combined $\hat{T}\widehat{M}_{\bar{1}10}$ symmetry is preserved, which transforms the wave vector, and the spin as follows:

$$\hat{T}\widehat{M}_{\bar{1}10}(k_{110}, k_{\bar{1}10}, k_{001}) = (-k_{110}, k_{\bar{1}10}, -k_{001}),$$

$$\hat{T}\hat{M}_{\bar{1}10}(\langle s_{110}\rangle, \langle s_{\bar{1}10}\rangle, \langle s_{001}\rangle) = (\langle s_{110}\rangle, -\langle s_{\bar{1}10}\rangle, \langle s_{001}\rangle). \quad (5.5)$$

This symmetry together with inversion symmetry $\hat{P}$ (Eq. (3)) implies that $\langle s_{\bar{1}10}\rangle$ is antisymmetric and $\langle s_{110}\rangle$ and $\langle s_{001}\rangle$ are symmetric with respect to $(\bar{1}10)$ plane. Therefore, a longitudinal electric current parallel to the $(\bar{1}10)$ plane, such as that along the [001] direction, becomes spin-polarized with finite $\langle s_{110}\rangle$ and $\langle s_{001}\rangle$ components and a zero $\langle s_{\bar{1}10}\rangle$ component. This implies finite longitudinal spin conductivities $\sigma_{zz}^{x} = \sigma_{zz}^{y} = C$ and $\sigma_{zz}^{z} = E$ as shown in Table 5.2.

The efficiency of the $\hat{T}$-odd spin current generation can be estimated by calculating a percentage spin conductivity ratio $\Phi\left(\sigma_{ij}^{k}\right) = \frac{2e}{\hbar}\sigma_{ij}^{k}/\sigma_{jj}$. Here σ_{jj} is a conductivity of the longitudinal charge current J_c used to generate the spin current J_s with conductivity σ_{ij}^{k}, which can be calculated by replacing the spin current operator J_i^k in Eq. (5.1) by the charge current operator $J_i = -ev_i$. $\Phi\left(\sigma_{zj}^{k}\right)$ serves as a figure of merit for the performance of realistic spintronic devices. In particular, $\Phi(\sigma_{zx}^{k})$ represents the spin Hall angle in spin-torque devices with current-in-plane (CIP) geometry, where an out-of-plane spin current is generated by an in-plane charge current. Similarly, $\Phi(\sigma_{zz}^{k})$ measures the degree of spin polarization for an out-of-plane charge current in devices with current-perpendicular-to-plane (CPP) geometry, such as MTJs.

We calculate $\Phi\left(\sigma_{zj}^{k}\right)$ for ANMn$_3$ (A = Ga, Ni, Sn, Pt) compounds assuming they are stacked in the (001) plane. Table 5.2 shows the calculated results for $\Gamma = 0.05$ eV which provides realistic conductivity σ_{zz} of the compounds. For the longitudinal spin conductivity, we find that $\Phi\left(\sigma_{zz}^{i}\right)$ is sizable for all ANMn$_3$ antiferromagnets we

Table 5.2. $\hat{T}$-odd spin conductivity tensors for the Γ_{5g} and Γ_{4g} phases of $ANMn_3$. The *x*, *y*, and *z* axes are set along the [100], [010] and [001] directions for a (001)-stacked film and along the $[\bar{1}10]$, [001], and [110] directions for a (110)-stacked film. The matrix elements in the parentheses only appear in the presence of spin-orbit coupling.

		$\sigma^x = \begin{bmatrix} \sigma^x_{xx} & \sigma^x_{xy} & \sigma^x_{xz} \\ \sigma^x_{yx} & \sigma^x_{yy} & \sigma^x_{yz} \\ \sigma^x_{zx} & \sigma^x_{zy} & \sigma^x_{zz} \end{bmatrix}$	$\sigma^y = \begin{bmatrix} \sigma^y_{xx} & \sigma^y_{xy} & \sigma^y_{xz} \\ \sigma^y_{yx} & \sigma^y_{yy} & \sigma^y_{yz} \\ \sigma^y_{zx} & \sigma^y_{zy} & \sigma^y_{zz} \end{bmatrix}$	$\sigma^z = \begin{bmatrix} \sigma^z_{xx} & \sigma^z_{xy} & \sigma^z_{xz} \\ \sigma^z_{yx} & \sigma^z_{yy} & \sigma^z_{yz} \\ \sigma^z_{zx} & \sigma^z_{zy} & \sigma^z_{zz} \end{bmatrix}$
$ANMn_3$ (001)	Γ_{5g}	$\begin{bmatrix} 0 & (-a) & (a) \\ (b) & -c & (-d) \\ (-b) & (d) & c \end{bmatrix}$	$\begin{bmatrix} c & (-b) & (d) \\ (a) & 0 & (-a) \\ (-d) & (b) & -c \end{bmatrix}$	$\begin{bmatrix} -c & (-d) & (b) \\ (d) & c & (-b) \\ (-a) & (a) & 0 \end{bmatrix}$
	Γ_{4g}	$\begin{bmatrix} E & (A) & (A) \\ (B) & C & (D) \\ (B) & (D) & C \end{bmatrix}$	$\begin{bmatrix} C & (B) & (D) \\ (A) & E & (A) \\ (D) & (B) & C \end{bmatrix}$	$\begin{bmatrix} C & (D) & (B) \\ (D) & C & (B) \\ (A) & (A) & E \end{bmatrix}$
$ANMn_3$ (110)	Γ_{5g}	$\begin{bmatrix} \frac{-a+b+c}{\sqrt{2}} & 0 & 0 \\ 0 & -\sqrt{2}c & (b-d) \\ 0 & (-a+d) & \frac{a-b+c}{\sqrt{2}} \end{bmatrix}$	$\begin{bmatrix} 0 & (-\sqrt{2}b) & c+d \\ (\sqrt{2}a) & 0 & 0 \\ c-d & 0 & 0 \end{bmatrix}$	$\begin{bmatrix} 0 & (-a-d) & \frac{a+b-c}{\sqrt{2}} \\ (b+d) & 0 & 0 \\ \frac{-a+b+c}{\sqrt{2}} & 0 & 0 \end{bmatrix}$
	Γ_{4g}	$\begin{bmatrix} 0 & (A-D) & \frac{A-B-C+E}{\sqrt{2}} \\ (B-D) & 0 & 0 \\ \frac{-A+B-C+E}{\sqrt{2}} & 0 & 0 \end{bmatrix}$	$\begin{bmatrix} C-D & 0 & 0 \\ 0 & E & (\sqrt{2}\,A) \\ 0 & (\sqrt{2}\,B) & C+D \end{bmatrix}$	$\begin{bmatrix} \frac{-A-B+C+E}{\sqrt{2}} & 0 & 0 \\ 0 & \sqrt{2}C & (B+D) \\ 0 & (A+D) & \frac{A+B+C+E}{\sqrt{2}} \end{bmatrix}$

investigated. Especially, we obtain $\Phi(\sigma_{zz}^{x}) = -20.7\%$ for $GaNMn_3$ which exhibits a Γ_{5g} ground state, and $\Phi(\sigma_{zz}^{x}) = -16.0\%$ and $\Phi(\sigma_{zz}^{z}) = 31.2\%$ for $SnNMn_3$ which has a high temperature Γ_{4g} state. These sizable spin polarizations of the longitudinal current in antiferromagnetic antiperovskites are comparable to those in ferromagnetic metals, such as Fe, Co, and Ni [63- 65], indicating their potential for spintronic applications, such as antiferromagnetic tunnel junctions discussed below. We note that our results are robust with respect to disorder scattering, as follows from our calculations of $\Phi(\sigma_{zz}^{k})$ as a function of Γ shown in Fig. 5.4.

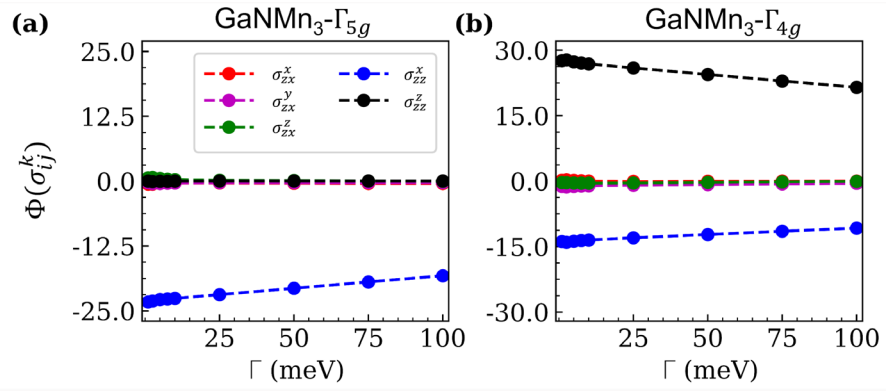

Figure 5.4. Charge-to-spin conversion efficiency $\Phi(\sigma_{ij}^{k})$ as a function of Γ for $GaNMn_3$ (a) Γ_{5g} and (b) Γ_{4g} phases.

Figure 5.4 shows the calculated charge-to-spin conversion efficiency of $GaNMn_3$ (001) as a function of Γ. It is seen that $\Phi(\sigma_{zj}^{k})$ does not change much with Γ. As expected, independent of Γ , the absolute values of $\Phi(\sigma_{zz}^{k})$ are significantly larger than those for $\Phi(\sigma_{zx}^{k})$, due to $\Phi(\sigma_{zz}^{k})$ being majorly contributed by the non-relativistic spin textures while $\Phi(\sigma_{zx}^{k})$ resulting from the weak spin-orbit coupling.

On the contrary, the transverse spin conductivity ratio $\Phi(\sigma_{zx}^{k})$ is negligible for *A*NMn$_3$ (001) [Table 5.2]. This is understandable since the non-relativistic spin texture does not contribute to σ_{zx}^{k} and the effect appears entirely due to small spin-orbit coupling. However, although *A*NMn$_3$ is not efficient for generating transverse spin currents in (001)-stacked films, it can form a good spin current source for spin-torque devices by engineering the *A*NMn$_3$ growth direction. The related spin conductivity tensors for a film with different orientation can be obtained by applying transformation

$$\sigma_{i'j'}^{k'} = \sum_{k,i,j} R_{k'k} R_{i'i} R_{j'j} \sigma_{ij}^{k}, \tag{5.6}$$

where σ_{ij}^{k} is the spin conductivity for a (001)-stacked film with coordinate system (x, y, z) , $\sigma_{i'j'}^{k'}$ is the spin conductivity of a film with coordinate system (x', y', z'), R is the rotation matrix to transform the coordinate system (x, y, z) to (x', y', z'). A non-relativistic spin texture contribution to $\Phi(\sigma_{zx}^{k})$ may be allowed by the magnetic-space group symmetry after the rotation transformation.

As an example, Table 5.2 shows the spin conductivity tensor for *A*NMn$_3$ (110) in the Γ_{5g} and Γ_{4g} phases. It is seen that when the charge current direction (*x*) is along the $[\bar{1}10]$ direction, finite σ_{zx}^{y} and σ_{zx}^{z} appear in the Γ_{5g} phase, and a finite σ_{zx}^{x} appear in the Γ_{4g} phase, even in the absence of spin-orbit coupling. Table 5.3 shows calculated $\Phi(\sigma_{zx}^{k})$ for *A*NMn$_3$ (*A* = Ga, Ni, Sn, and Pt) (110) films. For the Γ_{5g} ground state in GaNMn$_3$, we find large $\Phi(\sigma_{zx}^{y}) = -21.0\%$ and $\Phi(\sigma_{zx}^{z}) = 14.4\%$, which are comparable or even larger than these for the reported spin Hall angle in widely used spin source materials such as Pt [66- 68].Moreover, the transverse σ_{zx}^{x} component in the Γ_{5g} phase can be

Table 5.3. Charge-to-spin conversion efficiency $\Phi\left(\sigma_{ij}^{k}\right) = \frac{2e}{\hbar}\sigma_{ij}^{k}/\sigma_{jj}$ (in %) in antiperovskite $ANMn_3$ (A = Ga, Ni, Sn, Pt) in Γ_{5g} and Γ_{4g} phases for (001)- and (110)-stacked films. Calculations are performed in the presence of spin-orbit coupling for $\Gamma = 0.05$ eV. The *x*, *y*, and *z* are set along [100], [010] and [001] directions for (001)-stacked film and along $[\bar{1}10]$, [001], and [110] directions for a (110)-stacked film.

		$\boldsymbol{\Gamma_{5g}}$				$\boldsymbol{\Gamma_{4g}}$			
		$GaNMn_3$	$NiNMn_3$	$SnNMn_3$	$PtNMn_3$	$GaNMn_3$	$NiNMn_3$	$SnNMn_3$	$PtNMn_3$
ANMn$_3$ (001)	$\Phi(\sigma_{zz}^{x})$	−20.7	13.3	−27.0	14.2	−12.3	7.7	−16.0	10.2
	$\Phi(\sigma_{zz}^{z})$	0.0	0.0	0.0	0.0	24.4	−15.1	31.2	−18.1
	$\Phi(\sigma_{zx}^{x})$	−0.4	−0.7	−0.7	−3.4	−0.1	−0.3	0.6	−1.8
	$\Phi(\sigma_{zx}^{y})$	−0.3	−0.4	−0.6	−0.01	−0.8	−0.3	−0.4	−3.8
	$\Phi(\sigma_{zx}^{z})$	0.1	0.5	−0.1	1.0	−0.3	−0.2	0.3	−0.1
ANMn$_3$ (110)	$\Phi(\sigma_{zz}^{x})$	−15.0	8.6	−19.5	6.9	0.0	0.0	0.0	0.0
	$\Phi(\sigma_{zz}^{z})$	0.0	0.0	0.0	0.0	8.3	−5.6	11.4	−6.9
	$\Phi(\sigma_{zx}^{x})$	0.0	0.0	0.0	0.0	26.1	−16.2	33.6	−21.2
	$\Phi(\sigma_{zx}^{y})$	−21.0	12.9	−27.6	14.2	0.0	0.0	0.0	0.0
	$\Phi(\sigma_{zx}^{z})$	14.4	−9.5	18.5	−11.7	0.0	0.0	0.0	0.0

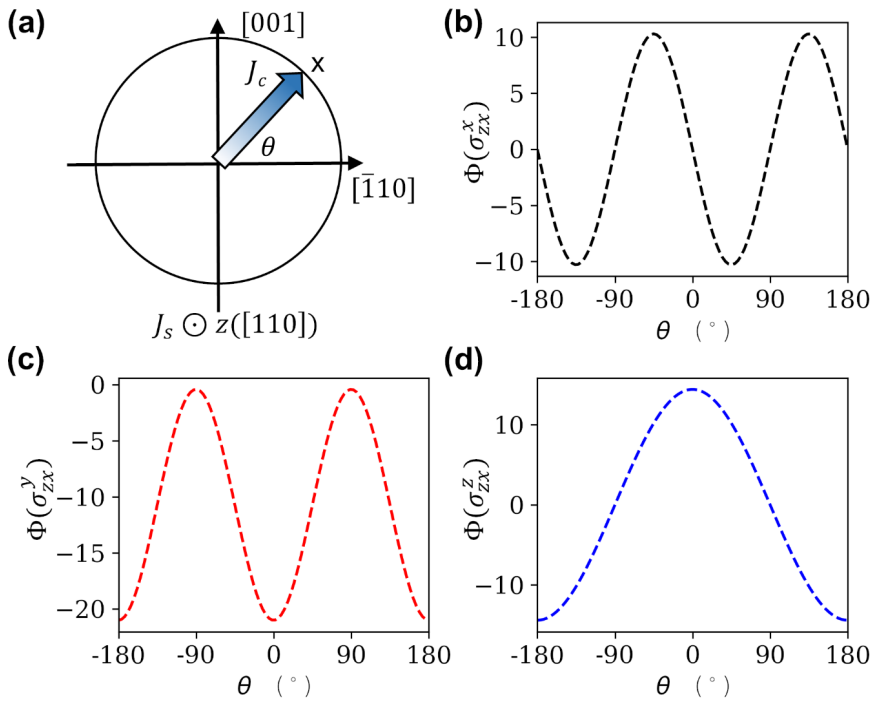

Figure 5.5. Effect of epitaxial growth direction of $ANMn_3$ thin film on spin conductivities. (a) The schematic of charge-to-spin conversion in an $ANMn_3$ (110) film. An out-of-plane spin current J_s along the [110] (z) direction is generated by applying an in-plane longitudinal charge current J_c along x direction which is away from [$\bar{1}$10] direction by the angle θ. (b, c, d) Charge-to-spin conversion efficiency $\Phi(\sigma_{zx}^k)$as a function of the longitudinal charge current direction for $GaNMn_3$ (110)-stacked films in the Γ_{5g} phase.

engineered by tilting the in-plane longitudinal current direction *x* from [110] by an angle θ [Fig. 5.5(a)]. In this case, the σ_{zx}^k components are functions of θ as follows:

$$\sigma_{zx}^x = \frac{-a+c}{2}\sin 2\theta\,,$$

$$\sigma_{zx}^y = \frac{1}{2}(a+c-2d) - \frac{1}{2}(a-c)\cos 2\theta\,,$$

$$\sigma_{zx}^{z} = -\frac{a+b+c}{\sqrt{2}}\cos\theta\,. \tag{5.7}$$

Figures 5.5(b-d) show the respective variations of σ_{zx}^{k} as functions of θ for $GaNMn_3$ (110). Similar angular dependences of σ_{zx}^{k} for the ground states of $NiNMn_3$, $SnNMn_3$, and $PtNMn_3$ (110) films can be found in Fig. 5.6 (a-c) respectively. Figure 5.6 shows the calculated $\hat{T}$-odd charge-to-spin conversion efficiency $\Phi(\sigma_{zx}^{k})$ as a function of longitudinal charge current direction for the ground state phases of ANMn3 (A = Ni, Sn, and Pt) stacked in (001) and (110) planes. Similar to the results in Fig. 5.5, we find that $\Phi(\sigma_{zx}^{k})$ is very small for (001) stacking and can be sizable for (110) stacking.

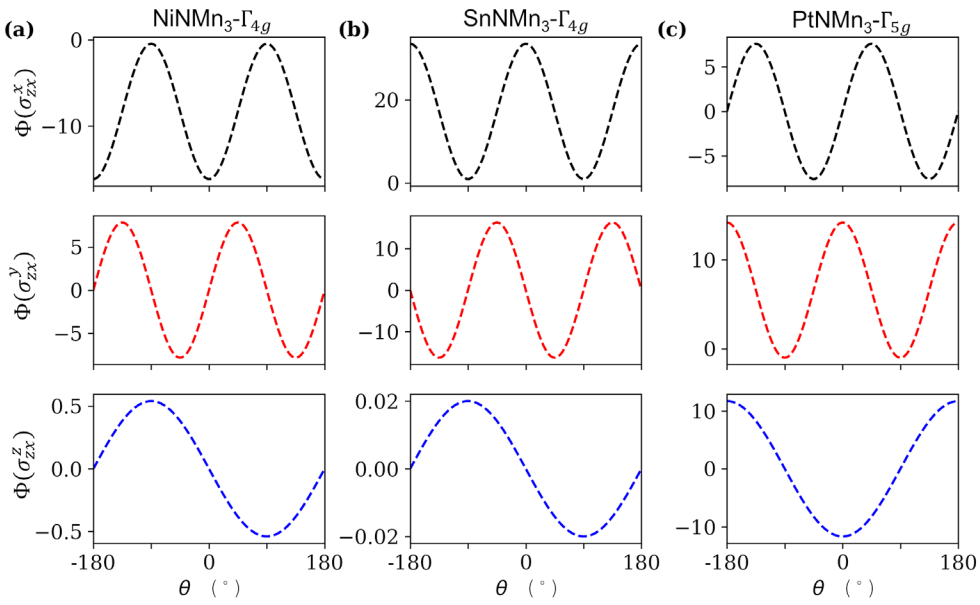

Figure 5.6. $\hat{T}$-odd charge-to-spin conversion efficiency $\Phi(\sigma_{zx}^{k})$ as a function of longitudinal charge current direction for ground state phases of ANMn$_3$ (110) (a) A = Ni, (b) A = Sn, and (c) A = Mn. The longitudinal charge current direction x is in the plane tilted away from the $[\bar{1}10]$ direction by an angle θ.

The predicted efficient generation of the longitudinal and transverse currents with sizable spin polarization allows promising spintronic devices based on noncollinear antiferromagnetic ANMn$_3$. Here we propose two types of spintronic devices, as shown in Figure 5.7. The first one is an antiferromagnetic tunnel junction, where the two ANMn$_3$ electrodes are separated by an insulating nonmagnetic layer [Fig. 5.7(a)]. The CPP longitudinal spin polarized current is controlled by the relative orientation of the magnetic order parameters in the ANMn$_3$ reference and free layers. Due to a large spin

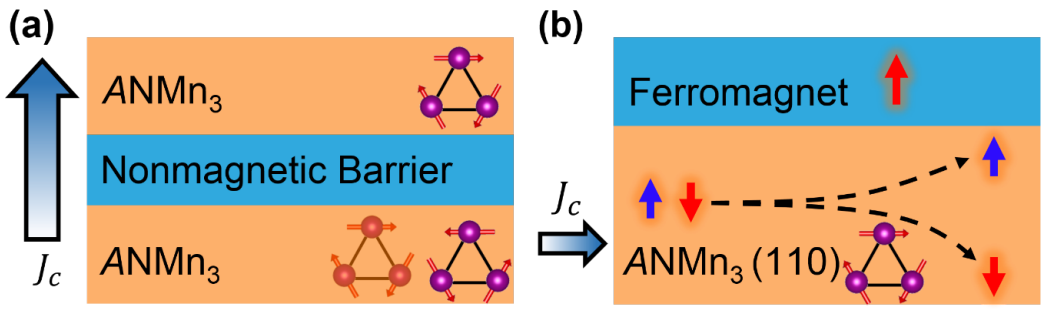

Figure 5.7. Antiferromagnetic spintronic devices. (a) The schematic of an antiferromagnetic tunnel junction using ANMn$_3$ as the electrodes, where the transport of the out-of-plane longitudinal spin polarized current is controlled by the relative orientation of the magnetic moments between two ANMn$_3$ layers. (b) The schematic of a spin torque device with CIP geometry. An in-plane charge current passes through ANMn$_3$ (110) layer and generates an out-of-plane spin current carrying sizable spin polarization collinear to the spin current direction. This spin current can exert a torque on the perpendicular magnetization in the top ferromagnetic layer for an efficient switching.

polarization of the longitudinal current, the TMR effect is expected to be sizable and hence can be used to efficiently detect the magnetic order parameter in ANMn$_3$. The spin polarized current can be also used to generate the spin-transfer torque for switching ANMn$_3$ [69- 71].

The second spintronic device is a CIP spin-torque device, where an ANMn$_3$ (110) layer is used as a spin source to generate an out-of-plane spin current which enters the top ferromagnetic layer and exerts a torque on its magnetization [Fig. 5.7(b)]. Since ANMn$_3$ (110) layer exhibits large $\Phi(\sigma_{zx}^{z})$, the spin current can carry sizable spin component collinear to the spin current direction, which is necessary for switching a ferromagnet with perpendicular anisotropy required for high-density spintronic devices.

In conclusion, based on first-principles density functional theory calculations, we have predicted that the low symmetry noncollinear antiferromagnetic antiperovskites ANMn$_3$ (A = Ga, Ni, Sn, and Pt) support electric currents with sizable spin polarization, and they also exhibit unconventional spin orbit torque due to unconventional spin polarization which was realized in experiment by our experimental collaborators. This unconventional torques can be robustly manipulated by controlling the antiferromagnetic ordering across the Néel temperature. We also found that the calculated spin polarization of the longitudinal currents can be comparable to that in widely used ferromagnetic metals, which makes the antiperovskites promising for using in antiferromagnetic tunnel junction and spin transfer torque devices. Furthermore, we demonstrated that by controlling the film growth direction, the out-of-plane transverse spin currents with sizable charge-to-spin conversion efficiencies can be achieved, which implies that the ANMn$_3$ compounds can serve as effective spin source materials. These properties make

noncollinear antiferromagnetic antiperovskites promising for realistic applications in spintronics.

References

[1] E. Y. Tsymbal and I. Žutić, Eds., *Spintronics Handbook: Spin Transport and Magnetism*. 2-nd edition (CRC press, 2019).

[2] A. V. Khvalkovskiy, D. Apalkov, S. Watts, R. Chepulskii, R. S. Beach, A. Ong, X. Tang, A. Driskill-Smith, W. H. Butler, P. B. Visscher, D. Lottis, E. Chen, V. Nikitin, and M. Krounbi, Basic principles of STT-MRAM cell operation in memory arrays. *J. Phys. D* **46**, 074001 (2013).

[3] M. Julliere, Tunneling between ferromagnetic films. *Phys. Lett.* **54A**, 225 (1975).

[4] J. S. Moodera, L. R. Kinder, T. M. Wong, and R. Meservey, Large magnetoresistance at room temperature in ferromagnetic thin film tunnel junctions. *Phys. Rev. Lett*. **74**, 3273 (1995).

[5] E. Y. Tsymbal, O. N. Mryasov, and P. R. LeClair, Spin-dependent tunneling in magnetic tunnel junctions. *J. Physics: Condensed Matter* **15**, R109-R142 (2003).

[6] J. C. Slonczewski, Conductance and exchange coupling of two ferromagnets separated by a tunneling barrier. *Phys. Rev. B* **39**, 6995 (1989).

[7] D. Ralph and M. Stiles, Spin transfer torques. *J. Magn.Magn. Mater*. **320**, 1190 (2008).

[8] J. Sinova, S. O. Valenzuela, J. Wunderlich, C. H. Back, and T. Jungwirth, Spin Hall effects. *Rev. Mod. Phys.* **87**, 1213 (2015).

[9] I. M. Miron, K. Garello, G. Gaudin, P.-J. Zermatten, M. V. Costache, S. Auffret, S. Bandiera, B. Rodmacq, A. Schuhl, and P. Gambardella. Perpendicular switching of a single ferromagnetic layer induced by in-plane current injection. *Nature (London)* **476**, 189 (2011).

[10] L. Liu, C.-F. Pai, Y. Li, H.W. Tseng, D. C. Ralph, and R. A. Buhrman, Spin-torque switching with the giant spin Hall effect of tantalum. *Science* **336**, 555 (2012).

[11] V. Baltz, A. Manchon, M. Tsoi, T. Moriyama, T. Ono, and Y. Tserkovnyak, Antiferromagnetic spintronics. *Rev. Mod. Phys.* **90**, 015005 (2018).

[12] T. Jungwirth, X. Marti, P. Wadley, and J. Wunderlich, Antiferromagnetic spintronics. *Nat. Nanotechnol.* **11**, 231 (2016).

[13] T. Jungwirth, J. Sinova, A. Manchon, X. Marti, J. Wunderlich, and C. Felser, The multiple directions of antiferromagnetic spintronics. *Nat. Phys.* **14**, 200 (2018).

[14] T. Nan, C. X. Quintela, J. Irwin, G. Gurung, D. F. Shao, J. Gibbons, N. Campbell, K. Song, S. Y. Choi, L. Guo, R. D. Johnson, P. Manuel, R. V. Chopdekar, I. Hallsteinsen, T. Tybell, P. J. Ryan, J. W. Kim, Y. S. Choi, P. G. Radaelli, D. C. Ralph, E. Y. Tsymbal, M. S. Rzchowski, and C. B. Eom, Controlling spin current polarization through non-collinear antiferromagnetism. *Nat. Commun.* **11**, 4671 (2020).

[15] F. Freimuth, S. Blügel, and Y. Mokrousov, Anisotropic spin Hall effect from first principles. *Phys. Rev. Lett.* **105**, 246602 (2010).

[16] Y. Zhang, Y. Sun, H. Yang, J. Železný, S. P. P. Parkin, C. Felser, and B. Yan, Strong anisotropic anomalous Hall effect and spin Hall effect in the chiral

antiferromagnetic compounds Mn_3X (X = Ge, Sn, Ga, Ir, Rh, and Pt). *Phys. Rev. B* **95**, 075128 (2017).

[17] G. Y. Guo, S. Murakami, T.-W. Chen, and N. Nagaosa, Intrinsic spin Hall effect in platinum: First-Principles Calculations. *Phys. Rev. Lett.* **100**, 096401 (2008).

[18] H. Chen, Q. Niu, and A. H. MacDonald, Anomalous Hall effect arising from noncollinear antiferromagnetism. *Phys. Rev. Lett*. **112**, 017205 (2014).

[19] L. Šmejkal, R. González-Hernández, T. Jungwirth, and J. Sinova, Crystal time-reversal symmetry breaking and spontaneous Hall effect in collinear antiferromagnets. *Sci. Adv.* **6**, eaaz8809 (2020).

[20] J. Kübler and C. Felser, Non-collinear antiferromagnets and the anomalous Hall effect. *EPL* **108**, 67001 (2014).

[21] S. Nakatsuji, N. Kiyohara, and T. Higo, Large anomalous Hall effect in a non-collinear antiferromagnet at room temperature. *Nature* **527**, 212 (2015).

[22] A. K. Nayak, J. E. Fischer, Y. Sun, B. Yan, J. Karel, A. C. Komarek, C. Shekhar, N. Kumar, W. Schnelle, J. Kübler, C. Felser, and S. P. P. Parkin, Large anomalous Hall effect driven by a nonvanishing Berry curvature in the noncollinear antiferromagnet Mn_3Ge. *Sci. Adv.* **2**, e1501870 (2016).

[23] Y. Zhang, Y. Sun, H. Yang, J. Železný, S. P. P. Parkin, C. Felser, and B. Yan, Strong anisotropic anomalous Hall effect and spin Hall effect in the chiral antiferromagnetic compounds Mn3X (X = Ge, Sn, Ga, Ir, Rh, and Pt). *Phys. Rev. B* **95**, 075128 (2017).

[24] G. Gurung, D.-F. Shao, T. R. Paudel, and E. Y. Tsymbal, Anomalous Hall conductivity of non-collinear magnetic antiperovskites. *Phys. Rev. Mater.* **3**, 044409 (2019).

[25] D. Boldrin, I. Samathrakis, J. Zemen, A. Mihai, B. Zou, B. Esser, D. McComb, P. Petrov, H. Zhang, and L. F. Cohen, The anomalous Hall effect in non-collinear antiferromagnetic Mn_3NiN thin films. *Phys. Rev. Mater.* **3**, 094409 (2019).

[26] X. Zhou, J.-P. Hanke, W. Feng, F. Li, G.-Y. Guo, Y. Yao, S. Blügel, and Y. Mokrousov, Spin-order dependent anomalous Hall effect and magneto-optical effect in the noncollinear antiferromagnets Mn_3XN with X = Ga, Zn, Ag, or Ni. *Phys. Rev. B* **99**, 104428 (2019).

[27] K. Zhao, T. Hajiri, H. Chen, R. Miki, H. Asano, and P. Gegenwart, Anomalous Hall effect in the noncollinear antiferromagnetic antiperovskite $Mn_3Ni_{1-x}Cu_xN$. *Phys. Rev. B* **100**, 045109 (2019).

[28] V. T. N. Huyen, M.-T. Suzuki, K. Yamauchi, and T. Oguchi, Topology analysis for anomalous Hall effect in the noncollinear antiferromagnetic states of Mn3AN (A= Ni, Cu, Zn, Ga, Ge, Pd, In, Sn, Ir, Pt), *Phys. Rev. B* **100**, 094426 (2019).

[29] Y. You, H. Bai, X. Chen, Y. Zhou, X. Zhou, F. Pan, and C. Song, Room temperature anomalous Hall effect in antiferromagnetic Mn_3SnN films. *Appl. Phys. Lett*. **117**, 222404 (2020).

[30] X. Li, A. H. MacDonald, and H. Chen, Quantum anomalous Hall effect through canted antiferromagnetism. *arXiv*:1902.10650 (2019).

[31] N. J. Ghimire, A. S. Botana, J. S. Jiang, J. Zhang, Y.-S. Chen, and J. F. Mitchell, Large anomalous Hall effect in the chiral-lattice antiferromagnet $CoNb_3S_6$. *Nat. Commun.* **9**, 3280 (2018).

[32] D. F. Shao, J. Ding, G. Gurung, S. H. Zhang, and E. Y. Tsymbal, Interfacial crystal Hall effect reversible by ferroelectric polarization. *Phys. Rev. Applied* **15**, 024057 (2021).

[33] K. Samanta, M. Ležaić, M. Merte, F. Freimuth, S. Blügel, and Y. Mokrousov, Crystal Hall and crystal magneto-optical effect in thin films of $SrRuO_3$. *Journal of Applied Physics* **127**, 213904 (2020).

[34] J. Kipp, K. Samanta, F. R. Lux, M. Merte, D. Go, J. P. Hanke, M. Redies, F. Freimuth, S. Blügel, M. Ležaić, and Y. Mokrousov, The chiral Hall effect in canted ferromagnets and antiferromagnets. *Commun. Physics* **4**, 99 (2021).

[35] S. Hayami, Yuki Yanagi, and Hiroaki Kusunose, Momentum-dependent spin splitting by collinear antiferromagnetic ordering. *J. Phys. Soc. Jpn.* **88**, 123702 (2019).

[36] L.-D. Yuan, Z. Wang, J. -W. Luo, E. I. Rashba, and A. Zunger, Giant momentum-dependent spin splitting in centrosymmetric low-Z antiferromagnets. *Phys. Rev. B* **102**, 014422 (2020).

[37] L.-D. Yuan, Z. Wang, J. -W. Luo, and A. Zunger, Prediction of low-Z collinear and noncollinear antiferromagnetic compounds having momentum-dependent spin splitting even without spin-orbit coupling. *Phys. Rev. Mater.* **5**, 014409 (2021).

[38] J. Železný, Y. Zhang, C. Felser, and B. Yan, Spin-polarized current in noncollinear antiferromagnets. *Phys. Rev. Lett.* **119**, 187204 (2017).

[39] M. Kimata, H. Chem, K. Kondou, S. Sugimoto, P. K. Muduli, M. Ikhlas, Y. Omori, T. Tomita, A. H. MacDonald, S. Nakatsuji, and Y. Otani, Magnetic and magnetic inverse spin Hall effects in a non-collinear antiferromagnet. *Nature* **565**, 627 (2019).

[40] A. Mook, R. R. Neumann, A. Johansson, J. Henk, and I. Mertig, Origin of the magnetic spin Hall effect: Spin current vorticity in the Fermi sea. *Phys. Rev. Research* **2**, 023065 (2020).

[41] R. González-Hernández, L. Šmejkal, K. Výborný, Y. Yahagi, J. Sinova, T. Jungwirth, J. Železný, Efficient electrical spin-splitter based on non-relativistic collinear antiferromagnetism. *Phys. Rev. Lett.* **126**, 127701 (2021).

[42] M. Naka, S. Hayami, H. Kusunose, Y. Yanagi, Y. Motome, and H. Seo, Spin current generation in organic antiferromagnets. *Nat. Commun.* **10**, 4305 (2019).

[43] H. Y. Ma, M. Hu, N. Li, J. Liu, W. Yao, J. F. Jia, and J. Liu, Multifunctional antiferromagnetic materials with giant piezomagnetism and noncollinear spin current. *Nat. Commun.* **12**, 2846 (2021).

[44] D. F. Shao, S. H. Zhang, M. Li, and E. Y. Tsymbal, Spin-neutral currents for spintronics. *arXiv*:2103.09219 (2021).

[45] S. Hu, D. F. Shao, H. Yang, M. Tang, Y. Yang, W. Fan, S. Zhou, E. Y. Tsymbal, and X. Qiu, Efficient field-free perpendicular magnetization switching by a magnetic spin Hall effect. *arXiv*:2103.09011 (2021).

[46] L. Šmejkal, A. B. Hellenes, R. G. Hernández, J. Sinova, and T. Jungwirth, Giant and tunneling magnetoresistance effects from anisotropic and valley-dependent spin-momentum interactions in antiferromagnets. *arXiv:*2103.12664 (2021).

[47] D. Fruchart and E. F. Bertaut, Magnetic studies of the metallic perovskite-type compounds of manganese. *J. Phys. Soc. Jap.* **44**, 781 (1978).

[48] P. Giannozzi, S. Baroni, N. Bonini, M. Calandra, R. Car, C. Cavazzoni, D. Ceresoli, G. L. Chiarotti, M. Cococcioni, I. Dabo, A. D. Corso, S. d. Gironcoli, S. Fabris, G. Fratesi, R. Gebauer, U. Gerstmann, C. Gougoussis, A. Kokalj, M. Lazzeri, L. M. Samos, N. Marzari, F. Mauri, R. Mazzarello, S. Paolini, A. Pasquarello, L. Paulatto, C. Sbraccia, S. Scandolo, G. Sclauzero, A. P. Seitsonen, A. Smogunov, P. Umari, and R. M. Wentzcovitch, Quantum ESPRESSO: A modular and open-source software project for quantum simulations of materials. *J. Phys.: Condens. Matt.* **21**, 395502 (2009).

[49] D. Vanderbilt, Soft self-consistent pseudopotentials in a generalized eigenvalue formalism. *Phys. Rev. B* **41**, 7892 (1990).

[50] J. P. Perdew, K. Burke, and M. Ernzerhof, Generalized gradient approximation made simple. *Phys. Rev. Lett.* **77**, 3865 (1996).

[51] J. Železný, *https://bitbucket.org/zeleznyj/wannier-linear-response/wiki/Home*

[52] N. Marzari, A. A. Mostofi, J. R. Yates, I. Souza, and D. Vanderbilt, Maximally localized Wannier functions: Theory and applications. *Rev. Mod. Phys.* **84,** 1419 (2012).

[53] G. Pizzi, V. Vitale, R. Arita, S. Blügel, F. Freimuth, G. Géranton, M. Gibertini, D. Gresch, C. Johnson, T.Koretsune, J. Ibañez-Azpiroz, H. Lee, J. M. Lihm, D. Marchand, A. Marrazzo, Y. Mokrousov, J. I. Mustafa, Y. Nohara, Y. Nomura, L. Paulatto, S. Poncé, T. Ponweiser, J. Qiao, F. Thöle, S. S. Tsirkin, M. Wierzbowska, N. Marzari, D. Vanderbilt, I. Souza, A. A. Mostofi, and J. R. Yates, Wannier90 as a community code: New features and applications. *J. Phys. Cond. Mat.* **32**, 165902 (2020).

[54] J. Železný, *https://bitbucket.org/zeleznyj/linear*.

[55] M. B. Nardelli, F. T. Cerasoli, M. Costa, S. Curtarolo, R. De Gennaro, M. Fornari, L. Liyanage, A. Supka, and H. Wang, PAOFLOW: A utility to construct and operate on ab-initio Hamiltonians from the projections of electronic wavefunctions on atomic orbital bases, including characterization of topological materials. *Comp. Mat. Sci.* **143**, 462 (2017).

[56] L. A. Agapito, A. Ferretti, A. Calzolari, S. Curtarolo, and M. B. Nardelli, Effective and accurate representation of extended Bloch states on finite Hilbert spaces. *Phys. Rev. B* **88**, 165127 (2013).

[57] L. A. Agapito, S. Ismail-Beigi, S. Curtarolo, M. Fornari, and M. B. Nardelli, Accurate tight-binding hamiltonian matrices from ab-initio calculations: Minimal basis sets. *Phys. Rev. B* **93**, 035104 (2016).

[58] K. Momma, and F. Izumi, VESTA: a three-dimensional visualization system for electronic and structural analysis. *J. Appl. Crystal.* **41**, 653 (2008).

[59] M. Kawamura, Fermisurfer: Fermi-surface viewer providing multiple representation schemes. *Comp. Phys. Commun.* **239**, 197 (2019).

[60] M. Seeman, D. Ködderitzch, S. Wimmer, and H. Ebert, Symmetry-imposed shape of linear response tensors. *Phys. Rev. B* **92**, 155138 (2015).

[61] A. M. Humphries, T. Wang, E. R. J. Edwards, S. R. Allen, J. M. Shaw, H. T. Nembach, J. Q. Xiao, T. J. Silva, and X. Fan, Observation of spin-orbit effects with spin rotation symmetry. *Nat. Commun.* **8**, 911 (2017).

[62] D. MacNeill, G. N. Stiehl, M. H. D. Guimaraes, R. A. Buhrman, J. Park, and D C. Ralph, Control of spin-orbit torques through crystal symmetry in WTe_2/ferromagnet bilayers. *Nat. Phys.* **13**, 300 (2017).

[63] R. J. Soulen Jr., J. M. Byers, M. S. Osofsky, B. Nadgorny, T. Ambrose, S. F. Cheng, P. R. Broussard, C. T. Tanaka, J. Nowak, J. S. Moodera, A. Barry, and J. M. D. Coey, Measuring the spin polarization of a metal with a superconducting point contact. *Science* **282**, 85, (1998)

[64] S. K. Upadhyay, A. Palanisami, R. N. Louie, and R. A. Buhrman, Probing ferromagnets with Andreev reflection. *Phys. Rev. Lett.* **81**, 3247 (1998).

[65] I. I. Mazin, How to Define and Calculate the Degree of Spin Polarization in Ferromagnets. *Phys. Rev. Lett.* **83**, 1427 (1999).

[66] X. Tao, Q. Liu, B. Miao, R. Yu, Z. Feng, L. Sun, B. You, J. Du, K. Chen, S. Zhang, L. Zhang, Z. Yuan, D. Wu and H. Ding, Self-consistent determination of spin Hall angle and spin diffusion length in Pt and Pd: The role of the interface spin loss. *Sci. Adv.* **4**, eaat1670 (2018).

[67] A. J. Berger, E. R. J. Edwards, H. T. Nembach, O. Karis, M. Weiler, and T. J. Silva, Determination of the spin Hall effect and the spin diffusion length of Pt from self-consistent fitting of damping enhancement and inverse spin-orbit torque measurements. *Phys. Rev. B* **98**, 024402 (2018).

[68] S. Keller, L. Mihalceanu, M. R. Schweizer, P. Lang, B. Heinz, M. Geilen, T. Brächer, P. Pirro, T. Meyer, and A. Conca, Determination of the spin Hall angle in single-crystalline Pt films from spin pumping experiments. *New J. Phys.* **20**, 053002 (2018).

[69] H. V. Gomonay, and V. M. Loktev, Spin transfer and current-induced switching in antiferromagnets. *Phys. Rev. B* **81**, 144427 (2010).

[70] H. Fujita, Field-free, spin-current control of magnetization in non-collinear chiral antiferromagnets. *Phys. Stat. Solidi RRL* **11**, 1600360 (2017).

[71] Y. Yamane, O. Gomonay, and J. Sinova, Dynamics of noncollinear antiferromagnetic textures driven by spin current injection. *Phys. Rev. B* **100**, 054415 (2019).

Chapter 6 Conclusions

This research work is aimed to identify the effective way of manipulating and detecting the Néel vector and in addition, to find other related spin-dependent properties such as spin Hall and anomalous Hall conductivities and spin polarization. Based on the symmetry analyses, first-principles DFT calculations, tight binding Hamiltonian, and magnetization dynamics techniques, we have explored the possibility of using noncollinear AFM antiperovskites $ANMn_3$ (A = Ga, Ni, Sn, Pt) for spintronics applications. We have demonstrated a way to read and write the AFM order parameter – the Néel vector, using the spin polarized current. Our results have clearly demonstrated the emergence of the unconventional spin polarization associated with the noncollinear magnetic structure in the antiferromagnets.

We considered $GaNMn_3$ as the representative antiperovskite compound for the detailed study of different magnetic phases, such as an ferrimagnetic (M-1) phase and noncollinear AFM Γ_{5g} and Γ_{4g} phases. We showed that the combination of the time reversal symmetry $\hat{T}$ and mirror symmetry $\widehat{M}$ in the Γ_{4g} magnetic phase makes the Berry curvature odd and hence, the AHC finite. On the contrary, the Γ_{5g} phase exhibits only $\widehat{M}$ symmetry resulting in zero AHC. The presence of the finite AHC in the Γ_{4g} phase is correlated with the finite out-of-plane magnetization (along the [111] axis) not forbidden by the $\hat{T}\widehat{M}$ symmetry, whereas its absence in the Γ_{4g} phase is correlated with $\widehat{M}$ symmetry prohibiting any finite magnetization. The finite AHC in the Γ_{4g} phase can be used to read out the state of the Néel vector during its manipulation.

Our results have demonstrated the possibility to manipulate the Néel vector by passing a spin-polarized charge current (with the spin polarization perpendicular to the (111) plane) in the $GaNMn_3$ (111) thin film. The dynamics of the Néel vector occurs in the terahertz frequency range. The stoichiometric engineering of the antiperovskite material ($Ga_{0.42}Ni_{0.58}NMn_3$) was demonstrated to highly reduce the critical current density required for the switching of the Néel vector. Since the Néel vector switching reverses the sign of the anomalous Hall effect, measuring the AHC allows an unambiguous detection of the Néel vector orientation. Thus, the predicted functional properties of the non-collinear AFM antiperovskites allow using these materials in ultrafast energy-efficient spintronic devices.

In addition to the control of the Néel vector, we have also explored the spin polarization of the spin conductivity tensor in the noncollinear antiferromagnets. The lower symmetry of the noncollinear AFM phase of $ANMn_3$ compared to its high-temperature paramagnetic phase allows both conventional and unconventional spin conductivity components. The unconventional component has the out-of-pane spin polarization and thus allows for an unconventional spin torque to be exerted on the magnetization of an adjacent ferromagnetic layer which can switch its out-of-plane magnetization. This phenomenon not possible using non-magnetic heavy metals as the source of a spin current. The predicted phenomenon has been observed in the experiments by our collaborators at University of Wisconsin-Madison using spin torque ferromagnetic resonance measurements. We conclude therefore that the noncollinear AFM antiperovskites can be efficiently used to produce spin torques of desired symmetry and thus behave superior to widely-used paramagnetic heavy metals.

We have shown that the unique spin texture associated with the noncollinear AFM antiperovskites $ANMn_3$ supported a spin-polarized charge current. In this regard, AFM antiperovskites behave like ferromagnets revealing a possibility of the AFM tunnel junctions. The structural similarity of the antiperovskites with perovskite oxides makes it feasible to grow them epitaxially. Our results have demonstrated that the charge-to-spin efficiency can be maximized by growing antiperovskite $ANMn_3$ thin films along specific directions. For example, a (110) oriented $GaNMn_3$ film was found to be an effective spin source with sizable charge-to-spin conversion efficiency.

Overall, our research work shows the pathway for the development of ultrafast, ultradense, and ultrarobust spintronic devices with antiferromagnets as functional materials. While some of our theoretical predictions have been already demonstrated experimentally, many of them remain to be explored. For example, it would be interesting to explore the magnetization dynamics in non-collinear antiperovskites driven by spin-polarized charge currents and realize the proposed spintronic devices (*e.g.* those shown in Fig. 5.7). We do hope therefore that our results will stimulate the experimentalists working in the field of antiferromagnetic spintronics to further verify our predictions.

Appendices

Appendix A: Magnetization Dynamics in a Ferromagnet and a Two-Sublattice Antiferromagnet

The magnetization dynamics in a ferromagnet can be defined using the phenomenological equation

$$\frac{\partial \vec{m}}{\partial t} = \gamma\left(\vec{m} \times \vec{H}^{eff}\right), \qquad (A1)$$

where $\vec{m}$ is the magnetization of the ferromagnet , $\vec{H}^{eff}$ is the effective magnetic field which consists of the external field ($\vec{H}^{ext}$) and internal field ($\vec{H} = -\sum_{i=x,y,z} \frac{\partial F}{\partial m_i}\, \hat{\imath}$, where F is the free energy and m_i is an *i*-component of the magnetization vector) . The external field generally consist of the static magnetic field ($\vec{H}^{stat}$) and a small *rf* magnetic field ($\vec{H}^{rf}$). The internal magnetic field is contributed generally due to the anisotropic energy and the exchange energy. Considering uniaxial anisotropy pointing in the $\hat{z}$ direction, the anisotropy field is defined as $\vec{H}^{K} = H_K\, \hat{z}$. The exchange field is given by $\vec{H}^{E} = -J\, \vec{M}$, similar to the Weiss molecular field. There are also other contributions like the demagnetization field, the DMI field, the dipole-dipole field, *etc*. Equation $A1$ describes the precession of the magnetization around the effective magnetic field $\vec{H}^{eff}$ and this term determines the FM resonance. The actual magnetization term contains the Gilbert damping term as well but Eq. $(A1)$ is sufficient to obtain the FMR frequency. Considering only the static magnetic field $\vec{H}^{stat} = H_o\, \hat{z}$ along $\hat{z}$ direction, Eq. $(A1)$ can be rewritten as,

$$\frac{\partial m_x}{\partial t} = \gamma(H_K + H_o)m_y \,, \tag{A2}$$

$$\frac{\partial m_y}{\partial t} = -\gamma(H_K + H_o)m_x \,. \tag{A3}$$

Substituting $m_i = M_s e^{-i\omega t}$, we find the frequency is $\omega_{FM} = \gamma(H_K + H_o)$. The FMR frequency is $\omega = \gamma H_K$ which shows that the anisotropy field determines the strength of the FMR. In ferromagnets the FMR frequency is in the gigahertz (GHz) range.

In the case of a two-sublattice antiferromagnets, the antiferromagnet can be considered as two ferromagnets with two oppositely oriented magnetizations and hence, they can be described by two separate equations ($A1$). The difference arises due to the exchange field which couples the two equations for two sublattices. This coupling completely changes the magnetization dynamics in antiferromagnets and these leads to interesting phenomena.

The corresponding equations are

$$\frac{\partial \vec{m}^s}{\partial t} = \gamma \left(\vec{m}^s \times \vec{H}^{eff,s} \right);\ s = A, B \,, \tag{A4}$$

where the effective field for the s^{th} sublattice is $\vec{H}^{eff,s} = \vec{H}_K^s + \vec{H}_E^s + \vec{H}_{ext}^s$. Considering the static external field $\vec{H}_{ext}^s = \vec{H}_{rf} + \vec{H}_{stat} = 0 + H_0\,\hat{z}$, the exchange field $\vec{H}^{E,s} = -J\,\vec{m}^{s'}$ for sublattices $s \neq s' = A, B$ with $J \neq 0$ and the anisotropic field $\vec{H}^{K,s} = (-1)^s H_K\,\hat{z}$, where $s = 0{,}1$ for A, B sublattices, respectively. Substituting this into equation ($A4$) and using $H_E = Jm_z^A = -Jm_z^B$, we obtain

$$\omega = \gamma \left(H_0 \pm \sqrt{H_A(2H_E + H_A)} \right), \tag{A5}$$

The AFM resonance frequency is $\omega_{AFM} = \omega_{FM}\sqrt{\frac{2H_E}{H_K}}$ and it is much larger than the corresponding FM resonance frequency. Generally, in most of the materials $H_K < 1T; H_E \sim 10^2 T$ and hence, the AFMR is in the terahertz (THz) range.

We can define the Néel vector $\vec{l} = \vec{m}^A - \vec{m}^B$ and the magnetization vector $\vec{m} = \vec{m}^A + \vec{m}^B$ such that $\vec{l} \cdot \vec{m} = 0$ and $\vec{l} \cdot \vec{l} + \vec{m}.\vec{m} = 4M_s^2$, where M_s is the saturation magnetization that is $|\vec{m}^A| = |\vec{m}^B| = M_S$. The first conditional relation is always satisfied whatever be the sublattice number and hence, the magnetization vector is always perpendicular to the Néel vector. Similarly, we can obtain other conditional equations for a given AFM sublattice. Denoting $\vec{m}^A = \frac{\vec{l}+\vec{m}}{2}$ and $\vec{m}^B = \frac{\vec{m}-\vec{l}}{2}$, we can rewrite the above equations as follows

$$\frac{\partial(\vec{m}+\vec{l})}{\partial t} = \gamma\left((\vec{m}+\vec{l}) \times \vec{H}^{eff,A}\right), \tag{A6}$$

$$\frac{\partial(\vec{m}-\vec{l})}{\partial t} = \gamma\left((\vec{m}-\vec{l}) \times \vec{H}^{eff,B}\right), \tag{A7}$$

where $\vec{H}^{eff,A} = \vec{H}^{stat,A} + \vec{H}^{K,A} - \frac{J(\vec{m}-\vec{l})}{2}$ and $\vec{H}^{eff,B} = \vec{H}^{stat,B} + \vec{H}^{K,B} - \frac{J(\vec{m}+\vec{l})}{2}$. In the above case, we assumed $\vec{H}^{stat,s} = H_0\,\hat{z},\ \vec{H}^{K,s} = (-1)^s H_K\,\hat{z}$, where $s = 0,1$ for A, B sublattices, respectively. Below, we consider two cases.

Case 1: Staggered field $\vec{H}^{stat,s} = (-1)^s \vec{H}_0$, $\vec{H}^{K,s} = (-1)^s\,\vec{H}_K; s = 0,1$ for A, B. In this case, we obtain

$$\frac{\partial \vec{m}}{\partial t} = \gamma\left(\vec{l} \times (\vec{H}_0 + \vec{H}_K)\right), \tag{A8}$$

$$\frac{\partial \vec{l}}{\partial t} = \gamma\big(\vec{m} \times (\vec{H}_0 + \vec{H}_K)\big) - \gamma J\, \vec{l} \times \vec{m}. \tag{A9}$$

Then taking a cross product with $\vec{l}$ and assuming that J is large, $|\vec{m}| \ll |\vec{l}|$, we have

$$\vec{m} \approx -\frac{\dot{\vec{l}} \times \vec{l}}{4\gamma J M_s^2}. \tag{A10}$$

Substituting into Eq. $(A8)$, we obtain

$$\ddot{\vec{l}} \times \vec{l} = -\gamma^2 J l^2 \big(\vec{l} \times (\vec{H}_0 + \vec{H}_K)\big). \tag{A11}$$

Taking a cross product with $\vec{l}$ again and assuming that dynamics does not change the length of the Néel vector ($\vec{l} \cdot \dot{\vec{l}} = 0$), we have

$$\ddot{\vec{l}} = -\gamma^2 J \left(\vec{l} \times \vec{l} \times \left(\vec{H}_0 + \vec{H}_K\right)\right) - \frac{1}{l^2}\dot{\vec{l}}^2 \vec{l}. \tag{A12}$$

This is the Newtonian equation for the Néel vector indicating that the Néel vector acts as a solid object with mass so that the AFM dynamics exhibits inertia. These properties are enhanced by the exchange term J. So, comparing Eqs. $(A1)$ and $(A12)$ for ferromagnets and antiferromagnets, we see that the latter behave very differently in a way that the effects are enhanced by the exchange term. Equation $(A1)$ describes the conic motion of the magnetization $\vec{m}$ and Eq. $(A12)$ describes the Néel vector $\vec{l}$ planar motion under the staggered field.

Case 2: Uniform field $\vec{H}^{stat,s} = \vec{H}_0$, $\vec{H}^{K,s} = (-1)^s\, \vec{H}_K; s = 0{,}1\ for\ A, B$. In this case, we obtain

$$\frac{\partial \vec{m}}{\partial t} = \gamma(\vec{m} \times \vec{H}_0) + \gamma(\vec{l} \times \vec{H}_K), \tag{A12}$$

$$\frac{\partial \vec{l}}{\partial t} = \gamma\left(\vec{l} \times \vec{H}_0\right) + \gamma(\vec{m} \times \vec{H}_K) - \gamma J\, \vec{l} \times \vec{m}. \qquad (A13)$$

Going through the same process as in case 1, we find that

$$\vec{m} = -\frac{1}{\gamma J l^2}\left[\dot{\vec{l}} \times \vec{l} + \gamma\, \vec{l}\left(\vec{H}_0.\vec{l}\right) - \gamma l^2\, \vec{H}_0\right], \qquad (A14)$$

$$\ddot{\vec{l}} \times \vec{l} = -\gamma\, \dot{\vec{l}}\left(\vec{H}_0.\vec{l}\right) + \gamma\left(\vec{l} \times \vec{H}_0\right)\left(\vec{H}_0.\vec{l}\right) - \gamma^2 J l^2\left(\vec{l} \times \vec{H}_K\right). \qquad (A15)$$

Considering the field to be parallel to $\vec{l}$, we have

$$\ddot{\vec{l}} \times \vec{l} = -\gamma\, \dot{\vec{l}}\, H_0 l - \gamma^2 J l^2\left(\vec{l} \times \vec{H}_K\right), \qquad (A16)$$

and for the field perpendicular to $\vec{l}$,

$$\ddot{\vec{l}} \times \vec{l} = \gamma^2 J l^2\left(\vec{l} \times \vec{H}_K\right). \qquad (A17)$$

Therefore, when the magnetic field is applied parallel to the Néel vector, the magnetic field affects the dynamics of the Néel vector in our approximation scheme.

Appendix B: Magnetic Ground State of Antiperovskites $ANMn_3$

Table B1 lists the calculated lattice parameters, the magnitude of the magnetic moments, and the ground state energies for ANMn$_3$ (A = Ga, Ni, Sn, and Pt). We find that GaNMn$_3$ and PtNMn$_3$ have the Γ_{5g} ground state, and NiNMn$_3$ and SnNMn$_3$ have the Γ_{4g} ground state. The calculated results are consistent well with the experimentally observed and previously calculated values. We find that the differences in the lattice parameters and magnetic moments for the Γ_{4g} and Γ_{5g} phases are negligible.

Table B1. Calculated lattice parameters (a) and magnetic moments $(|\vec{m}|)$ for ANMn$_3$ (A = Ga, Ni, Sn, and Pt).

	GaNMn$_3$	NiNMn$_3$	SnNMn$_3$	PtNMn$_3$
$\boldsymbol{a}$ (Å)	3.87	3.84	3.99	3.93
$\|\vec{\boldsymbol{m}}\|$ ($\boldsymbol{\mu_B}$/Mn)	2.16	2.45	2.33	2.72
$\boldsymbol{E_{5g} - E_{4g}}$ (meV)	-0.5	0.1	0.02	-0.5

Appendix C: Geometry Dependence of Anomalous Hall Conductivity

The Anomalous Hall Conductivity (AHC) tensor depends on geometry used in transport measurements. Table 3.1 in Chapter 3 shows the AHC tensor for $GaNMn_3$ (001) growth orientation corresponding to the standard Cartesian coordinates with *x* along [100], *y* along [010], and *z* along [001] directions. For $GaNMn_3$ (111) sample, the AHC can be measured for a charge current parallel to the Ga-Mn Kagome lattice. Here we show the AHC tensor for a $GaNMn_3$ (111) sample, with *x* pointing along $[\bar{1}10]$, *y* along $[\bar{1}\bar{1}2]$ and *z* along [111] directions. The respective AHC tensor $\sigma_{[111]}$ can be obtained from

$$\sigma_{[111]} = R\ \sigma_{[001]}\ R^{-1} \tag{C1}$$

where $\sigma_{[001]}$ is the AHC tensor for $GaNMn_3$ (001) and R represents the respective rotation matrix. The resulting AHC tensors for Γ_{4g} and Γ_{5g} phases are shown in Table C1, where $\sigma'_{xy} = -68\ \Omega^{-1}cm^{-1}$.

Table C1. AHC matrix tensors for Γ_{5g} and Γ_{4g} magnetic phases with $\hat{x}||[\bar{1}10]$, $\hat{y}||[\bar{1}\bar{1}2]$ and $\hat{z}||[111]$.

Magnetic Phase	Γ_{5g}	Γ_{4g}
AHC tensor	$\begin{bmatrix} 0 & 0 & 0 \\ 0 & 0 & 0 \\ 0 & 0 & 0 \end{bmatrix}$	$\begin{bmatrix} 0 & \sigma'_{xy} & 0 \\ -\sigma'_{xy} & 0 & 0 \\ 0 & 0 & 0 \end{bmatrix}$

Appendix D: Moment Orientation Dependence of Anomalous Hall Conductivity

Figure D1 shows the variation of the anomalous Hall conductivity of $Ga_{0.42}Ni_{0.58}NMn_3$ due to the rotation of the magnetic moments around [111] axis. The calculations were carried out for each configuration with a fixed angle ϕ, as shown in Figure D1 (top panel). Equation C1 can also be used to obtain the angular dependence of the AHC.

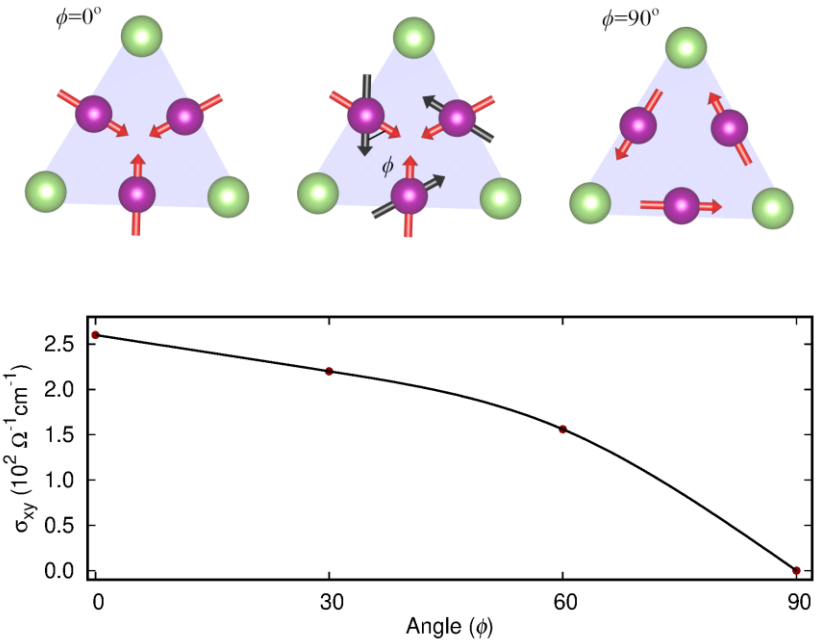

Figure D1. The calculated anomalous Hall conductivity of $Ga_{0.42}Ni_{0.58}NMn_3$ as a function of the magnetic moment orientation determined by angle ϕ. $\phi = 0^o$ corresponds the Γ_{4g} magnetic phase while $\phi = 90^o$ corresponds to the Γ_{5g} magnetic phase.